SANDIA REPORT
SAND2024-07522
Printed June 2024

LYNM PE1 Pre-Experiment A Site Characterization Report

Miles Bodmer[1], Margaret Townsend[2], Barry Roberts[1], Jennifer Wilson[1], Justin Reppart[2], Devon Smith[2], Nicholas Downs[2], Joshua Feldman[3], R. Charles Choens II[1], Jason Heath[1], Austin Holland[1], Perry Barrow[1], Tara Bartlett[2], Hakim Boukhalfa[4], Scott Broome[1], Matthew Dietel[2], Christine Downs[1], Souheil Ezzedine[5], Clayton Freimuth[2], James Griego[1], Mathew Ingraham[1], Johnny Jaramillo[1], Kyle Jones[1], William Kibikas[1], Kristopher Kuhlman[1], Jennifer Larotonda[2], Andrew Miller[2], Shawn Otto[4], Matthew Powell[1], Mark Rodriguez[1], Josh Tafoya[1], Nichole Valdez[1], Guangping Xu[1], Stephanie Lyons[3], Philip Stauffer[4].

[1] Sandia National Laboratories
[2] Nevada National Security Sites
[3] Pacific Northwest National Laboratory
[4] Los Alamos National Laboratory
[5] Lawrence Livermore National Laboratory

Prepared by
Sandia National Laboratories
Albuquerque, New Mexico
87185 and Livermore,
California 94550

Issued by Sandia National Laboratories, operated for the United States Department of Energy by National Technology & Engineering Solutions of Sandia, LLC.

Available to DOE and DOE contractors from
U.S. Department of Energy
Office of Scientific and Technical Information
P.O. Box 62
Oak Ridge, TN 37831

Telephone: (865) 576-8401
Facsimile: (865) 576-5728
E-Mail: reports@osti.gov
Online ordering: http://www.osti.gov/scitech

Available to the public from
U.S. Department of Commerce
National Technical Information Service
5301 Shawnee Rd
Alexandria, VA 22312

Telephone: (800) 553-6847
Facsimile: (703) 605-6900
E-Mail: orders@ntis.gov
Online order: https://classic.ntis.gov/help/order-methods/

ABSTRACT

Underground chemical explosive experiments such as LYNM PE1 generate large multi-phenomenological datasets, require complex site preparation and build out, and utilize cutting edge models and analysis techniques to analyze and simulate the explosion-induced signals. This wide range of outcomes makes it a necessity to thoroughly characterize the testbed in advance of experiments in a way that complements the wide suite of data being generated. Here, we present a broad overview of the site characterization work and data collection that was conducted before Experiment A, which is the first in a series of three PE1 experiments. This work includes, but is not limited to, geologic mapping, physical sample collection, analysis of material properties, geophysical borehole logging, and in-situ measurements. This information was collected by a large, dedicated team and was used to inform site construction, finalize instrumentation placement, generate Geologic Framework Models, feed pre-experiment predictions, and facilitate post-experiment data analysis.

ACKNOWLEDGEMENTS

This Low Yield Nuclear Monitoring (LYNM) research was funded by the National Nuclear Security Administration, Defense Nuclear Nonproliferation Research and Development (NNSA DNN R&D). The authors acknowledge important interdisciplinary collaboration with scientists and engineers from LANL, LLNL, NNSS, PNNL, and SNL.

Funding statements

The views expressed in the document do not necessarily represent the views of the U.S. Department of Energy or the United States Government.

Los Alamos National Laboratory

Unless otherwise indicated, this information has been authored by an employee or employees of the Triad National Security, LLC (LANS), operator of the Los Alamos National Laboratory under Contract No. 89233218CNA000001 with the NNSA, U.S. Department of Energy.

Lawrence Livermore National Laboratory

Lawrence Livermore National Laboratory is operated by Lawrence Livermore National Security, LLC, for the U.S. Department of Energy, National Nuclear Security Administration under Contract DE-AC52-07NA27344.

Pacific Northwest National Laboratory

This document was sponsored by a contractor of the U.S. Government under contract DE-AC05-76RL01830.

Sandia National Laboratories

Sandia National Laboratories is a multimission laboratory managed and operated by National Technology & Engineering Solutions of Sandia, LLC, a wholly owned subsidiary of Honeywell International Inc., for the U.S. Department of Energy's National Nuclear Security Administration under contract DE-NA0003525.

Mission Support and Test Services, LLC

This document was sponsored by the U.S. Department of Energy, National Nuclear Security Administration under contract DE-NA0003624 through Mission Support and Test Services, operator of the Nevada National Security Site.

CONTENTS

LIST OF FIGURES

LIST OF TABLES

This page left blank

ACRONYMS AND TERMS

Acronym/Term	Definition
AC	Accelerometer
BSE	Backscattered Electrons
CT	Computed Tomography
DA	Drift Accelerometer
DD	Dip Direction
DEM	Digital Elevation Map
DI	Deionized Water
EDAX	Energy Dispersive X-Ray
EDS	Energy Dispersive Spectra
FEHM	Finite Element Heat and Mass
GFM	Geologic Framework Model
GI	Geologic Investigation
GS	Gas Sampling
GZ	Ground Zero
HE	High Explosive
HF	Hydrofracture
HLD	Leeb D
HQ	2.5 inches (96 mm outer diameter, 64 mm inner diameter) dill core size
LANL	Los Alamos National Laboratory
LiDAR	Light Detection and Ranging
LVDTs	Linear Variable Displacement Transducers
MDA	Minimum Detectable Activity
MICP	Mercury Intrusion Capillary Pressure
MSA	Multivariate Statistical Analysis
MSTS	Mission Support and Test Services
ND	Not Determined
NER	New England Research
NNSS	Nevada National Security Sites
P-Tunnel	U12p Tunnel
PCA	Principal Component Analysis
PE1	Physics Experiment 1
PH	Practice Borehole
PNNL	Pacific Northwest National Laboratory
PQ	4.8 inches (122 mm outer diameter, 85 mm inner diameter) drill core size

Acronym/Term	Definition
RQD	Rock Quality Designation
SE	Secondary Electrons
SEM	Scanning Electron Microscopy
SF6	Sulfur Hexafluoride
SNL	Sandia National Laboratories
SVGS	Small Volume Gas Samples
TD	Total Depth
TE	Tunnel Environment
TGA	Thermogravimetric Analysis
UNESE	Underground Nuclear Explosives Signatures Experiment
USGS	United States Geological Survey
UV	Ultraviolet
UWT	Upper Welded Tuff
UZNT	Upper Zeolitic Non-Welded Tuff
VG	Van Genuchten
VNT	Vitric Non-Welded Tuff
XRD	X-Ray Diffraction
XRF	X-Ray Florescence

1. INTRODUCTION

The purpose of this document is to describe and highlight the site characterization work done for the Physics Experiment 1 (PE1) testbed in preparation for PE1 Experiment A. Experiment A was a fully coupled chemical explosive experiment in an underground chamber located in the northern section of the Nevada National Security Site (NNSS) and is the first in a series of three planned explosive experiments (Myers et al., 2024) [14]. This work includes geologic mapping and characterization, sample preservation and management, geophysical characterization of boreholes, geomechanical rock property measurements, geochemical characterization, and background atmospheric, liquid, and radiologic sampling.

Characterization of the PE1 testbed is a critical component of the project, which informs site construction, instrument planning, and analysis. As a part of PE1, three drifts and chambers are being mined in the P Tunnel complex, with a significant portion of site characterization work occurring before the mining of the drifts and all the work presented here taking place before the mining of the final two chambers. Results of material properties measurements and geologic mapping inform activities such as mining, borehole drilling, chamber placement, and confinement. Understanding of the geology and borehole conditions directly influences decisions on instrumentation emplacement and optimization. Finally, detailed site characterization directly feeds predictive models of seismic wave propagation, gas transport, radionuclide tracers, and source mechanics, as well as the analysis of the observed seismic, infrasound, cavity, radionuclide, gas and liquid samples, and physical deformation data.

This document describes the data collection efforts in the field, the systems used to collect data, the initial observations, and notable findings related to site characterization work performed prior to Experiment A. In several instances, more detailed results can be found in cited topic-specific reports and publications, as this document is meant to provide a high-level overview of the site characterization effort.

This page left blank

2. TESTBED OVERVIEW

Understanding the geologic medium in which an explosive test takes place is critical to inform experiment design, risk and hazard assessment, modeling efforts, and the analysis of recorded signals.

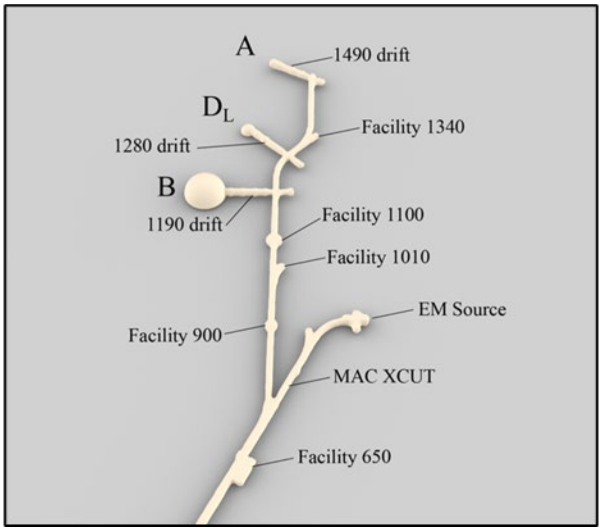

Figure 1. Oblique view of the P-Tunnel Complex where PE1 was conducted. Notable locations for the experiment are identified.

The PE1 experiment testbed was constructed within the U12p Tunnel (P-Tunnel) complex, which is located within Aqueduct Mesa at the Nevada National Security Site (NNSS) (Figure 1). The testbed includes previously constructed areas such as the U12p.06 Bypass drift and newly constructed drifts specific to PE1. As of this report, three experimental drifts have been constructed, referred to as the 1490, 1280, and 1190 drifts. These drifts initiate from the west rib of the U12p.06 Bypass to the A, D_L, and B experiment locations, respectively. The B and D_L Chambers will be constructed in a future second mining phase following the execution of Experiment A.

P-Tunnel is located within a bedded sequence of nonwelded pyroclastic deposits of generally rhyolitic composition (Figure 2). This bedded sequence lies between two densely welded regional ignimbrites, the Rainier Mesa Tuff (Tmr; 11.65 Ma), which caps much of Rainier and Aqueduct Mesas, and the Grouse Canyon Tuff (Tbg; 13.7 Ma), which lies more than 150 m below P-Tunnel. In the PE1 testbed region, the bedded pyroclastic deposits dip eastward at approximately eight degrees. During the original construction of P-Tunnel, this bedded sequence was referred to as "Paintbrush Tuff," but this stratigraphic designation has been superseded by formal regional stratigraphic nomenclature.

The rocks in which P-Tunnel was constructed consist mostly of nonwelded ash- and pumice-fall deposits, as well as ash-flow tuff assigned stratigraphically to the Crater Flat Group (13.25 Ma), Wahmonie Formation (13.0 Ma), and the Calico Hills Formation (12.9 Ma). Rocks within the Calico Hills Formation tend to be vitric (i.e., the volcanic glass and pumice retain their original glassy structure), but in older units the glass has been altered to zeolite. Very thin, completely silicified beds (typically less than 10 cm thick) are present throughout the section but are more common within the zeolitic rocks and in the transition zone between vitric and zeolitic rocks. Argillic and opaline alteration is common in most rocks, but typically in minor proportions. Alteration appears to be partially controlled by bedding but is also observed to cut across bedding, as well as changing laterally within beds.

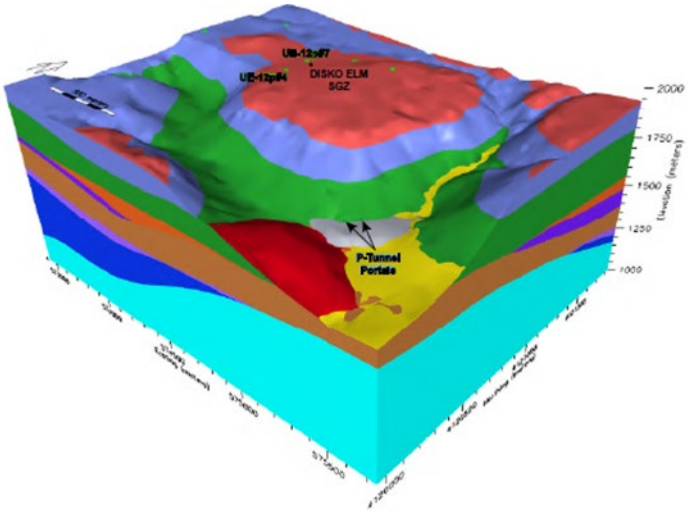

Figure 2. View of the UNESE GFM.

A transition zone between unaltered vitric tuffs above to zeolitic tuffs below is common within the volcanic rock section at the NNSS and can range from sharp to gradational, with alternating beds of vitric and zeolitic tuffs. In the P-Tunnel area, the transition between vitric and zeolitic rocks occurs over an interval of approximately 12 m and is characterized by alternating beds of vitric, zeolitic, and lesser silicic beds. The PE1 testbed is in the general vicinity this transition zone.

GFM Layer	Stratigraphic Unit(s)[1]	Basic Lithology	General Physical Properties[2]
Muck pile deposits (MPD)	na	Mined material consisting of vitric and zeolitic nonwelded tuff.	Low density, poorly consolidated material.
Alluvial deposits (AD)	Qc, Qal	Tuffaceous sands, gravels, and colluvium.	Low density and high porosity. Poorly fractured.
Landslide deposits (LD)	Qls	Blocks of welded tuff.	Relatively high density and low porosity. Well fractured.
Upper nonwelded to partially welded tuff (UNPWT)	Tma, Tmab, Tmr	Vitric nonwelded to partially welded ash-flow tuff and bedded ash- and pumice-fall deposits.	Relatively low density and high porosity. Typically poorly to moderately fractured.
Upper welded tuff (UWT)	Tmr	Devitrified welded ash-flow tuff.	Relatively high density and low porosity. Moderately to well fractured.
Vitric nonwelded tuff (VNT)	Tmr, Tmrh, Th, Tw	Vitric nonwelded ash-flow tuff, and bedded ash- and pumice-fall deposits and reworked tuff.	Relatively low density and high porosity. Typically poorly fractured.
Upper zeolitic nonwelded tuff (UZNT)	Tc	Zeolitic bedded ash- and pumice-fall deposits.	Relatively moderate density and high porosity. Typically poorly to moderately fractured.
Middle welded tuff (MWT)	Tbg	**Devitrified welded ash-flow tuff.**	**Relatively high density and low porosity. Moderately to well fractured.**
Middle zeolitic nonwelded tuff (MZNT)	Tn	Zeolitic bedded ash- and pumice-fall deposits.	Relatively moderate density and high porosity. Typically poorly to moderately fractured.
Lower welded tuff (LWT)	Tub	Devitrified welded ash-flow tuff.	Relatively high density and low porosity. Moderately to well fractured.
Lower zeolitic nonwelded tuff (LZNT)	To	Zeolitic bedded ash- and pumice-fall deposits.	Relatively moderate density and high porosity. Typically poorly to moderately fractured.
Precambrian siliciclastic rocks (PcS)	Zws	Siltstone, sandstone, and quartzite.	Relatively high density and low porosity. Well fractured.
Paleozoic carbonate rocks (PzC)	O - D	Dolomite.	Very high density and very low porosity. Well fractured.

Figure 3. Descriptions of the geologic layers that make up the GFM. The PE1 testbed lies near the VNT-UZNT transition.

The rocks encountered in P-Tunnel were originally grouped into informal local underground mapping units designated, from oldest to youngest, MC-0 through MC-4. These designations were based on visual and physical characteristics that were easily observed at the field mapping scale to facilitate underground geologic mapping and correlation as new drifts were constructed. These informal P-Tunnel mapping units have been superseded by model layer designations in the Underground Nuclear Explosives Signatures Experiment (UNESE) Geologic Framework Model (GFM) (Prothro 2018) [16]. In the PE1 area, MC-3 generally correlates to the upper portion of the upper zeolitic non-welded tuff (UZNT) and MC-4 to the vitric non-welded tuff (VNT) model layer (Figure 4). To accommodate anticipated higher fidelity geologic mapping at the PE1 testbed, the VNT unit has been subdivided into several smaller units designated numerically (increasing with depth).

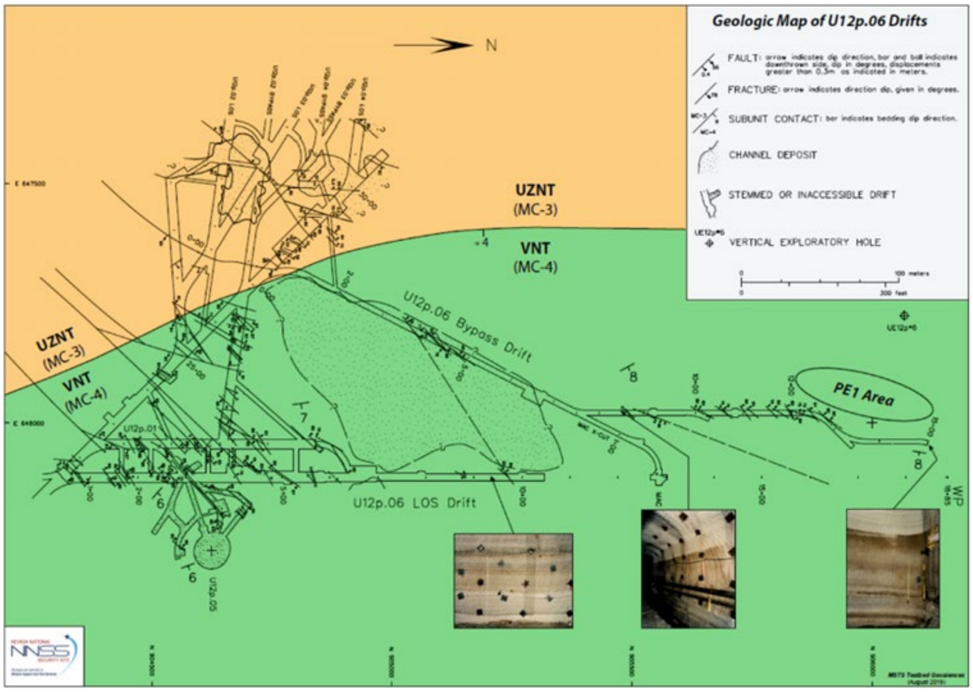

Figure 4. Map of the northern P-Tunnel. The contact between VNT (formerly MC-4) and UZNT (formerly MC-3) is shown in relation to the PE1 testbed location. See discussion above about recent updates to these designations.

2.1. LiDAR

Detailed tunnel infrastructure data has been captured by multiple light detection and ranging (LiDAR) scans of the mined areas. LiDAR data was first collected in the U12p.06 Bypass drift before construction of the PE1 testbed (Figure 5).

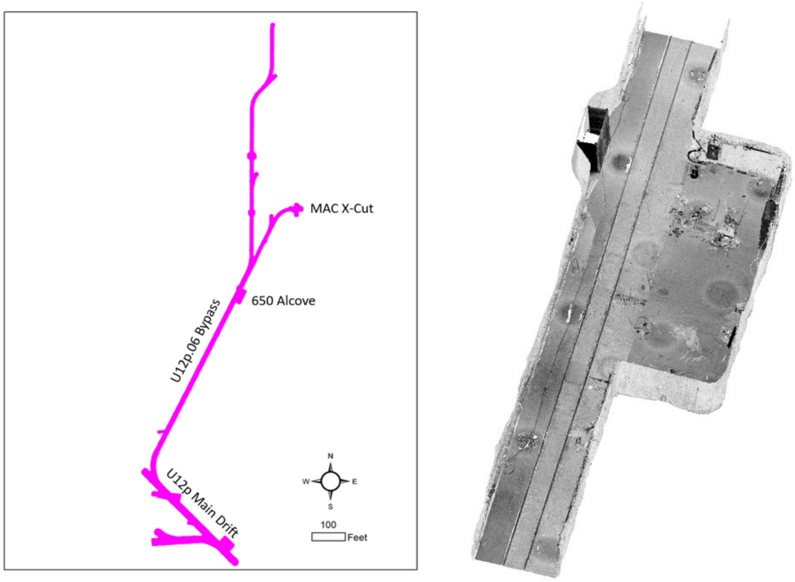

Figure 5. (Left) Top-down view of the LiDAR collected for the U12p.06 Bypass (before mining of the drifts). (Right) Closer view of the 650 Alcove.

LiDAR scans were also made after mining the 1490, 1280, and 1190 drifts. Figure 6 shows an example of the scans for the 1190 drift. The scan data clearly shows many of the notable features of the drift, including keyways, rock bolts, alcoves, and the geologic layers. Other features such as nearby workers and equipment were also captured by the scans but were removed from the raw dataset, leaving just the relevant features. Additionally, obvious outliers in the data have been removed to create a cleaned point cloud. The geolocation of the data was validated by manually confirming the location of multiple surveyed targets along the drifts.

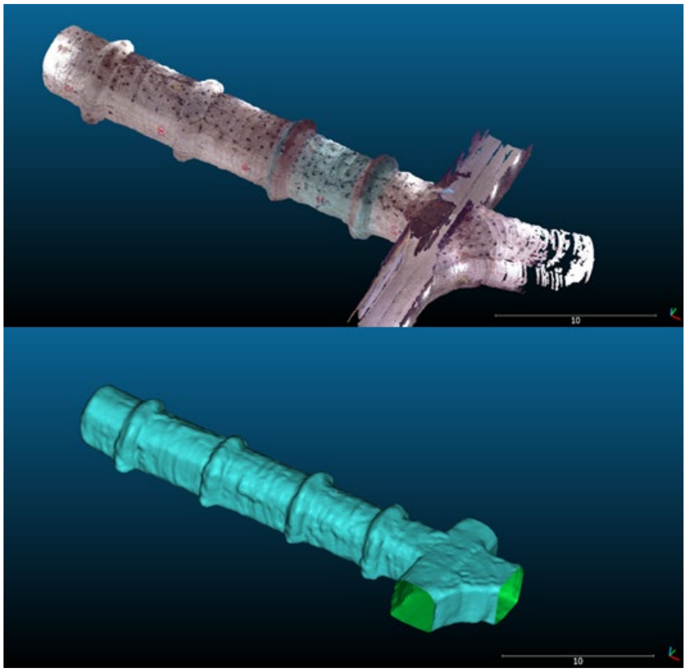

Figure 6. Example of available LiDAR data. Above images are from the 1190 drift. (Top) View of the point cloud data, (Bottom) Interpolated surface.

A LiDAR scan of the 1490 drift was completed as quickly as possible after mining the drift, 23 days after mining completion and 50 days from the start of mining. We also performed a second scan of the 1490 drift twelve days after the first scan. This rapid repetition was done so that the two datasets could be compared and analyzed for relaxation post mining. This analysis has not been completed yet.

The testbed has changed significantly since the time of the initial U12p.06 Bypass scan. A follow-up scan that covers the entire Bypass drift north of Facility 650, including the MAC crosscut, was completed in February of 2023. This dataset is being processed similar to and merged with the individual drift data described above.

2.2. Boreholes

Twenty-four boreholes were drilled in the testbed before Experiment A (Table 1).

Table 1. Borehole collar locations, starting angles and lengths

Borehole	Collar Location (NAD27: °State Plane feet)			Azimuth (°)	Starting Dip (°)	Drilled Length (ft)
	Northing	Easting	Elevation			
AC-1	906039.2	648034.0	5518.1	328	-39	167
AC-2	906077.8	648034.0	5524.5	315	44	120
AC-5	906004.3	648033.7	5521.5	294	6	116.5
DA-1	906068.0	648038.8	5516.1	0	-90	37
DA-2	905863.4	647979.0	5515.6	0	-90	37
DA-3	905759.3	647978.5	5515.5	0	-90	37
DA-4	905675.4	647978.5	5515.0	0	-90	37
DA-5	905544.8	647978.5	5514.3	0	-90	37
DA-6	905467.3	647978.5	5514.5	0	-90	37
DA-7	905356.2	647963.7	5514.0	0	-90	37
GS-1	906088.6	648033.5	5521.4	293	-6	57.5
GS-2	906088.4	648033.7	5523.5	294	8	58
GS-3	906036.1	648033.8	5520.3	297	-12	60.5
GS-4	906036.7	648033.9	5523.0	299	20	63
GS-5	906032.8	648033.8	5519.4	248	-20	60.5
GS-6	906032.1	648033.6	5523.4	251	32	64.5
GS-7	906115.1	648037.0	5520.0	308	-10	13
GS-8	906114.1	648044.7	5523.6	24	38	54
HF-1	906116.2	648037.5	5521.1	313	-1	84
GI-2	906108.7	648034.8	5521.3	300	-3	79.5
GI-3	905911.5	647994.7	5521.3	315	-2	60
GI-4	905822.8	647973.3	5521.2	270	0	84.5
GI-5	905969.0	647930.9	5520.4	312	-1	20
GI-6	905821.3	647888.3	5521.1	27	-1	116.5

These include:

- Three near-source accelerometer boreholes (AC)
- Seven drift accelerometer boreholes (DA)
- Eight gas sampling boreholes (GS)
- One hydrofracture borehole (HF)
- Five geologic investigation boreholes (GI)

Not included in this number are seven practice boreholes (PH) drilled in the U12p Tunnel Vent drift for evaluation of drilling and instrument installation techniques. All boreholes are nominally 4.8 inches in diameter (PQ size).

The final as-built configurations of the boreholes were determined using the surveyed collar locations (Table 1) along with data from measurements of the borehole path ("deviation" data) (Figure 7). Inconsistencies in the deviation data were observed for AC-1, resulting in a ~5 ft uncertainty at Total Depth (TD).

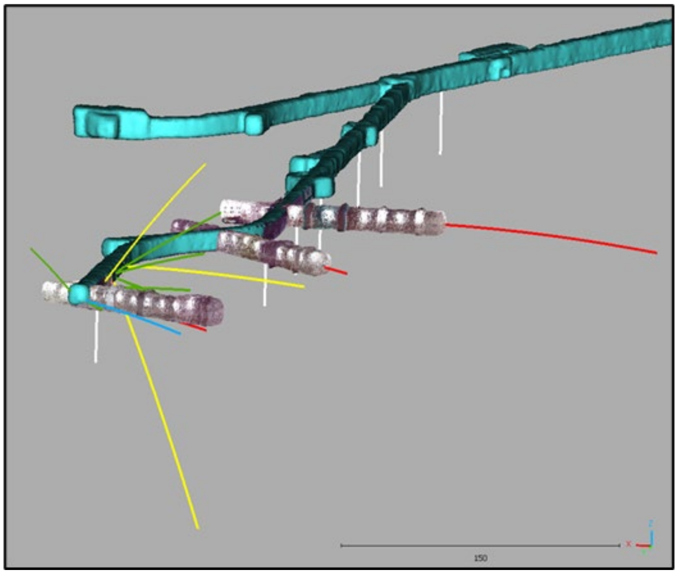

Figure 7. Borehole trajectories merged with LiDAR. Red: Geologic Investigation boreholes; Green: Gas Sampling boreholes; White: Drift Accelerometer boreholes; Blue: Hydrofracture borehole; Yellow: Near-Source Accelerometer boreholes. View is to the SE.

The GI-2, -3, and -4 boreholes were drilled along the paths of the 1490, 1280, and 1190 drifts, respectively, prior to mining of the drifts. Thus, these boreholes no longer exist in the testbed prior to Experiment A, as they were mined out during the drift construction.

2.3. Rock Bolt Catalogue

The 1190, 1280, and 1490 drifts required rock bolting for safe operations. These rock bolts were catalogued using the available LiDAR data as well as visual inspection. Rock bolt locations refer to the bolt's location along the drift interface. Rock bolts are assumed to be drilled perpendicular to the drift surface for the purposes of 3D modeling (Figure 8). Rock bolts of different lengths were used, short (1 to 6 ft) and long (8 ft), and were either fiberglass, rebar, or split-set bolts.

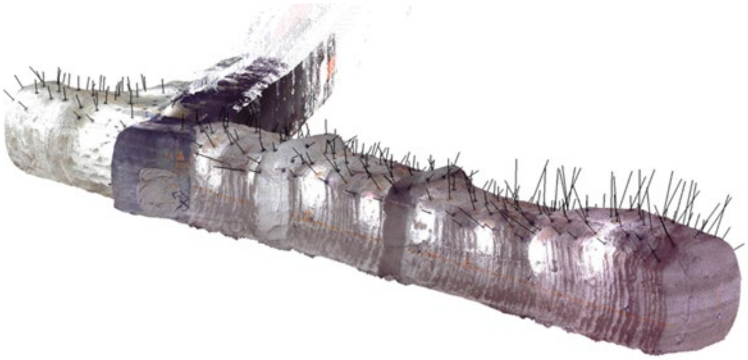

Figure 8. LiDAR with modeled rock bolt catalogue data. Rock bolt extents and angles are estimated from the existing data.

3. GEOLOGIC MAPPING

Geologic mapping was conducted both underground, focusing on the newly mined drifts, and on the Mesa surface, focusing on instrument installation locations. The goal of underground mapping was to identify lithologic contacts, categorize the severity of fractures (i.e., potential fast gas pathways), and collect additional rock properties. The goal of surface mapping was to photograph, document, and identify the geologic conditions at locations where surface instrumentation was emplaced to better understand the site characteristics.

3.1. Geologic Units

The PE1 testbed is located near the transition from VNT to UZNT, with the rock exposed during mining located entirely within the VNT unit. The VNT unit is highly heterogeneous, comprising of alternating beds of ash-fall and pumice-fall tuffs, as well as regions of reworked tuff (Figure 9). To account for this heterogeneity, the VNT unit has been subdivided into smaller units corresponding to these various deposits. Significant heterogeneity may still exist within these subunits in a more gradational state.

Layer VNT-1 represents the uppermost layer of the VNT subunits exposed in the drifts, and the numerical designation increases with depth. In total, ten VNT units were identified in this way above the lithologic contact with UZNT. UZNT was not subdivided, as the unit is much more homogenous than the VNT and the data we have sampling UZNT is too sparse to make further distinctions. Up-going boreholes have sampled additional VNT layers, which can be identified and are designated with an alphabetic label (ex. VNT-A). Labeling is done in this manner because we do not know the exact number of sublayers that exist above the testbed and below the upper welded tuff (UWT).

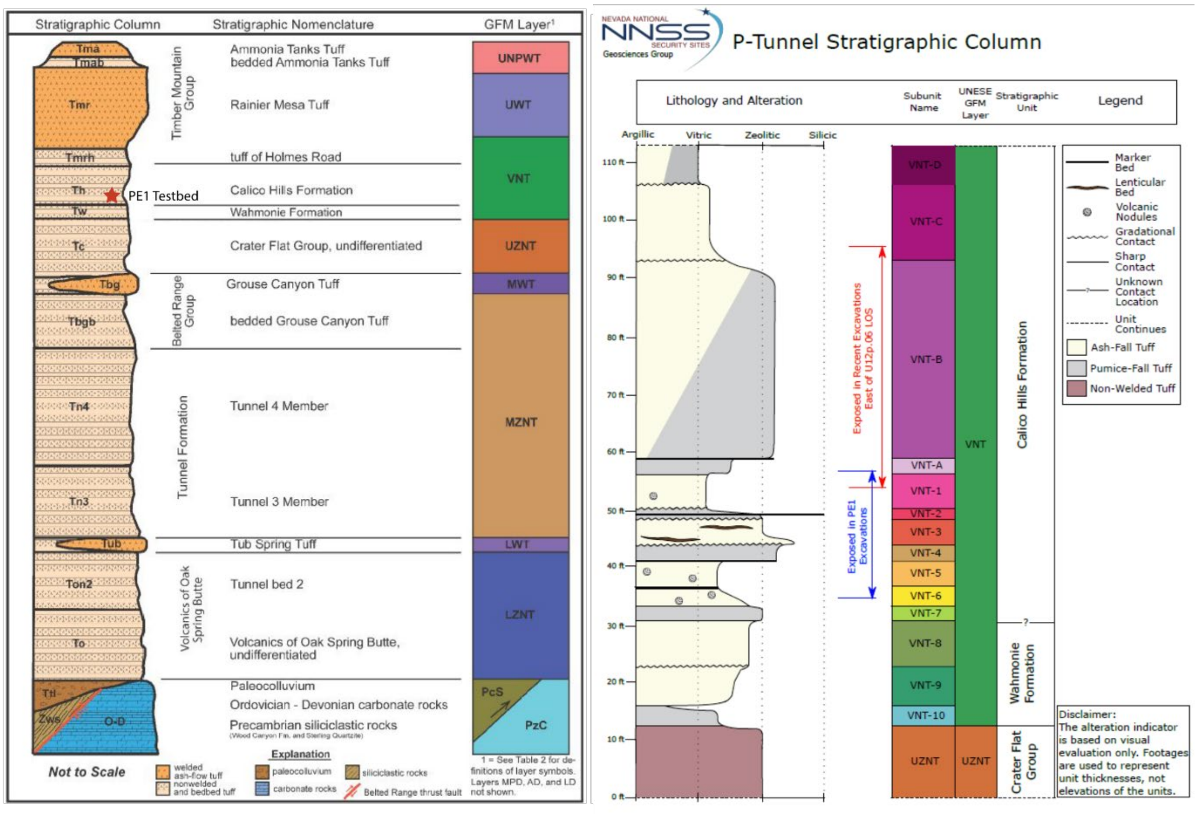

Figure 9. Stratigraphic cross sections of the PE1 testbed. (Left) The full Aqueduct Mesa cross section. The PE1 testbed lies within the VNT unit marked with a red star. (Right) A detailed cross section of the subunits that make up the PE1 testbed.

Generalized, brief descriptions of the identified units and subunits are as follows:

Table 2. Descriptions of the identified geologic units near and around the PE1 testbed. Thicknesses are approximate and are based on the available borehole core. Descriptions are based on visual inspection of whole core samples.

Unit	Approx. Avg. Thickness (ft)	Main Lithology	Description
VNT-D	>10	Pumice-fall tuff	Mostly vitric interbedded pumice-fall tuff and ash-fall tuff
VNT-C	15.1	Ash-fall tuff	Fine-grained, mostly vitric
VNT-B	21.4	Ash-fall tuff	Mostly vitric interbedded ash-fall and pumice fall tuff
VNT-A	2.3	Pumice-fall tuff	Coarse to very coarse, vitric
VNT-1	18.0	Ash-fall tuff	Fine grained, vitric
VNT-2	3.3	Pumice-fall tuff	Vitric, becoming zeolitic and silicified lower
VNT-3	4.7	Ash-fall tuff	Vitric, becoming zeolitic and silicified lower
VNT-4	2.6	Pumice-fall tuff	Mostly zeolitic, vitric at top and partially vitric at base; partially silicified

Unit	Approx. Avg. Thickness (ft)	Main Lithology	Description
VNT-5	6.9	Ash-fall and reworked tuff	Mostly vitric, with some partially zeolitic intervals
VNT-6	3.8	Ash-fall tuff	Mostly vitric, grading to more zeolitic lower
VNT-7	3.7	Pumice-fall tuff	Very coarse grained. Mostly zeolitic, locally vitric. Similar to VNT-4, but without silicified interbedding.
VNT-8	6.1	Ash-fall tuff	Fine-grained. Mostly vitric, with zeolitic alteration grading in and out. Gradational with VNT-9
VNT-9	10.9	Ash-fall tuff	Fine-grained. Mostly vitric, with zeolitic alteration grading in and out. Very abundant euhedral biotite
VNT-10	2.1	Pumice-fall tuff	Coarse-grained, “salt and pepper”. Mostly vitric with weak zeolitic and local alteration.
UZNT	>50	Non-welded tuff	Mostly zeolitic, bedded and massive tuff

3.2. Underground Mapping

The 1190, 1280, and 1490 drifts were mapped and characterized using a variety of techniques following the completion of pre–Experiment A mining. These included photography, lithologic interpretation, and hardness measurements.

Multiple photographs were taken of the southern (“left”) ribs and were subsequently compiled using photo stitching (Figure 10). The resulting image spans the entire rib from the U12p.06 Bypass to the drift face. These images were used in conjunction with notes from visual inspection to identify the continuous contacts between the VNT sub-units. These interfaces are also used to generate a simplified lithology map of the 1190, 1280, and 1490 drifts.

3.3. Schmidt Hammer

Schmidt hammer measurements, which can be used to obtain a qualitative rock hardness, were performed on the left (south) ribs of the 1190, 1280, and 1490 drifts to help characterize the exposed VNT units. The performance of the Schmidt hammer (L-Type) was first verified using a testing anvil to ensure proper performance range. Measurements were made on every accessible VNT sub-unit along the drift at approximately 20 ft intervals (Figure 11). Test locations were selected to try to obtain values for each exposed VNT unit but were limited by how accessible the planned locations were.

Even though Schmidt Hammer data have been used to estimate other rock properties (e.g., strength), a more appropriate use in investigations like this, with few measurements in a variable medium, is to use them to compare visibly different units (Table 3). The VNT-2 subunit shows the highest relative strength as estimated from Schmidt Hammer measurements, although standard deviations between rebound values imply a wide range of variability. VNT-1, -3, -4, -5, and -6 have similar rebound values and differing ranges of variability between values.

Table 3. Average Schmidt Hammer values for the U12p06 1190, 1280, and 1490 drifts.

Unit	Number of Measurements	Average Schmidt Hammer Number (standard deviation in parentheses)
1490 Drift		
VNT-1	2	27 (1.0)
VNT-2	3	54 (4.1)
VNT-3	4	27 (0.7)
VNT-4	2	23.5 (1.5)
VNT-5	1	24
1280 Drift		
VNT-1	2	27.5 (2.5)
VNT-2	2	59 (5)
VNT-3	4	30.5 (1.1)
VNT-4	3	34 (6.2)
VNT-5	2	35 (4.0)
VNT-6	1	33
1190 Drift		
VNT-1	1	25
VNT-2	1	59
VNT-3	3	30 (3.0)
VNT-4	3	37 (3.9)
VNT-5	2	27 (0.7)
VNT-6	1	25

U12p.06 1190 Drift Left (South) Rib Lithology and Fracture Map

03 March 2022

The four-digit number in the drift name refers to the construction station at the point where the drift intersects the U12p.06 Bypass drift.

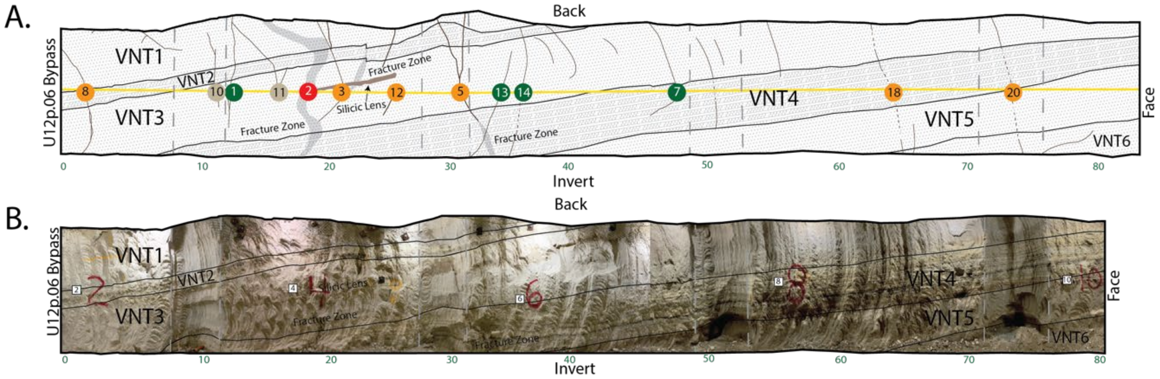

U12p.06 1280 Drift Left (South) Rib Lithology and Fracture Map

03 March 2022

The four-digit number in the drift name refers to the construction station at the point where the drift intersects the U12p.06 Bypass drift.

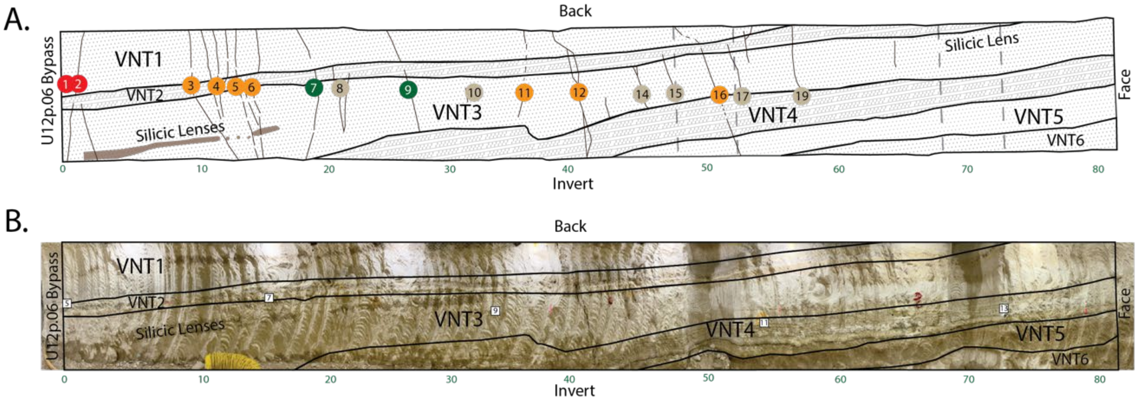

U12p.06 1490 Drift Left (south) Rib Lithology and Fracture Map

07 January 2021

The four-digit number in the drift name refers to the construction station at the point where the drift intersects the U12p.06 Bypass drift.

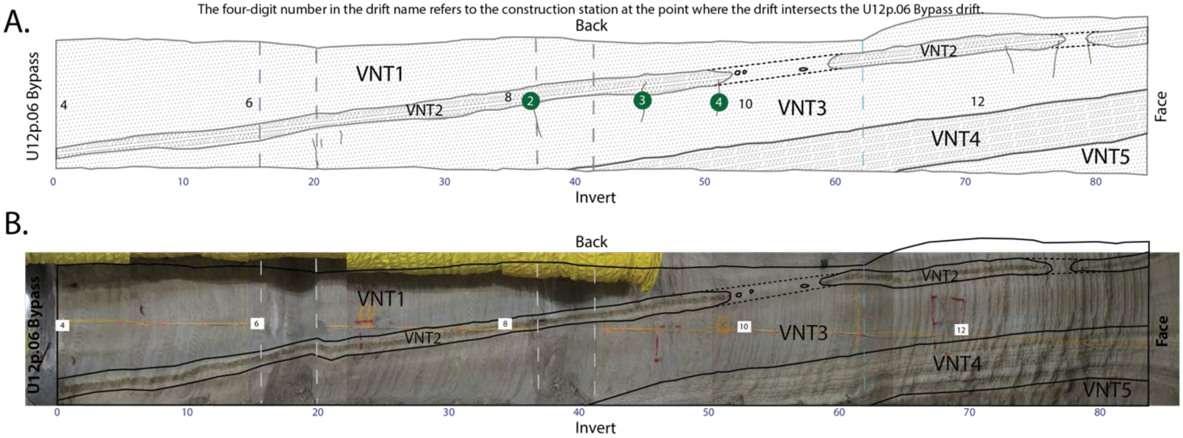

Figure 10. Rib maps of the southern (left) rib of the 1190, 1280, and 1490 drifts. Upper panels (A) show the simplified lithologic interpretation along with fracture categorization. Numbered circles are used to uniquely identify fractures and are color coded by their severeness (see Table 4). Bottom panels (B) show the stitched-together photo mosaics of the rib walls with lithologic interpretations overlain. Note that these flattened views result in some distortion, giving unrealistic bedding dips, particularly around the keyway locations and near the face. These maps should not be used for direct measurement.

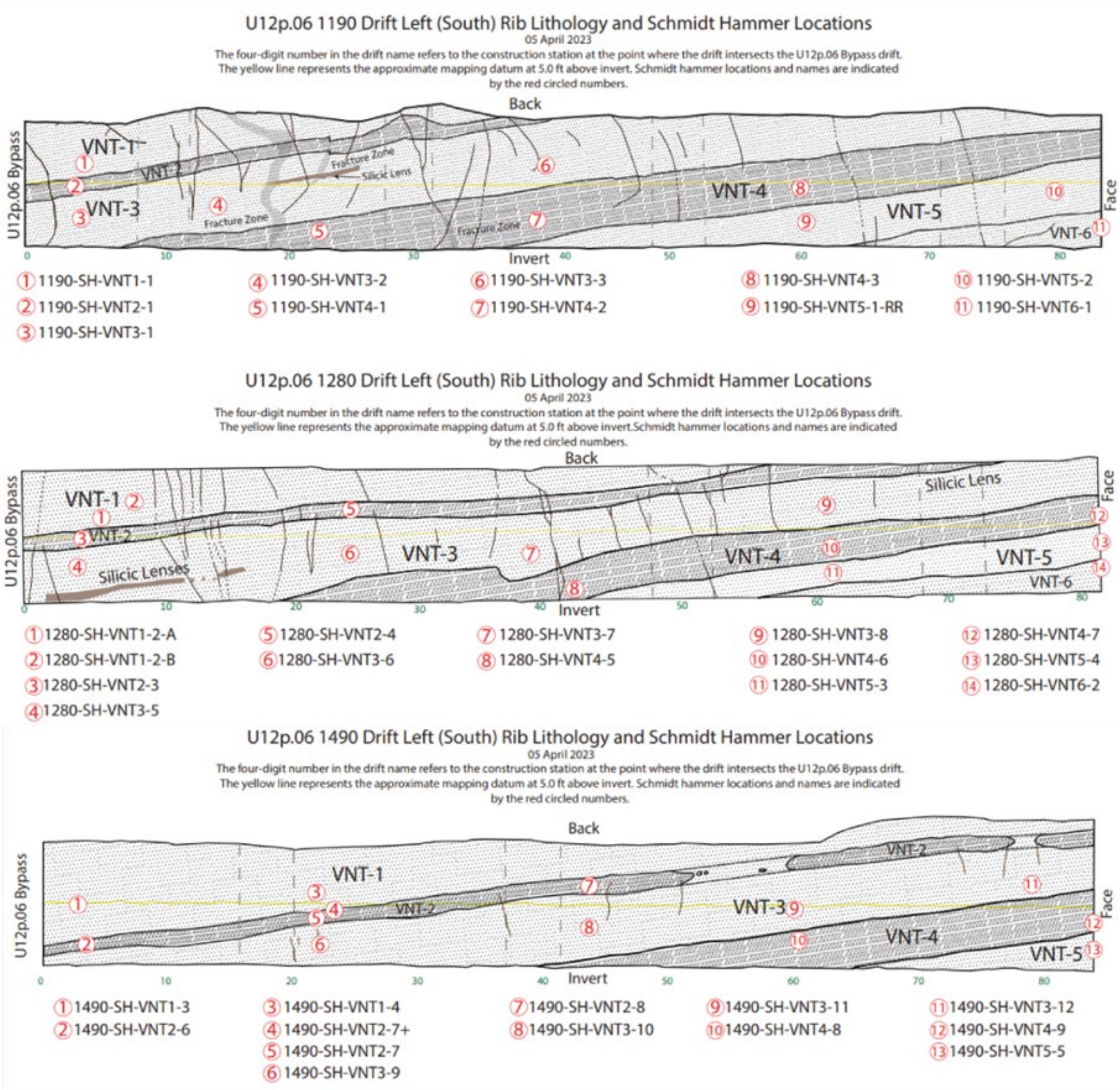

Figure 11. Locations for Schmidt hammer measurements superimposed on rib maps for the 1190, 1280, and 1490 drifts.

3.4. Fractures

Fractures were identified in the 1190, 1280, and 1490 drifts from visual inspection; their locations on the south ribs are shown in Figure 10. Fractures were also mapped on the north ("right") rib and back (ceiling) of the drifts to characterize the 3D distribution of the fast pathways within the local area. Fractures that could be traced on multiple surfaces of the drift were interpolated into local fracture planes with associated strike and dip angles (Figure 12). These newly defined fracture orientations were compiled with existing fracture maps of the U12p.06 Bypass drift to give a testbed-wide characterization of known fast pathways.

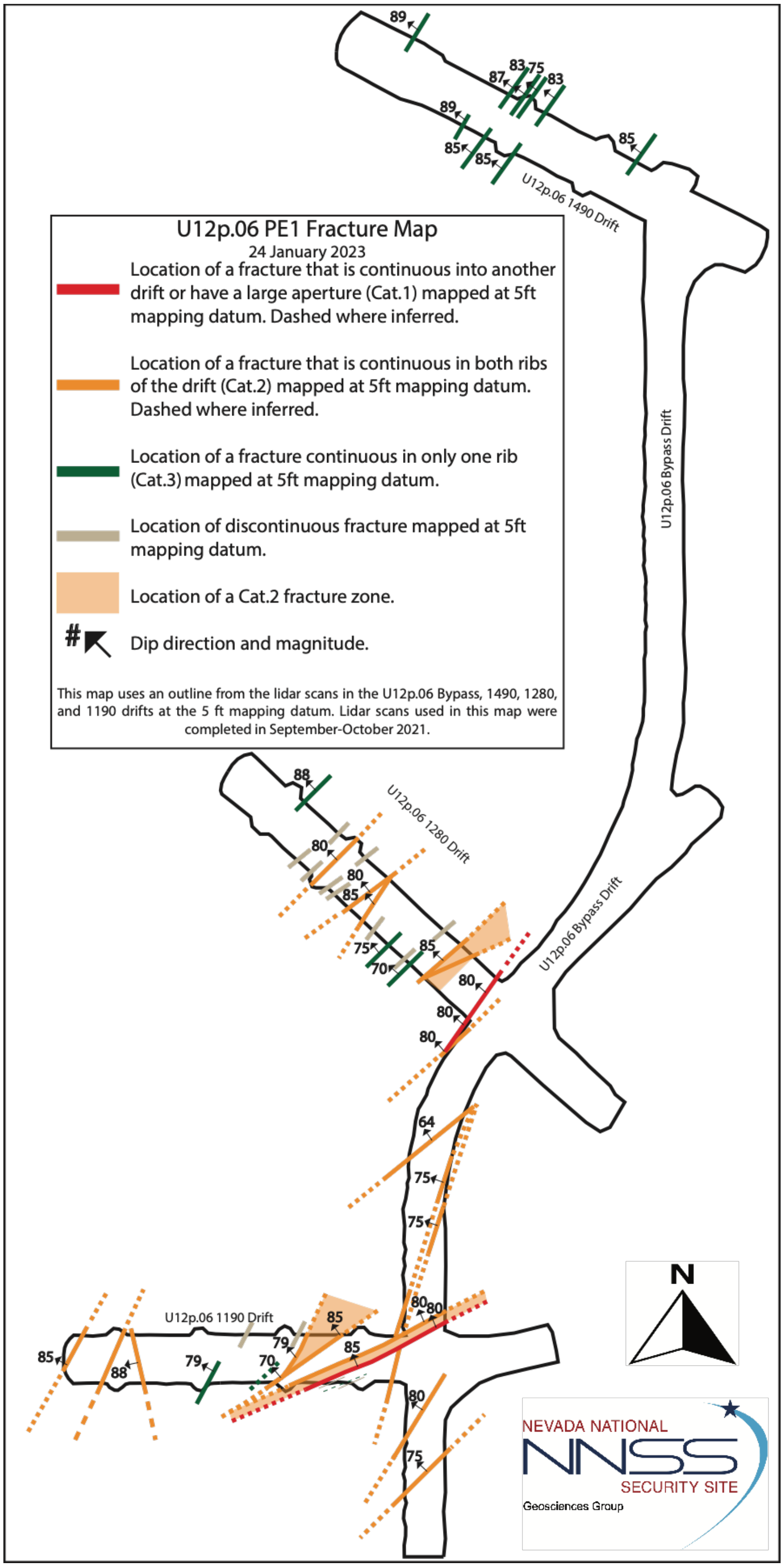

Figure 12. Mapped fractures in the PE1 testbed. Fractures are depicted as lines indicating strike direction with an associated dip and are overlain on a top-down view of the PE1 testbed drifts. All fractures are mapped at a datum of 5 ft above the invert (floor).

Fractures were further characterized into three categories denoting their severity and perceived amount of effort needed to confine them prior to the explosive experiments. The categories are defined as follows:

Table 4. Description of the fracture severity categories used in underground mapping and appearing on Figure 9.

Category	Features	Remediation
Cat. 1	Aperture at tunnel wall 30 mm or more Multiple associated planes Visible across drift (e.g., both ribs and back) Crosses more than one lithology Correlates with mapped fractures in other drifts (based on orientation and other characteristics)	Investigate Options for Sealing
Cat. 2	Aperture at tunnel wall >5 mm but <30 mm Visible across drift (e.g., both ribs and back) Notable mainly in brittle lithologies, and may die out in less brittle ones May correlate with fracture in nearby a borehole, but not another drift (based on orientation and other characteristics)	Cover with Shotcrete
Cat. 3	Aperture at tunnel wall ≤5 mm Does not cross drift (e.g., both ribs and back) Notable mainly in brittle lithologies and may die out in less brittle ones No apparent correlation with any fractures in nearby boreholes or drifts (based on orientation and other characteristics)	Ignore

In general, fractures are observed trending northeast-southwest, except for a nearly north-south trending fracture between the 1190 and 1280 drifts in the U12p.06 Bypass drift and a northwest-southeast trending fracture near the face of the 1190 drift, adjacent to other northeast-southwest fractures. Fractures tend to be steeply dipping to the northwest, with most fractures angled 70° to 85° from horizontal.

Fractures are more numerous and severe in the southern portion of the testbed (Figure 10 and Figure 12). The 1490 drift only contains nine Cat. 3 fractures, while as many as eleven Cat. 1, 2, and 3 fractures were mapped in the 1280 and 1190 drifts. In the 1280 drift, the most severe fractures are observed near the U12p.06 Bypass drift, and no fractures are observed in the last 20 ft of the drift. In the 1190 drift, two sets of Cat. 1 fractures were observed ~20 ft from the U12p.06 Bypass drift, and Cat. 1 and 2 fractures are present near the face of the drift.

3.5. Surface Mapping

Surface mapping was completed over a week-long campaign in 2022 after the surface instrumentation had been deployed (Figure 13). A list of station sites on Aqueduct Mesa was evaluated (Gaylord 2021) [3], and a subset (14 sites from 32) was selected to be mapped.

Each site was visited to observe its general topographic orientation, vegetation cover, and surface geology. The sites were located by spotting the telemetry equipment installed at each location. From the telemetry equipment, each sensor cable was traced to the sensor installation location, noting the general surficial features along the way. The length of the cable traces varies from several meters to hundreds of meters. The area investigated at each site encompassed all the sensor locations. For smaller installations, the investigation area spanned a radius of at least 50 meters. No unusual or unexpected surficial geologic features were observed at any of the sites that were visited.

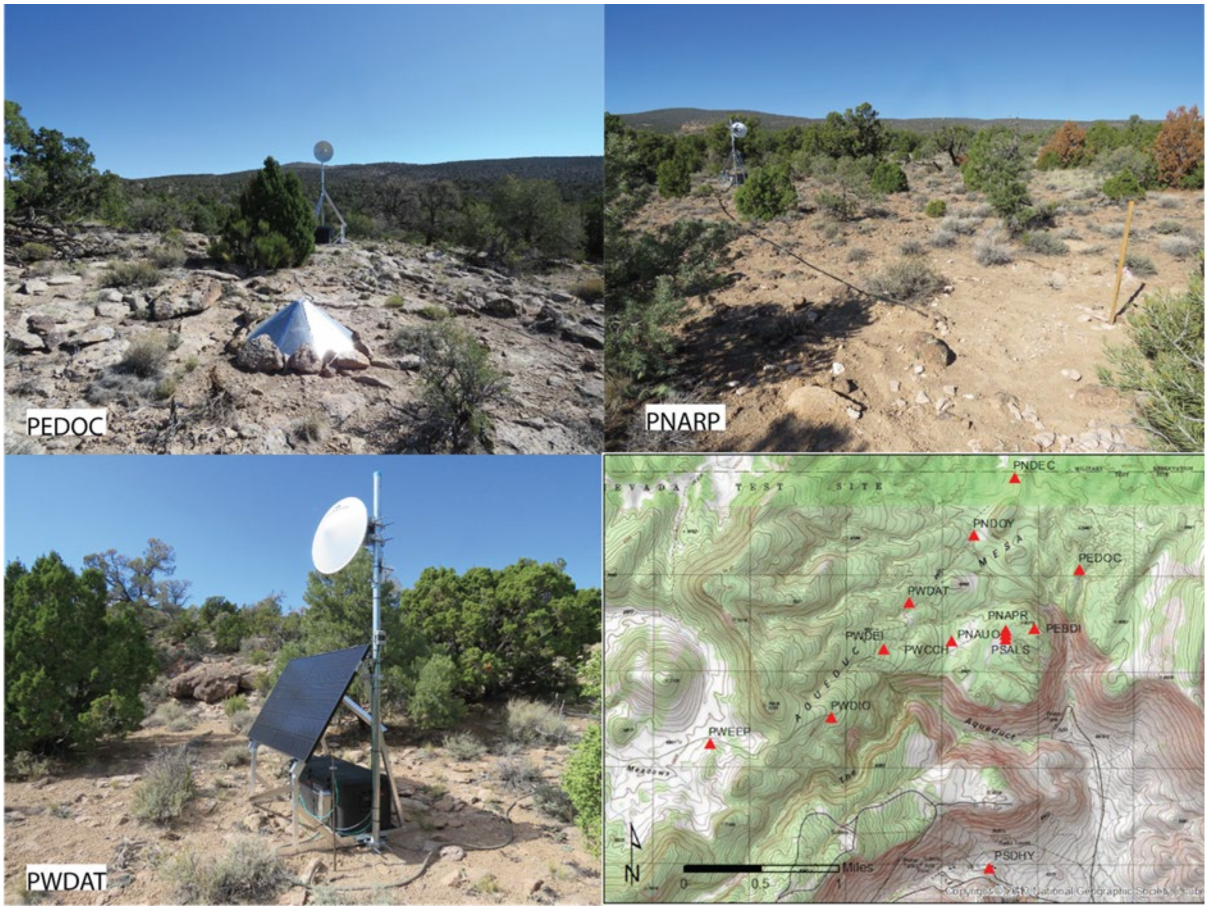

Figure 13. Example photos from three of the surface sites visited (PEDOC: upper left; PNARP: upper right; and PWDAT: lower left). PEDOC shows an infrasound sensor and telemetry looking east. PNARP shows a seismic site looking west, with telemetry and a cable leading to a geophone. PWDAT shows a seismic site looking west; telemetry is visible, which connects to multiple geophones. (Bottom Right) Displays a map of the visited sites.

A high-resolution digital elevation map (DEM) of Aqueduct Mesa was generated for the UNESE project (Vigil 2016) [21] and has been obtained for use in PE1 (Figure 14). This DEM has a horizontal pixel size of ~7.5 cm with +/- 3 cm vertical accuracy.

Figure 14. Map showing the extent of the high-resolution DEM (blue rectangle). The overhead image is taken from Google Maps. Also shown is a contour map overlay that shows the extent of the interior P-Tunnel complex prior to construction of the PE1 testbed.

Additionally, surveys were done on Aqueduct Mesa for the three locations on the surface directly above the emplacement locations for Experiments A, B, and D_L (Surface Ground Zero (GZ)). A summary of those points and the calculated overburden above the experiment locations is found in Table 5.

Table 5. Surveyed locations directly above the experiment emplacement points on Aqueduct Mesa and the calculated overburden.

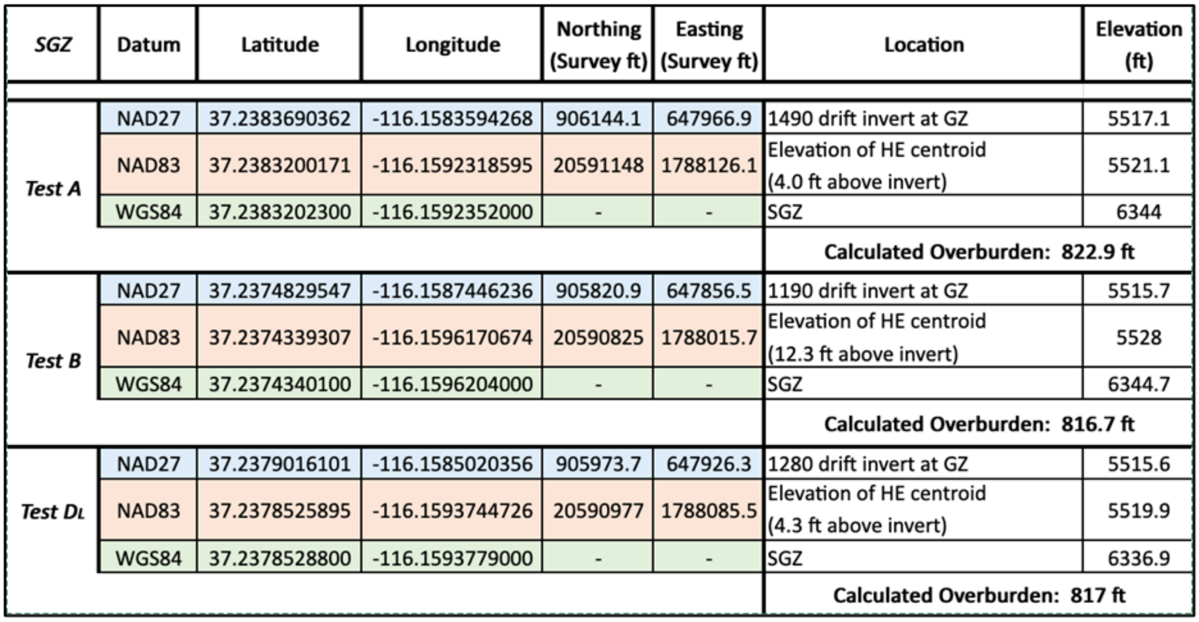

SGZ	Datum	Latitude	Longitude	Northing (Survey ft)	Easting (Survey ft)	Location	Elevation (ft)
Test A	NAD27	37.2383690362	-116.1583594268	906144.1	647966.9	1490 drift invert at GZ	5517.1
	NAD83	37.2383200171	-116.1592318595	20591148	1788126.1	Elevation of HE centroid (4.0 ft above invert)	5521.1
	WGS84	37.2383202300	-116.1592352000	-	-	SGZ	6344
						Calculated Overburden: 822.9 ft	
Test B	NAD27	37.2374829547	-116.1587446236	905820.9	647856.5	1190 drift invert at GZ	5515.7
	NAD83	37.2374339307	-116.1596170674	20590825	1788015.7	Elevation of HE centroid (12.3 ft above invert)	5528
	WGS84	37.2374340100	-116.1596204000	-	-	SGZ	6344.7
						Calculated Overburden: 816.7 ft	
Test D_L	NAD27	37.2379016101	-116.1585020356	905973.7	647926.3	1280 drift invert at GZ	5515.6
	NAD83	37.2378525895	-116.1593744726	20590977	1788085.5	Elevation of HE centroid (4.3 ft above invert)	5519.9
	WGS84	37.2378528800	-116.1593779000	-	-	SGZ	6336.9
						Calculated Overburden: 817 ft	

Underground locations are typically reported in NAD 27, while surface locations are often in WGS 84. Compounding conversion errors or failing to convert all data to a base system can result in significant offsets and must be handled carefully.

This page left blank

4. BOREHOLE DRILLING AND CORE COLLECTION

A total of 24 boreholes were drilled during PE1 testbed construction: three prior to the excavation of the three access drifts, and 21 after mining (Phase I boreholes). Of the Phase I boreholes, six were drilled primarily for geologic characterization, and 18 were drilled for installation of instrumentation. Geophysical data, videos, and core samples from all the holes were examined to provide characterization data and to support installation and grouting of instrumentation. Table 6 presents basic information for all 24 holes, and the following sections present information about characterization data and notable features of each hole.

Table 6. Drilling information for the 24 boreholes drilled prior to Experiment A (note that U12p.06 GI-1 was drilled in 1992 and is not addressed here.)

Hole[1]	Starting Angle[2]	Drilled Depth (ft)	Depth of Casing[3] (ft from collar)	Drill Dates		Date of Geophysical Logging (Colog)
				Start	Finish	
GI-2	–3.0	79.4	None	02/02/2021	02/08/2021	03/04/2021
GI-3	–1.5	60.0	None	02/17/2021	02/21/2021	03/04/2021
GI-4	0	84.5	None	03/10/2021	03/18/2021	03/23/2021
GI-5	–1.0	20.0	None	05/09/2022	05/10/2022	05/19/2022
GI-6	–1.0	116.5	None	05/12/2022	05/17/2022	06/07/2022
HF-1	–1.0	84.0	None	05/24/2022	05/25/2022	06/06/2022
AC-1	–39.0	167.0	5.0	01/18/2022	02/01/2022	02/15/2021
AC-2	+44.3	120.0	10.0	04/07/2022	04/21/2022	05/17/2022
AC-5	+5.6	116.5	10.0	02/02/2022	02/17/2022	05/19/2022
DA-1	–90	37.0	5.0	11/29/2021	12/01/2021	12/13/2021
DA-2	–90	37.0	5.0	10/18/2021	10/19/2021	12/16/2021
DA-3	–90	37.0	5.0	10/25/2021	10/27/2021	12/16/2021
DA-4	–90	37.0	5.0	11/03/3021	11/04/2021	12/16/2021
DA-5	–90	37.0	5.0	11/08/2021	11/09/2021	12/16/2021
DA-6	–90	37.0	5.0	11/15/2021	11/17/2021	12/15/2021
DA-7	–90	37.0	5.0	11/18/2021	11/22/2021	12/15/2021
GS-1	–5.6	57.5	5.0	12/21/2021	12/28/2021	02/14/2022
GS-2	+8.2	58.0	10.0	03/29/2022	04/04/2022	05/19/2022
GS-3	–11.9	60.5	5.0	12/30/2021	01/04/2022	02/15/2022
GS-4	+20.1	63.0	10.0	03/08/2022	03/10/2022	05/18/2022
GS-5	–19.7	60.5	5.0	01/06/2022	01/13/2022	02/15/2022
GS-6	+32.2	64.4	10.0	02/23/2022	03/03/2022	05/18/2022
GS-7	–10.3	13.0	5.0	12/15/2021	12/16/2021	02/14/2022
GS-8	+37.7	54.0	10.0	04/27/2022	05/05/2022	05/18/2022

1. For full name of all holes, add U12p.06, e.g., U12p.06 AC-1

Hole[1]	Starting Angle[2]	Drilled Depth (ft)	Depth of Casing[3] (ft from collar)	Drill Dates		Date of Geophysical Logging (Colog)
				Start	Finish	

2. Angle given in degrees from horizontal
3. Zero point for collars of all holes is at rib line.

Geologic core samples were collected from all the drilled boreholes. The boreholes were drilled using a special bit that produced a HQ-size core (2.5 in. diameter) but created a PQ-size hole (4.8 in. diameter). This drilling facilitated collection of geologic core samples of convenient size for analysis but still facilitated the conveyance of borehole instrumentation. Recovery statistics can be found in Table 7. Recovery was generally greater than 80%, except for GI-2, which was the first borehole drilled for the experiment and encountered complications with the newly purchased drill rig which were resolved for subsequent boreholes.

For many of the boreholes, particularly those designated for site characterization use, a subset of the core was preserved in layers of foil and wax to preserve the in situ water content. The collected core was inventoried and relocated to the United States Geological Survey (USGS) Core Library at NNSS for storage and management. High resolution photographs of the samples were taken at the Core Library in both dry and wet conditions (Figure 15).

Table 7. Recovery, rock quality designation (RQD), and preservation statistics for all the PE1 boreholes.

Borehole	Recovery	Loss	Sound	RQD	% Recovery	% Preserved
AC-1	166.6	0.4	154.2	92.3	99.7	9.2
AC-2	112.5	7.5	91.8	76.5	93.8	6.8
AC-5	110.8	5.7	90.0	77.3	95	0
DA-1	35.8	1.2	27.9	75.4	97	6.7
DA-2	29.8	7.2	21.1	57.0	81	0
DA-3	30.1	6.9	22.0	59.5	81	0
DA-4	34.3	2.7	21.5	58.1	93	0
DA-5	34.5	2.5	24.9	67.3	93	0
DA-6	31.6	5.4	20.8	56.2	85	0
DA-7	31.7	5.3	30.0	81.1	86	9.8
GS-1	51.9	5.6	32.3	56.2	90	0
GS-2	55.8	2.2	50.9	87.8	96	0
GS-3	60.0	0.5	40.5	66.9	99	8.3
GS-4	61.5	1.5	45.6	72.4	98	8.8
GS-5	59.6	0.9	49.1	81.2	99	7.4
GS-6	55.0	9.4	34.7	53.9	85	0
GS-7	12.9	0.1	5.7	43.8	99	0
GS-8	51.5	2.5	36.3	67.2	95	4.9

Borehole	Recovery	Loss	Sound	RQD	% Recovery	% Preserved
HF-1	83.3	0.7	52.4	62.4	99	2.8
GI-2	51.2	22.2	30.0	40.9	70	18
GI-3	56.4	3.6	35.4	59.0	94	11
GI-4	80.3	4.2	56.3	66.6	95	10
GI-5	19.7	0.3	13.8	69.0	98.5	11.2
GI-6	114.8	1.7	102.4	87.9	98.5	7.8

Figure 15. Example of the high-resolution photographs taken for the PE1 core in the USGS Core Library. This example is from the GI-2 borehole under dry conditions. Some samples are coated in wax to preserve water content.

This page left blank

5. BOREHOLE CHARACTERIZATION

Geophysical logs from the boreholes were used to inform operations essential to PE1, such as instrumentation emplacement, grouting implementation, and site characterization measurement locations. We identified notable features such as fractures, enlarged areas, water levels (residual from drilling), and hole geometry. These reviews relied heavily on core observations, borehole video runs, optical televiewer images, and caliper log data.

For each borehole we present observations, which include basic lithologic information. Note that fracture information listed for each hole is based on “quick-logs” of the core, and alteration information is based on visual evaluation rather than X-ray Diffraction (XRD) or Scanning Electron Microscopy (SEM) data. More detailed fracture analyses are available for a subset of cores and can be found in the Tabletop Core Measurements section.

5.1. Geophysical Logging

All boreholes were characterized using a suite of downhole tools to record geophysical log data (Table 8). All boreholes (including most practice holes) had a minimum set of logs run including video, gyroscopic deviation, optical televiewer, compensated density, and caliper. Additional logs such as full waveform sonic and acoustic televiewer were run on down-going holes that could hold water (excluding GS holes due to instrumentation concerns about adding additional water). Further, the GI holes had some additional logs such as neutron and induction and resistivity. A set of deviation logs were run by Colog for GI-2, -3, and -4; however, the desired gyroscopic tool was not available at the time and was substituted by a magnetic tool. Errors in the data led to these logs being omitted.

The suite of logs was run by two different groups. The first logs were run by the NNSS geologists, who ran video and deviation logs. These could be done quickly during and after each individual borehole was drilled. The second group was run by Colog (an NNSS subcontractor), who ran the remaining logs in batches as holes became available.

Equipment details are as follows:

- Video (NNSS): Hathorn 1.68-in. color self-leveling camera
- Deviation (NNSS): SPT GyroMaster
- Color Video (Colog): DGRT 02848 Wireline Digital Camera Multi View
- Deviation (Colog): SPT GyroMaster
- Density (Colog): Mt. Sopris Instruments HLP-4180
- Caliper (Colog): Mt. Sopris Instruments 2CCA-1000 – or the arm on the HLP-4180
- Neutron (Colog): Robertson Geologging DNNS
- Optical Televiewer (Colog): Mt. Sopris Optical Borehole Imager (OBI™) QL40 OBI/OBI 40 GR
- Induction (Colog): Robertson Geologging DUIN
- Acoustic Televiewer (Colog): QL40-ABI 111702 Acoustic Borehole Imager
- Natural Gamma (Colog): 2PEA-1000 PolyElectric probe
- Resistivity (Colog): Mt. Sopris Instruments 2PEA1000

- Full Wave-form Sonic (Colog): Mt. Sopris 2SAA (F)-1000 Multi-Frequency Full Wave-form Sonic

Table 8. List of logs run and available data (green X) for each borehole. Colog logs are highlighted in purple, while NNSS logs are highlighted in blue. (*) These boreholes had an additional Colog optical televiewer run following hydrofracture measurements.

Borehole	Color Video	Borehole Deviation	Compensated Density, Caliper	Neutron	Optical Televiewer	Natural Gamma	Induction	Acoustic Televiewer	Resistivity	Full wave-form Sonic	Deviation	Video Camera
GI-2	X	-	X	X	X	X	X	X	X	X	X	X
GI-3	X	-	X	X	X	X	X	X	X	X	X	X
GI-4	X	-	X	-	X	X	-	X	X	X	X	X
GI-5	X	X	X	-	X*		-	-	-	-	X	X
GI-6	X	X	X	-	X*		-	-	-	-	X	-
GS-1	X	X	X	-	X		-	-	-	-	X	-
GS-2	X	X	X	-	X		-	-	-	-	X	X
GS-3	X	X	X	-	X		-	-	-	-	X	X
GS-4	X	X	X	-	X		-	-	-	-	X	X
GS-5	X	X	X	-	X		-	X	-	-	X	X
GS-6	X	X	X	-	X		-	-	-	-	X	X
GS-7	X	X	X	-	X		-	-	-	-	X	X
GS-8	X	X	X	-	X		-	-	-	-	X	X
HF-1	X	X	X	-	X*		-	-	-	X	X	X
DA-1	X	X	X	-	X		-	X	-	X	X	X
DA-2	X	X	X	-	X		-	X	-	X	X	X
DA-3	X	X	X	-	X		-	X	-	X	X	X
DA-4	X	X	X	-	X		-	X	-	X	X	X
DA-5	X	X	X	-	X		-	X	-	X	X	X
DA-6	X	X	X	-	X		-	X	-	X	X	X
DA-7	X	X	X	-	X		-	X	-	X	X	X
AC-1	X	X	X	-	X		-	X	-	X	X	X
AC-2	X	X	X	-	X		-	-	-	-	X	-
AC-5	X	X	X	-	X		-	-	-	-	X	-
PH-1	-	-	-	-	-		-	-	-	-	X	X
PH-2	-	-	-	-	-		-	-	-	-	X	X
PH-3	-	-	-	-	X		-	-	-	-	X	X
PH-4	-	-	-	-	-		-	-	-	-	-	-
PH-5	-	-	-	-	X		-	-	-	-	X	X
PH-6	-	-	-	-	X		-	-	-	-	X	X
PH-7	-	-	-	-	-		-	-	-	-	X	X
U-15n-009	-	X	X	-	X		-	-	-	x	-	X

5.2. Geologic Logging

The following sections present summaries of geological and physical observations for each borehole, including basic lithologic information based on "quick-logs" of the core. Collar location and borehole trajectory information are provided in Table 6. An overview of the lithologies sampled by each borehole is shown in Table 9. See the Tabletop Core Measurements section for additional fracture characterization information.

Table 9: Chart of lithologies sampled (colored cells) for each borehole. In one case (DA-7) there is some ambiguity on what lithology is sampled due to a possible scour feature.

	VNT-D	VNT-C	VNT-B	VNT-A	VNT-1	VNT-2	VNT-3	VNT-4	VNT-5	VNT-6	VNT-7	VNT-8	VNT-9	VNT-10	UZNT	Scour?
GI-2					■	■	■	■	■							
GI-3						■	■	■	■							
GI-4						■	■	■	■							
GI-5									■							
GI-6									■	■	■	■	■			
HF-1					■	■	■	■	■	■						
AC-1						■	■	■	■	■	■	■	■	■	■	
AC-2	■	■	■	■	■											
AC-5					■	■	■	■								
DA-1						■	■	■	■	■	■	■	■			
DA-2								■	■	■	■	■	■	■	■	
DA-3								■	■	■	■	■	■	■		
DA-4								■	■	■	■	■	■	■	■	
DA-5						■	■	■	■	■	■	■	■	■		
DA-6							■	■	■	■	■	■	■			
DA-7							■	■	■	■ ?	■ ?					■ ?
GS-1					■	■	■	■	■	■						
GS-2					■											
GS-3					■	■	■	■	■	■						
GS-4			■	■	■											
GS-5					■	■	■	■	■	■	■	■				
GS-6			■	■	■											
GS-7					■	■	■									
GS-8			■	■	■											

5.2.1. Geologic Investigation Boreholes

Five Geologic Investigation (GI) boreholes were drilled to characterize the PE1 testbed. U12p.06 GI-2, GI-3, and GI-4 were drilled from the left (west) rib of the U12p.06 Bypass drift at the planned locations of the 1490, 1280, and 1190 drifts, respectively, prior to mining. U12p.06 GI-5 and GI-6 were drilled westward from the faces of the 1280 and 1190 drifts, respectively. As noted above, GI-2, GI-3, and GI-4 were later destroyed during mining of the three access drifts. (Hole U12p.06 GI-1 [not described here] was drilled in 1992 from the north end of the U12p.06 drift toward the location of the then-planned nuclear test for which the U12p.06 drifts were originally constructed.)

5.2.1.1. GI-2

Borehole U12p.06 GI-2 was the first hole drilled. Issues related to stabilizing the rig and accounting for the natural drop in the hole path due to the design of the special PQ-HQ core bit described in the Borehole Drilling and Core Collection section resulted in lower core recovery than in all subsequent holes (these issues were mitigated for later holes).

The GI-2 hole dropped in elevation significantly during drilling so that it penetrated the invert elevation of the 1490 drift about 15 ft outside the planned experiment room and thus did not sample geologic units in the room (see description of short cores collected to fill this data gap in the Additional Geologic Sample Collection section). The hole penetrated VNT-1 through VNT-4 and extended into the top of VNT-5.

At the time of geophysical logging and video runs, the GI-2 borehole had standing water from drilling operations present at 69.5 ft, with significant sandy muck from drilling present, which increased downhole. Camera and televiewer logs did not show any distinct fractures or regions of borehole breakout. Borehole scarring from the drilling process was observed in multiple locations. Caliper logs show that hole is in gauge for most of its length, with no large breakout or enlargements observed. A particularly smooth section is observed from 25 to 50 ft.

5.2.1.2. GI-3

The U12p.06 GI-3 borehole penetrated VNT-2 through VNT-4 and extended into the top of VNT-5. The GI-3 hole also dropped significantly during drilling and so was halted before it reached its planned drilled length. The GI-5 borehole was drilled later, in part to fill this data gap.

No standing water was observed in GI-3 at the start of geophysical logging; however, sandy muck was present on the bottom side of the hole and increased with depth. Two minor fractures were observed in the video between 10 and 15 ft but were not apparent in the televiewer logs. Borehole scarring is visible in the televiewer log in several places, with a noticeably scarred section at 25 to 28 ft. The borehole was in gauge for most of its length, with no large breakouts or enlargements observed. The borehole wall was particularly smooth between 26 and 47 ft.

5.2.1.3. GI-4

Adjustments in its planned starting angle resulted in the U12p.06 GI-4 remaining relatively close to its planned elevation during drilling, but it was stopped short of its planned length so that it did not penetrate below the invert elevation. The GI-6 borehole was drilled later, in part to fill this data gap. The GI-4 borehole penetrated VNT-2 through VNT-4 and extended into the top of VNT-5.

At the time of geophysical logging, standing water from drilling operations was present at the bottom of the hole, and sandy muck was present that increased downhole. Several fracture features were observed in the video and televiewer logs. Possible fractures at 15.4 ft and 64.9 ft are visible in the video but are not apparent in the televiewer logs. Open fractures were identified in both the televiewer and video at 5.5, 7.8, and 21.7 ft. Between 3 and 7 ft, significant breakout features are also visible. Caliper logs show hole enlargement from the collar to 31 ft, with a fracture-controlled breakout larger than 6 in. at 5.5 ft.

5.2.1.4. GI-5

Borehole U12p.06 GI-5 was drilled westward from the face of the 1280 drift. The hole was drilled entirely within VNT-5. No fractures or breakouts are visible in the video, televiewer log, or core.

5.2.1.5. GI-6

Borehole U12p.06 GI-6 was drilled westward from the face of the 1190 drift. The borehole penetrated subunits VNT-5 through VNT-8 and extended into the top of VNT-9.

Possible fractures are visible in the video and televiewer log at 55 to 59 ft and 74 to75 ft, which correlate with fractures noted in the core. Possible fractures were logged in the core at 73 to 82 ft and 87 to 89 ft, which were not visible in the video. No breakouts or ledges are visible in the video, televiewer, or caliper log; the hole remained in gauge for most of its length. Water was visible in the video made on 06/08/2022 at the depth of about 64 ft. Beyond the depth of about 105 ft, murky water precludes confident identification of smaller borehole features, but no fractures were noted in the core beyond that depth.

5.2.2. Hydrofracture Borehole

5.2.2.1. HF-1

Borehole U12p.06 HF-1 was drilled from a point just north of the 1490 drift into and beyond the calculated damage zone for Experiment A. The hole penetrated subunits VNT-1 through VNT-5 and extended into the top of VNT-6.

The caliper log indicates that the borehole may be slightly over-sized between 25 and 35 ft, and between 50 and 52 ft, and partially constricted at 63 to 65 ft, but these variations are not apparent in the video. Possible fractures were noted in the core at the depths of 9.7 and 24.4 ft, but these are not apparent in the borehole video.

5.2.3. Accelerometer Boreholes

Three Near-Source Accelerator (AC) boreholes were drilled following excavation of the three access drifts. AC-1 and AC-2 provide locations near Experiment A at positions above and below the plane of the test; AC-5 is located mid-way between Experiment A and Experiment D_L locations and provides sensor locations near the tunnel elevation.

5.2.3.1. AC-1

The U12p.06 AC-1 borehole penetrated VNT-2 through VNT-10 and extended into the upper part of the UZNT.

When the geophysical borehole logs were run in February 2022, water was observed at the depth of 155.7 ft. The presence of water precluded running of some logs (e.g., optical televiewer) in the lowest 10 ft of the hole. Water was added, however, to facilitate other logs. In June 2022, the water level was tagged at the depth of 103 ft.

5.2.3.2. AC-2

The U12p.06 AC-2 borehole penetrated VNT-1 through VNT-C and extended into the lower part of VNT-D.

Caliper data show a decrease of about 1 in. in the borehole diameter just below the casing, likely due to the presence of the cement used to seal the casing. An increase in borehole size (~1 in.) is apparent at 106 to 108 ft. At TD, there is a small core stub present.

Possible openings along bedding planes are visible in the video at 36.3, 38.8, and 54.6 ft. Several drilling-induced ledge features are present at the depths of 101.1, 105.9, 107.4, 113.3, 114.9, and 116.1 ft.

5.2.3.3. AC-5

The U12p.06 AC-5 borehole has a "banana" shape due to the shallow starting angle and natural downward trend that can occur during drilling. This change in shape means that the borehole begins to drop at the depth of approximately 90 ft.

A small void is visible in the video just below the collar, at 11.8 to 12 ft. A small ledge is present at 17.7 ft, and a possible fracture is visible at 62.9 ft. Significant mud and debris were present in this borehole and obscured the borehole walls in portions of the video. A possible fracture was noted in the core at 67 ft but is not visible in the video.

5.2.4. Drift Accelerometer Boreholes

Seven Drift Accelerometer (DA) holes were drilled vertically down from the invert of the U12p.06 Bypass drift to the depth of 37 ft, and all have 5 ft collar casings. They are positioned approximately every 100 to 200 ft from near the 1490 drift to just north of the 650 alcove.

5.2.4.1. DA-1

The U12p.06 DA-1 borehole penetrates units VNT-3 through VNT-8 and extends into the top of VNT-9

Water was present at the bottom the borehole (depth of 36.2 ft) on 12/13/2021. Small fractures are visible in the video and optical televiewer at 6.9 and 7.2 ft. Small ledges are present at 17.8, 18.2, and 19.7 ft. A small washout feature is present at 20.1 ft. Possible fractures were noted in the core at 1.0, 17.0, 22.6, and 23.3 ft, but are not apparent in the video.

5.2.4.2. DA-2

The U12p.06 DA-2 borehole penetrates units VNT-4 through VNT-10 and extends into the top of the UZNT.

A small ledge and a void are present at the bottom of the casing at 5 ft, as seen in the video, televiewer, and caliper logs. Additional small ledges are observed at the depths of 6.5, 12.0, 14.0, 27.0, and 34.0 ft. Small fractures are present at 8.1 and 9.5 to 10.4 ft, and a small washout feature is present at TD. Possible fractures were noted in the core at 1.4, 3.4, 4.4, 17.6, 19.3, and 23.0 ft, but are not apparent in the video or televiewer. The caliper log data shows fairly large variations in hole diameter, with a steady increase starting at 11.5 ft, reaching a maximum (1 in. larger) at 14 ft before abruptly decreasing.

5.2.4.3. DA-3

The U12p.06 DA-3 borehole penetrates units VNT-4 through VNT-9 and extends into the top of VNT-10.

A small void is apparent in the video, televiewer, and caliper logs, just below the casing at 5.9 ft. Another small washout feature and ledge are present near TD at 36.3 ft. Possible fractures are visible in the video and televiewer at the depths of 18.0, 19.0, 19.5, 20.3 to 28.8, 29.4 to 33.7, and 35.5 to

36.3 ft. Possible fractures were noted in the core at 16.7, 22.2, 24.8, and 35.4 ft, several of which appear to correlate with features observed in the video.

5.2.4.4. DA-4

The U12p.06 DA-4 borehole penetrates units VNT-4 through VNT-10 and extends into the top of the UZNT.

A small void is visible in the video and televiewer log at 5.5 ft, just below the collar. Small ledges are present at 6.5 and 8.6 ft, and small closed fractures are visible at 9.9 to 10.3, 17.9 to 21.0, and 21.3 to 23.5 ft. Fractures were also noted in the core at the depth of 20.7 ft. Possible fractures were noted in the video and televiewer at 6.5, 24.5 to 28.9, 32.5 to 34.0, and 34.5 to 36.4 ft. The caliper data shows a ~0.5 in. decrease in diameter at 8.5 ft, where a small ledge is visible.

5.2.4.5. DA-5

The U12p.06 DA-5 borehole penetrates units VNT-2 through VNT-9 and extends into the top of VNT-10.

A significant void (1.5 in.) is visible in the video, televiewer, and caliper logs just below the casing at 5.5 ft, and small breakout features were noted at the depths of 8.4, 19.7, and 36.4 ft. Small, closed fractures were noted in the video and televiewer at 9.5 and 16.8 ft. A small ledge is visible at 25.0 ft. and at TD. Possible fractures were noted in the core at 0.1, 9.5, 16.7, and 30.7 ft, but are not visible in the video.

5.2.4.6. DA-6

The U12p.06 DA-6 borehole penetrates units VNT-3 through VNT-8 and extends into the top of VNT-9.

Water was present at the bottom of the hole on 12/15/2021. A void is visible in the video and televiewer log, just below the casing at 5.0 ft. Significant fractures can be seen in the video and televiewer at the depths of 11.8 to 12.5, 30.3 to 36.1, and 36.7 to 36.9 ft. The fracture at 30 ft becomes tighter below 32.2 ft. Small ledges are present at 15.5 and 17.9 ft.

The presence of the VNT-7 unit is not clear in the core. The unit may be present but thin (<0.2 ft), however the exact nature of the contact between VNT-6 and VNT-7 is uncertain.

5.2.4.7. DA-7

The U12p.06 DA-7 borehole penetrates subunits VNT-3 through VNT-5. Units below VNT-5 cannot be confidently identified and may have been removed by a scour-like feature observed in other areas of P-Tunnel, which is characterized by the presence of a variety of reworked tuff layers deposited at varying dip angles.

A void was noted in the video, televiewer, and caliper logs just below the casing at 5 ft. A small fracture can be seen in the video and televiewer at 8.2 to 8.4 ft, and a possible fracture was noted at 31.4 ft. A small washout feature is present at 11.7 ft, and a ledge is present at 14 ft. Fracture-like features were noted in the core in the interval 24.8 to 27.1 ft, at 32.5 ft, and 36.3 ft, but it is likely that these features are associated with the postulated scour structure, and not true fractures.

The caliper measurements indicate that the hole diameter steadily increases between 10.0 and 13.8 ft, and decreases sharply back to the nominal diameter of 4.8 in. at 13.8 ft.

5.2.5. Gas Sampling Boreholes

Eight Gas Sampling (GS) boreholes were drilled at various angles, depths, and distances from Experiments A and D_L to serve as locations for insertion of instrumentation for collecting gases from the tuff.

5.2.5.1. GS-1

The U12p.06 GS-1 borehole penetrates VNT-1 through VNT-5 and extends into the top of VNT-6.

A void and small ledge are visible in the video and televiewer log just below the casing at 5 ft. A small opening along bedding can be seen observed in the video and televiewer log at 17 ft. Several ledges are visible in the video at 13, 30, 41, 48.4, and 48.8 ft. Possible fractures were noted in the core at 25.7, 49.8, and 51.2 ft but are not visible in the video. A small amount of water was observed at 56 ft in the borehole on 02/14/2022.

The caliper measurements show changes In borehole diameter in several sections. The diameter is roughly 1 in. larger than the nominal 4.8 in. from the bottom of the casing to the depth of 8 ft. The diameter increases again (by 1.3 in.) at 13 ft. and then decreases sharply at 15 ft. Small increases of 0.5 in. are observed at 18 to 20.5 ft. and at 42 to 44 ft. A larger (1.5 in.) increase in diameter was measured at 30 to 32 ft. (it increases slowly starting at 21 ft).

5.2.5.2. GS-2

The U12p.06 GS-2 borehole remained within VNT-1 for its entire length.

A fracture can be seen in the video, televiewer log, and the core at 12.4 ft, and an open bedding plane is visible at 47.2 ft. A possible fracture is observed in the core at 19.9 ft but is not visible in the video. Several small ledges are present in the last ten feet of the hole, at the depths of 48.6, 54.0, and 56.6 ft. The caliper measurements indicate that the hole diameter steadily narrows with depth, however it is unclear if this change may be an artifact of using a one-arm caliper tool.

5.2.5.3. GS-3

The U12p.06 GS-3 borehole penetrates VNT-1 through VNT-5 and extends into the top of VNT-6.

A void is visible in the video and televiewer log just below the casing at 5 ft. A fracture can be seen in the video and televiewer log at 11.2 ft, and another possible fracture was noted at 32 ft. Small ledges are present at 25.5, 52.9, 57.5, 59.0, and 59.5 ft. Possible fractures were noted in the core at 3.4, 15.0, 15.8, 21 to 22, and 49.5 ft. but are not visible in the video. Water was tagged at the depth of 60.5 ft in the borehole on 02/15/2022.

5.2.5.4. GS-4

The U12p.06 GS-4 borehole penetrates VNT-1 and extends upward through VNT-A and into the bottom of VNT-B.

A void is visible in the video, televiewer, and caliper log just below the casing at 10 ft. This hole skimmed a rock bolt, which can be seen on the top of the borehole at 11 to 12 ft in the video, and that likely caused this void, as rock broke away from the bolt into the hole. A small ledge is visible at 60.7 ft. A possible fracture was noted in the core at 43.7 ft, but is not visible in the video.

5.2.5.5. GS-5

The U12p.06 GS-5 borehole penetrates VNT-1 through VNT-7 and extends into the top of VNT8.

A void can be seen just below the casing at 5 ft in the video and televiewer log. A fracture can be seen in the video and televiewer at 6.5 ft, and additional possible fractures were noted at the depths of 12 and 13 ft. A small ledge is present at 5.9 to 6.0 ft, just below the casing. A potential fracture was noted in the core at 40 ft but is not visible in the video. Water was tagged at the depth of 54.2 ft on 02/15/2022.

5.2.5.6. GS-6

The U12p.06 GS-6 borehole was collared near the top of VNT-1, penetrates through VNT-A, and extends into the bottom of VNT-B.

A small ledge and a void can be seen just below the casing, at 10.5 ft in the video, televiewer, and caliper log. Small adjustments made in the rig position after the casing was installed resulted in a small shift in the planned borehole path, and minor drilling issues, which likely contributed to development of these features. A breakout feature along the bedding can be seen in the video and televiewer at the depths of 43.8 and 48.1 ft, and small ledges are present 54.5 and 62.8 ft. Openings along bedding are visible at 58.0 and 59.4 ft. Possible fractures were noted in the core at 18.5, 34.0, and 41.5 ft, with additional breaks along bedding at 55.9, 61.2, 61.6, and 62.1 ft, but none of these features are apparent in the video.

The caliper data indicates that the borehole diameter varies significantly (~0.6 in.) in the intervals of 15 to 30 ft and 41 to 55 ft (3 in. at max). Apparent borehole diameters as observable in the video do not match these drastic variations in the caliper data and may be an artifact of limitations in the one-arm caliper used. It is possible that the hole may have an oval shape.

5.2.5.7. GS-7

The U12p.06 GS-7 borehole was collared in VNT-2, but due to the dip of the VNT units, it enters VNT-1 for a short distance, then again enters and penetrates through VNT-2 and into VNT-3.

A void is visible in the video and televiewer just below the casing at 5 ft. A possible fracture was noted in the core at 10.2 ft. but is not visible in the video. A significant deviation in the caliper data (1.5 in.) is observed at 7.0 to 7.5 ft.

5.2.5.8. GS-8

The U12p.06 GS-8 borehole was collared near the top of VNT-1, penetrates through VNT-A, and extends into the bottom of VNT-B.

A void is visible in the video and televiewer log just below the casing at 10.1 ft. Small ledges are present at the depths of 46.9, 48.0, 52.4, and 52.9 ft. Breaks along bedding were noted in the core at 3.3, 35.6, and 47.3 ft, and a possible fracture was noted at 49.6 ft; however, none of these are visible in the video.

5.3. Borehole Measurements

Local permeability and hydrofracture measurements were conducted in a subset of the boreholes using dual packer systems designed and fabricated at Sandia National Laboratories (SNL). These measurements were taken after the initial borehole logging by NNSS and Colog, which helped to inform and define the testing intervals. Following hydrofracturing, optical televiewer logs were re-run to look for induced fractures.

5.3.1. Local Permeability

Local permeability measurements were conducted over two campaigns in GI-2, GI-3, and GI-4 (March 2021), and GI-5, GI-6, HF-1 and AC-1 (June 2022), using a dual-packer, air-based, in-situ permeameter (Figure 16). The system utilizes two borehole packers, inflated with compressed air, to isolate an interval (first campaign, 2.8 ft.; second campaign, 1.4 ft.). Packers are inflated to a pressure of 100 to 120 psi to ensure a tight seal within the borehole. Compressed air is then allowed to flow into the interval, while the flow rate and interval pressures are recorded. Compressed air is supplied to the interval and the packers by two gas cylinders, one for each component.

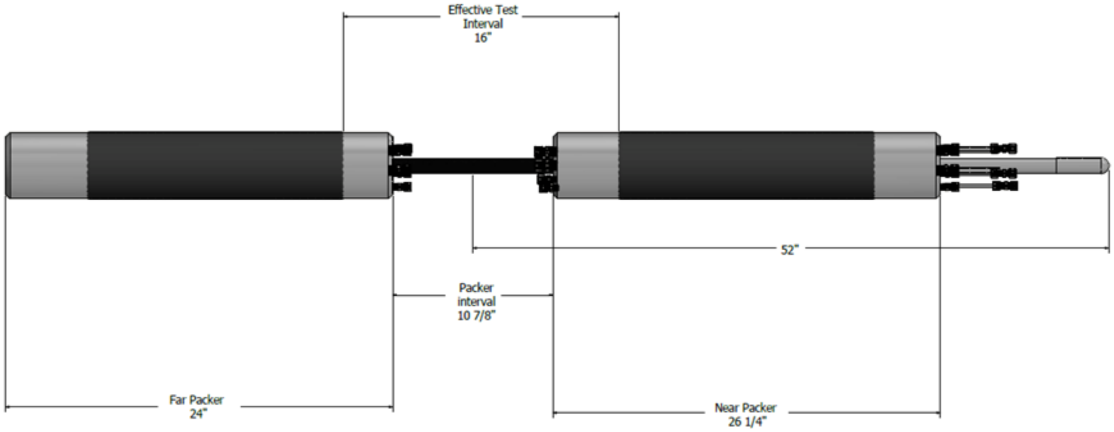

Figure 16. Schematic of the air permeability dual packer assembly. Interval dimensions reflect equipment used in the second campaign.

Prior to transporting the local permeability system (this includes the packers, tanks, Data Acquisition (DAQ), and tubing connections) underground, the system was leak-tested using a section of spare drill casing with a diameter comparable to that of the boreholes. This impermeable casing allowed for any leaks in the system's plumbing to be identified and remediated to ensure that pressure builds in the interval and there was no air loss within the system. Additional leak testing was performed underground using spare casing before the start of the measurement campaign and in between measurements if the data return was questionable or something had changed in the system configuration (such as breaking connections).

Local permeability measurements were taken at the locations detailed in Figure 17. The deepest location in each borehole was measured first. For Campaign 1, measurements were performed using a 1 L/min and a 2 L/min flow rate (the maximum at the time) in an alternating fashion. This approach was taken because it was not possible to build pressure in the interval to the desired value of 30 psi. Instead, data were taken at both flow rates until the pressure in the interval stabilized, at which point the pressure was shut in and the pressure decay was observed. Results were compared to water permeability estimates using the Hydrofracture system data and were found to be in general agreement.

For Campaign 2, the system was upgraded to include a 20 L/min flow controller and a pressure gauge at the test interval. Each location was tested at three interval pressures (10, 20, and 30 psi) that were set using the supply tank. The pressure was allowed to stabilize, the flow rate was recorded, and the pressure was shut in. Note that the pressure measured at the interval does not always equal the pressure set at the tank. Further details can be found in Stauffer et al. (2022) [19].

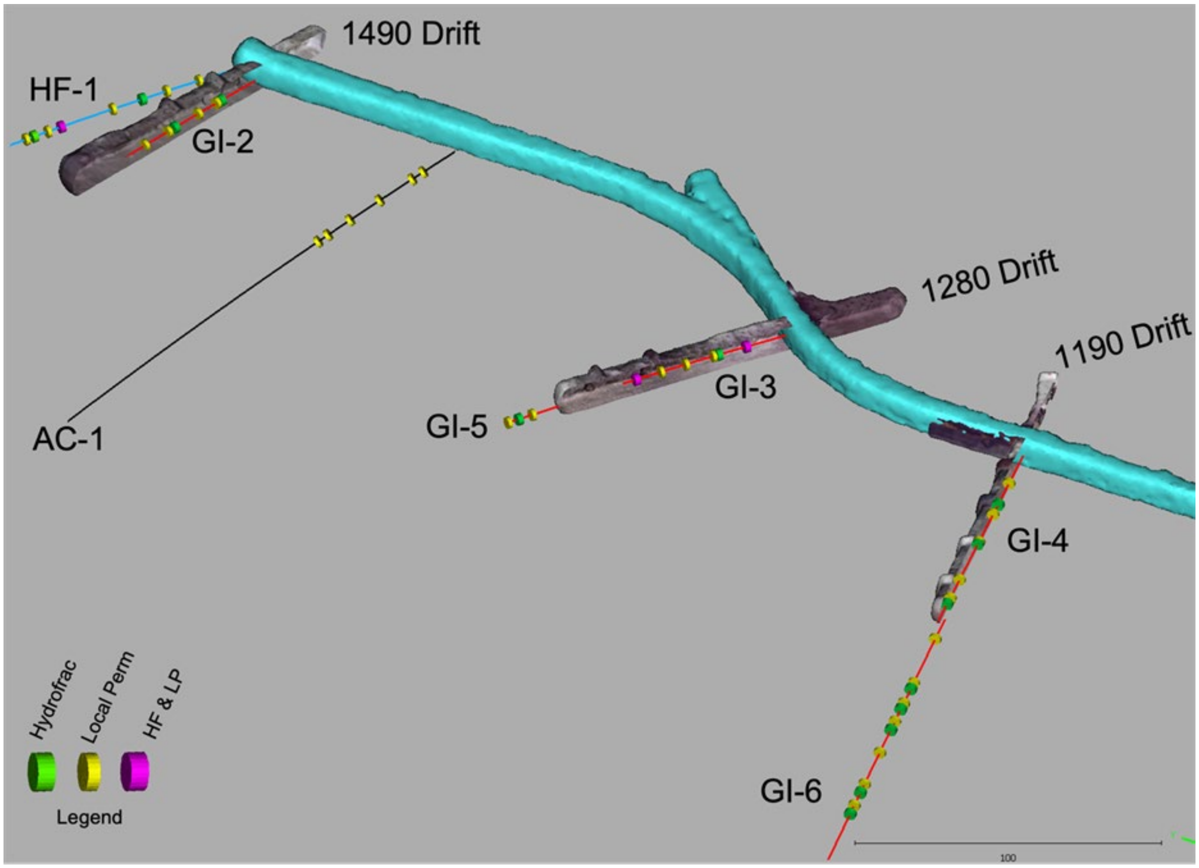

Figure 17. Locations of hydrofracture and local permeability measurements. Yellow symbols represent Local Permeability measurements, green symbols represent Hydrofracture measurements, and purple symbols represent location where both were taken. Cylinder length shows testing interval. Diameters sized for display only and don't reflect radial sampling extent.Left rib of test drifts removed for clarity.

Preliminary permeability estimates at each location were calculated at Los Alamos National Laboratory (LANL) using the FEHM (Finite Element Heat and Mass) multiphase flow and transport simulation code (fehm.lanl.gov). The simulations were built as radial 2-D with a borehole in the center and used the interval geometry, pressure, and flow rates to estimate permeability in a homogeneous formation surrounding the dual packer assembly. The analysis assumes that a single Van Genuchten (VG) function applies to the rock to obtain the estimates (Figure 18 & Figure 19). Permeability is generally lower in the deeper VNT units. The deepest geologic units (VNT-9 and VNT-10) have permeability values on order of 1e-16 m^2 or less. Several of the measurements in the upper units (VNT-1 to VNT-5) are up to three orders of magnitude higher, approaching 1e-13 m^2 in HF-1, VNT-1. However, there seems to be significant variability even within VNT units, possibly reflecting the visually observed lithologic variability, even as measurements at individual locations are quite consistent. For additional details see Stauffer et al (2022) [19].

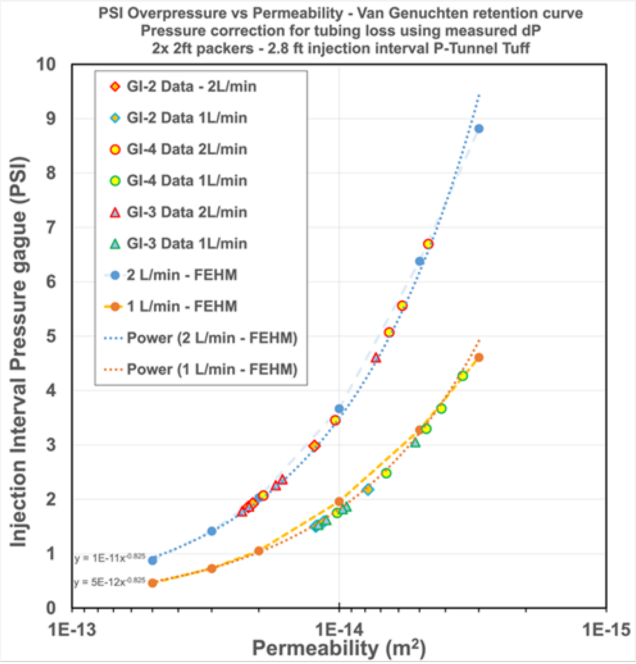

Figure 18. Permeability estimates from the first campaign. Data for each measured pair of interval pressure and flow rate is plotted with larger color symbols. Blue and orange lines denote the calculated permeability curves for 1 and 2 L/min from FEHM given the packer geometry, a pressure correction (dP) for tubing loss, and an assumed Van Genuchten retention curve. These curves were used to back out permeability from the measured pressures.

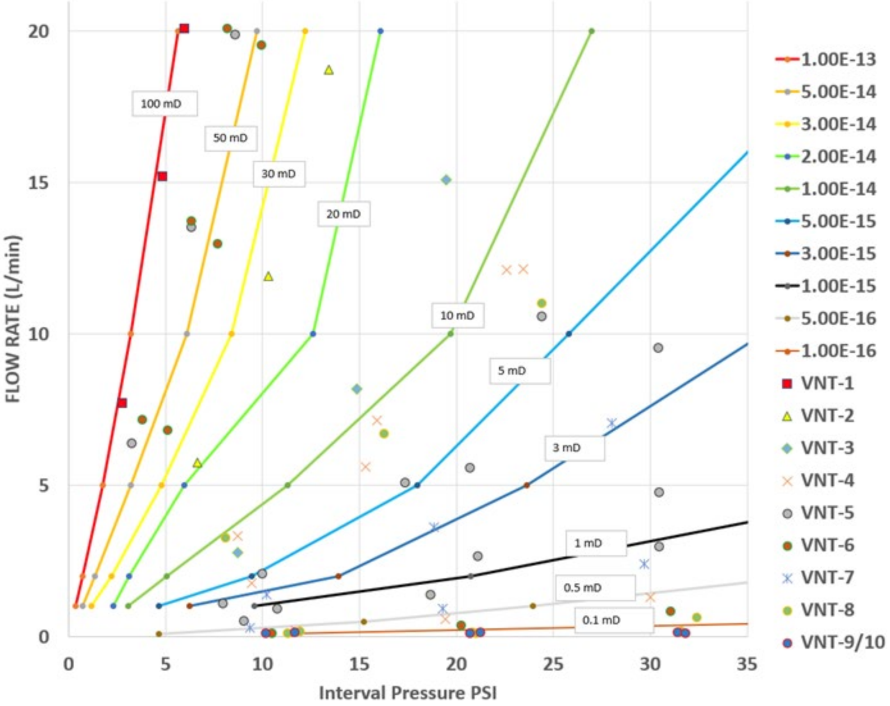

Figure 19. Permeability estimates for the second campaign. Measurements within each VNT unit are plotted as colored symbols (as a function of interval pressure and flow rate). Colored lines represent the calculated permeability curves (in millidarcies) from FEHM given packer geometry and an assumed Van Genuchten retention curve. No pressure correction was needed for tubing in

this campaign as the pressure transducer was located in the injection interval. For more details see Stauffer et al. (2022) [19].

5.3.2. Hydrofracture Measurements

Hydrofracture measurements were conducted over two campaigns in GI-2, GI-3, and GI-4 (March 2021), and GI-5, GI-6, and HF-1 (July 2022). Measurements were made after local permeability and initial borehole logging was completed so as not to alter the borehole conditions or local rock properties. Hydrofracture measurements were made using a dual-packer system and facility water and air. Borehole packers were inflated with water, using an independent air-driven pump, to a starting pressure of ~1000 psi. Water was then pumped into the 1.9 ft testing interval using a second air-driven pump. Pressure was allowed to build in the testing interval (and consequently in the bounding packers) until a pressure drop consistent with fracturing was observed (Figure 20; ex. 510 sec). The fracture was held open for ~1 to 2 min, and the flow rate was monitored for total injected volume (ex. 675 sec). The pressure was then shut in and the decay was recorded. Once stabilized, the fracture was then reopened (ex. at 1200 sec, 1360 sec), and pressure was shut in for a second time. The reopening cycle is important for calculating the reopening pressure, which will be lower than the formation-breaking pressure needed to initiate fracture.

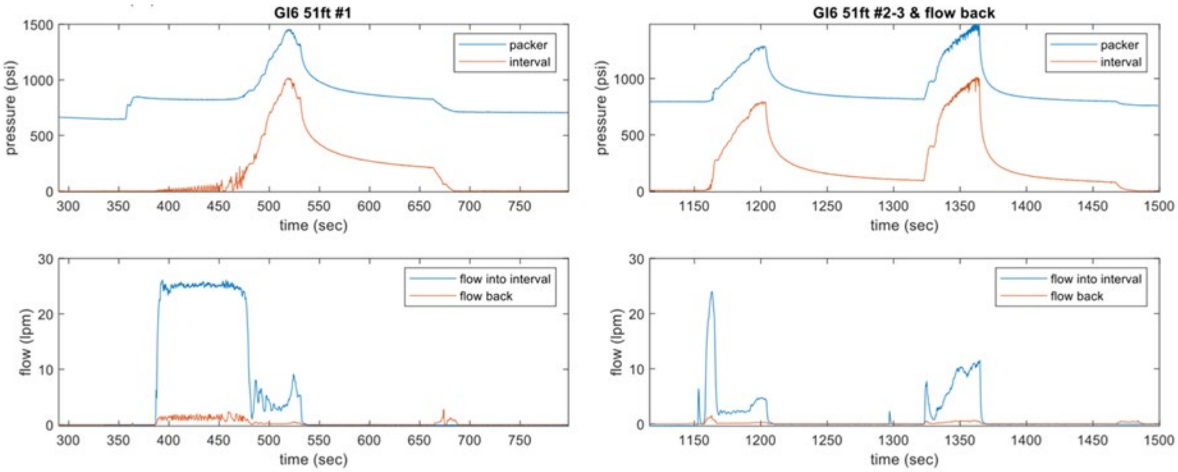

Figure 20. Plots showing a typical hydrofracture run. (Left) The initial fracturing of the interval, here in GI-6. (Right) Two reopening sequences following the initial hydrofracture at the same interval. Upper panels show the pressure in both the packers (blue) and the interval (orange). Bottom panels show the flow rate into the interval (blue) and the flowback (orange).

Water pumped into the testing interval was dyed using a combination of nontoxic fluorescent dyes from Bright Dyes (blue) and Kingscote (red) to stain the rock and help identify fractures while mining through later. GI-2 was dyed red, GI-4 was dyed blue, and GI-3 was dyed purple (a combination of the red and blue dyes). During the mining of the 1190, 1280, and 1490 drifts, however, evidence of the dye used in these boreholes was not observed. We conducted a series of tests at SNL looking at different dyes and concentrations using tuff hand samples from the tunnel. It was concluded that the dye concentration used in the first campaign was too low to stain the rock and the concentration was significantly increased for the second campaign. Bright Dyes (blue) were used for GI-5, GI-6, and HF-1 hydrofracture measurements. At the time of writing, the B and D_L chambers have not been mined, which allows for investigation of dye in the rock (GI-6 and GI-5 respectively) when they are excavated. HF-1 will not be mined through and cannot be evaluated in this way.

After the first campaign, it was determined that the system was not able to supply the flow rates and fluid viscosities that may be necessary to obtain definitive fractures in the permeable rock. For Campaign 2, the interval pump was upgraded to a higher flow system and bentonite was used as a thickening agent.

Hydrofracture measurements were made at the location shown in Figure 17. Whenever possible, hydrofracture locations were chosen to correspond with local permeability locations. In many locations, because the rock is highly permeable, the system was unable to build pressure in the interval in a way that resulted in a clear hydrofracture (a pressure drop signaling crack opening). In these cases, we still collected data, paying particular attention to shut in pressures, as this information is also beneficial to researchers looking at water permeability of the geology. Water permeability is complicated by the addition of bentonite; however, no additives were used in Campaign 1, allowing for more straightforward estimation. Locations where a potential hydrofracture was observed in the pressure data are indicated in Table 10.

Table 10. Locations of the hydrofracture measurements. Measurements highlighted in red are locations where a potential hydrofracture was observed in the pressure data.

Borehole	Depth (ft) and Unit				
GI-2	17 VNT-2	38 VNT-3			
GI-3	15 VNT-3	27 VNT-3	46 VNT-4	**55 VNT-4**	
GI-4	30 VNT-3	**44 VNT-4**	**72 VNT-5**		
GI-5	**17 VNT-5**				
GI-6	32 VNT-6	42 VNT-6	52 VNT-6	**82 VNT-8**	**91 VNT-8**
HF-1	**40 VNT-3**	**66 VNT-4**	**78 VNT-5**		

Optical televiewer borehole logs were run following the completion of hydrofracture measurements. For GI-2, -3, and -4, this logging was done using SNL's Mount Sopris OBI40 Optical televiewer by the same team that performed the hydrofracture measurements. For GI-5, GI-6, and HF-1, logging was done by Colog using the same optical televiewer setup that was run prior to hydrofracture measurements being made. In GI-2, -3, and -4, there was no obvious evidence of fracture in the televiewer logs.

Figure 21. Photograph of the Hydrofracture system being run in GI-3.

This page left blank

6. ADDITIONAL GEOLOGIC SAMPLE COLLECTION

In addition to the borehole cores described above, small geologic samples were collected from the drift walls, and short core samples were taken from the Experiment A chamber to enhance site characterization.

6.1. Drift Grab Samples

Drift grab samples were collected from the 1190, 1280, and 1490 drift rib walls shortly after mining was completed in each drift. These samples are roughly 6 in. in diameter and were chipped directly from the rib walls. Samples were collected at ~nominally 20 ft intervals along the drifts and sampled all the accessible lithologies at each location. In total, 31 samples were collected from unique locations, spanning VNT units 1 through 6 (Table 11).

Three samples were taken at each location: a primary sample, a duplicate sample, and a preserved sample. Preserved samples were wrapped in plastic, vacuum-sealed, and then canned to ensure that the state of hydration was kept constant (Figure 22). Samples were taken from the rib walls as soon after excavation as possible to prevent the rocks from drying out too much. The 1190 drift samples were collected 14 to 27 days after excavation; the 1280 samples 7 to 27 days; and the 1490 samples 7 to 29 days. These preserved samples were collected specifically to be used for water content analysis at SNL [22], the results of which support the broader geomechanics testing [7].

Table 11. Locations of geologic grab sample collections. All coordinates are in NAD 27 Nevada State plane.

Drift	Northing	Easting	Elevation (ft)	Unit
1490	906113.3	648012.3	5523.9	VNT-1
1490	906113.5	648012.0	5522.0	Lower VNT-1
1490	906113.1	648013.2	5519.6	Upper VNT-3
1490	906123.8	647993.0	5523.6	Lower VNT-1
1490	906123.9	647992.7	5521.4	VNT-3
1490	906123.9	647992.8	5519.7	Lower VNT-3
1490	906133.6	647972.0	5520.0	VNT-4
1490	906133.3	647971.8	5521.9	VNT-3
1490	906133.1	647972.3	5523.7	VNT-3
1280	905921.2	647973.7	5523.7	Lower VNT-1
1280	905920.6	647974.5	5522.3	Lower VNT-2
1280	905921.2	647973.6	5520.7	VNT-3
1280	905935.9	647957.8	5524.0	Lower VNT-1
1280	905935.5	647958.0	5521.8	VNT-3
1280	905935.6	647958.1	5520.8	VNT-3
1280	905950.3	647942.4	5524.3	VNT-3
1280	905950.3	647942.4	5521.2	VNT-4
1280	905950.3	647942.6	5520.0	VNT-4

Drift	Northing	Easting	Elevation (ft)	Unit
1280	905962.0	647929.4	5523.5	VNT-4
1280	905962.2	647929.2	5522.4	VNT-4
1280	905962.3	647928.8	5521.1	VNT-5
1190	905814.5	647966.7	5522.9	VNT-1
1190	905814.6	647948.2	5520.6	VNT-3
1190	905814.8	647948.0	5522.6	VNT-3
1190	905814.7	647926.5	5520.1	Upper VNT-4
1190	905814.8	647926.6	5522.6	VNT-3
1190	905814.6	647905.4	5519.4	Upper VNT-5
1190	905814.5	647905.5	5520.8	VNT-4
1190	905814.6	647905.5	5523.0	Lower VNT-3,Upper VNT-4
1190	905814.7	647891.5	5518.2	Base VNT-5
1190	905814.7	647893.0	5518.0	VNT-6

Figure 22. Photograph of two geologic grab samples from the 1490 drift. Leftmost sample is preserved, and rightmost sample is bagged.

6.2. Chamber Short Core

Short cores were collected from the Experiment A chamber at the face of the 1490 drift (Figure 23). These short cores enable us to extract geologic samples in the chamber region, from lithologies that were not sampled by the GI-2 borehole. These samples span VNT units 3 through 5.

Samples were taken from the face (four locations), south rib (six locations), and north rib (three locations), and sampled all available VNT units (Table 12). Short cores were collected using a handheld drill with a specialized coring bit. The resulting samples are ~12-in. in length and 2.5 in. in diameter. Samples were stored in plastic bags.

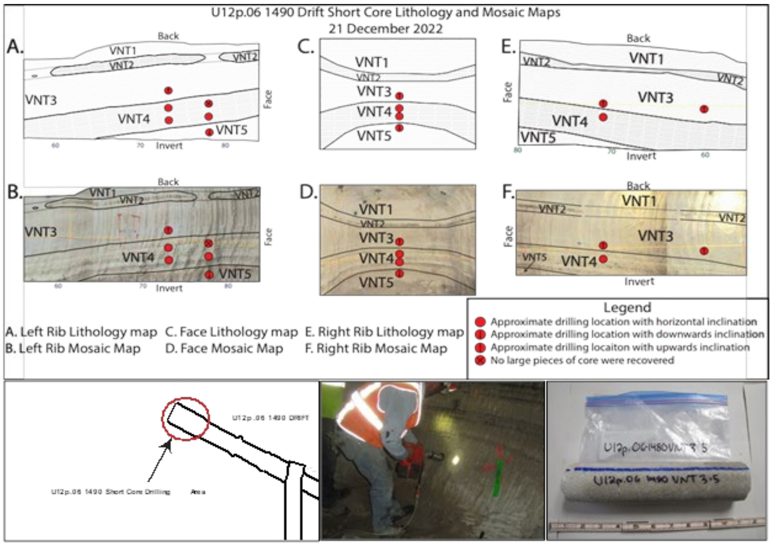

Figure 23. Short core locations. A-F shows the collection locations plotted on the mapped VNT layers. The A Chamber location is shown in the bottom left. Bottom right shows a photograph of the collection and an example sample from VNT-3.

Table 12. XYZ locations of the Short Core collection points. All Coordinates are in NAD 27 Nevada state plane.

Sample ID	Easting	Northing	Elevation (ft)	Location	Unit
U12p.06-1490-VNT3-1	647959.27	906147.74	5523.47	Face	VNT-3
U12p.06-1490-VNT3-3	647969.93	906134.65	5521.68	South Rib	VNT-3
U12p.06-1490-VNT3-4	647972.87	906149.21	5521.64	North Rib	VNT-3
U12p.06-1490-VNT3-5	647982.67	906143.98	5520.86	North Rib	VNT-3
U12p.06-1490-VNT4-1	647959.31	906147.66	5522.47	Face	VNT-4
U12p.06-1490-VNT4-2	647959.46	906147.55	5521.14	Face	VNT-4
U12p.06-1490-VNT4-3	647962.93	906138.30	5521.40	South Rib	VNT-4
U12p.06-1490-VNT4-4	647962.97	906138.28	5519.97	South Rib	VNT-4
U12p.06-1490-VNT4-5	647970.10	906134.69	5520.43	South Rib	VNT-4
U12p.06-1490-VNT4-6	647970.33	906134.75	5518.89	South Rib	VNT-4
U12p.06-1490-VNT4-7	647972.93	906149.29	5520.92	North Rib	VNT-4
U12p.06-1490-VNT5-1	647959.84	906147.25	5519.64	Face	VNT-5
U12p.06-1490-VNT5-2	647963.03	906138.25	5518.25	South Rib	VNT-5

This page left blank

7. GEOLOGIC SAMPLE CHARACTERIZATION

Samples collected from the PE1 testbed were analyzed via several different methods to characterize geophysical properties, geologic composition, and hydrologic properties. Several tabletop measurements were performed on the core at the USGS Core Library using portable instruments. Additional testing was done in a laboratory setting at SNL. This laboratory work was broadly organized into three categories:

1. Geomechanical testing (e.g., elastic properties, triaxial deformation)
2. Geologic characterization (e.g., thin sections, x-ray diffraction)
3. Hydrologic characterization (e.g., water content, porosity, thermogravimetric analysis).

7.1. Tabletop Core Measurements

Geologic cores from the PE1 boreholes are archived at the USGS Core Library in Mercury, NV, for storage and management. Several tabletop measurements were performed on a subset of core at the Core Library, including ultrasonic velocity, permeability, and hardness. Observations of lithologic texture, mineralogy, and fracture occurrence were also recorded. These tests were done on the all the GI cores as well as HF-1 and AC-1 cores. Test locations were selected at intervals averaging 2 to 5 ft, with deviations in spacing caused by the condition of the core in some locations. AC-1 is an exception. Due to its length, measurement spacing was increased within the UZNT section. The UZNT is understood to be more homogenous than the VNT, thus less data was needed to capture variability. The same locations were used for all three measurements to allow for better comparison.

In general, the measurements show good agreement, with increases in velocity correlating with increases in hardness and decreases in permeability. This correlation is most prominent in the upper units (VNT-1 through VNT-5) and can be seen nicely in the GI-5 logs. This consistency offers confidence in the relative accuracy of the measurements as these use three completely independent tools.

7.1.1. Velocity

Ultrasonic velocity data was collected using a Proceq Pundit 200 ultrasound pulse velocity system (Figure 24). This system can send, receive, and record waveforms using 250 kHz transducers to determine P and S velocities. At each location, two pieces of cellophane packaging tape were diametrically applied to the core. Small amounts of acoustic couplant were applied to the transducer faces in a thin layer. The transducers were held against the pieces of cellophane packaging tape, and the Pundit system automatically recorded a waveform when the signal stabilized. This procedure was repeated for each measurement, and acoustic couplant was reapplied about three times per core transect. At each location, the diameter of the core was measured using calipers to convert the travel times to velocities.

S-wave travel times were difficult to determine on core samples. The short travel distance across the diameter of the core is not sufficient to allow full separation of P and S wave phases, resulting in overlapping arrivals. Additionally, it was not possible to measure S waves in the manufacturer recommended method. Proceq recommends applying the shear wave transducers directly to the core with a sufficient coating of couplant to ensure proper contact. It was decided to use cellophane packaging tape in between the transducers and the core to prevent widespread contamination of the core from sticky, sugary gels used as couplants. It was not possible to pick the first arrival of the S wave in the recorded data, so velocities are calculated using the first identifiable peak of the S wave phase. P waves were also picked using the first peak for consistency when comparing data, even though first arrival is more accurate.

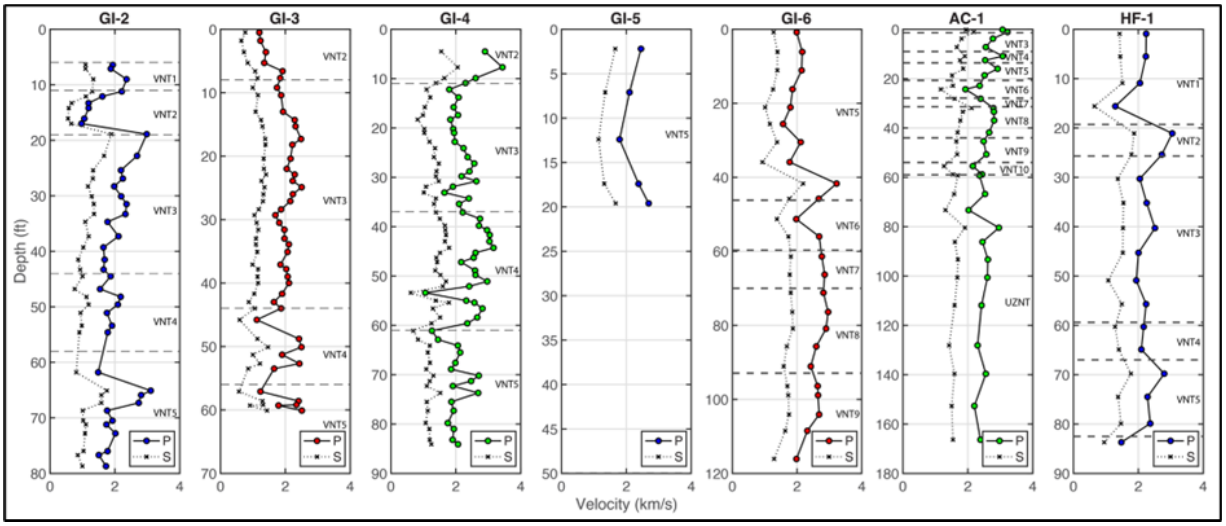

Figure 24. Ultrasonic velocity measurements performed on the GI, HF-1, and AC-1 core. Large colored symbols indicate P wave velocities while smaller x symbols (and dashed lines) indicate S wave velocities. VNT interfaces are indicated as horizontal dashed lines.

P-wave velocities average about 2 km/s and show variability across VNT units and within each unit. Note that the bedding angle varies with each core run and is not accounted for in the measurement placement. VNT-2 shows lower velocities (~1 km/s) in GI-2 and GI-3 but shows elevated velocities in GI-4. VNT-3 appears to be relatively consistent across boreholes while greater variability is observed for VNT-4 and VNT-5. Deeper units (below VNT-6) appear to have slightly higher P-wave velocities (closer to 3 km/s). Measurements from AC-1 appear to be generally a bit faster relative to the other holes, which may be related to the fact that this borehole is the only significantly dipping borehole in the set.

7.1.2. Permeability

Permeability measurements were conducted using a New England Research (NER) TinyPerm II portable permeameter (Figure 25). This system works by pressing a rubber nozzle to the sample and drawing air using a syringe. As air is pulled from the sample, a microcontroller unit simultaneously monitors the syringe volume and the transient vacuum pulse created at the sample surface, and the resulting response function is computed. Care was taken to place the TinyPerm nozzle so that it had a good seal to the core sample, which can be difficult for the small cylindrical core samples, with varying grain and pore sizes. Measurements were repeated three times and the maximum output value (T) was used to calculate absolute permeability (K) according to the NER's calibration curve equation: $K = 10((T - 12.8737)/-0.8206)$.

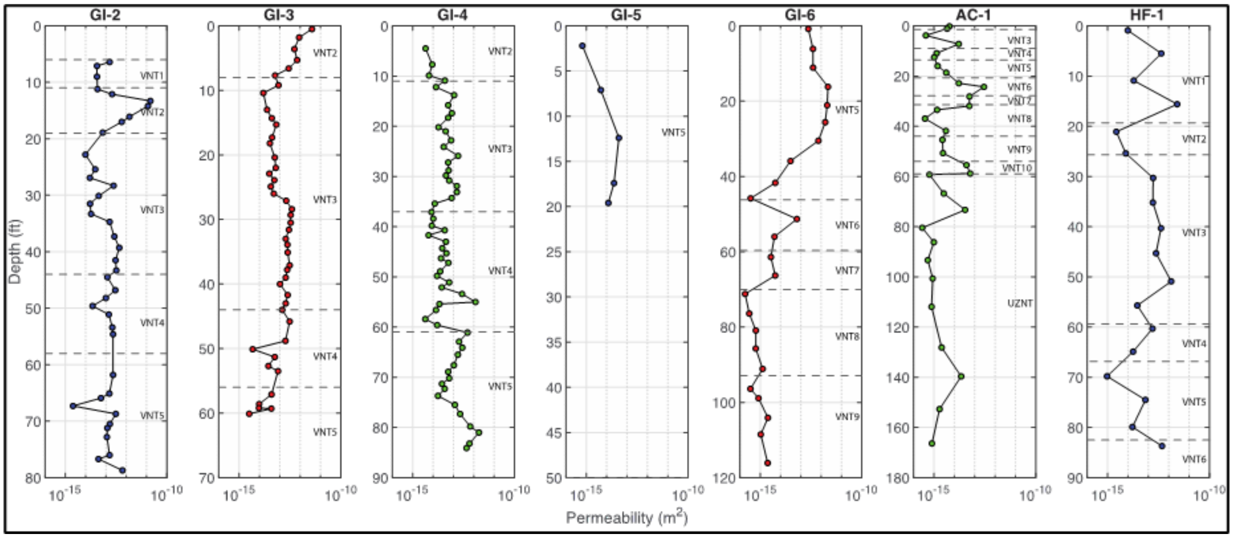

Figure 25. Permeability measurements made on the GI, HF-1, and AC-1 core made using the TinyPerm system. VNT interfaces are indicated as horizontal dashed lines.

Permeabilities tend to fall in the 10^{-14} – 10^{-12} m^2 range for the upper units (VNT-1 through VNT-5) and decreases to the 10^{-16} – 10^{-14} m^2 range for the lower units (below VNT-6), which is comparable to local permeability and laboratory measurements for the given VNT units. Permeability is lower for VNT-2 in the GI-4 and HF-1 boreholes but is slightly elevated, with wider variability (two orders of magnitude) in the GI-2 and GI-3 boreholes. Permeability values hover around 10^{-13} m^2 for VNT-3 and VNT-4, with larger variability observed in VNT-5. Core from AC-1 is in general less permeable than the other boreholes.

7.1.3. *Hardness*

Hardness measurements were made using a Proceq Piccolo 2 portable Leeb hardness tester (Figure 26). The Piccolo 2 tester was calibrated using a calibrated steel billet provided by Proceq. Measurements are reported in the HLD (Leeb D) scale and are corrected for gravity and tilt. All measurements were taken vertically perpendicular to the core axis, but measuring by hand may have introduced tilt. Five measurements were taken to get a representative average at each location.

Hardness values are typically in the 250–500 range, with some locations showing spikes in hardness, perhaps due to very local features. VNT-2 displays lower hardness in GI-2 and GI-3 but larger values in GI-4. VNT-3 is relatively consistent across boreholes (except perhaps AC-1), with values near 400. VNT-5 shows some evidence for lower hardness, particularly in GI-4. In general, hardness remains constant around 400 in the lower units (below VNT-6).

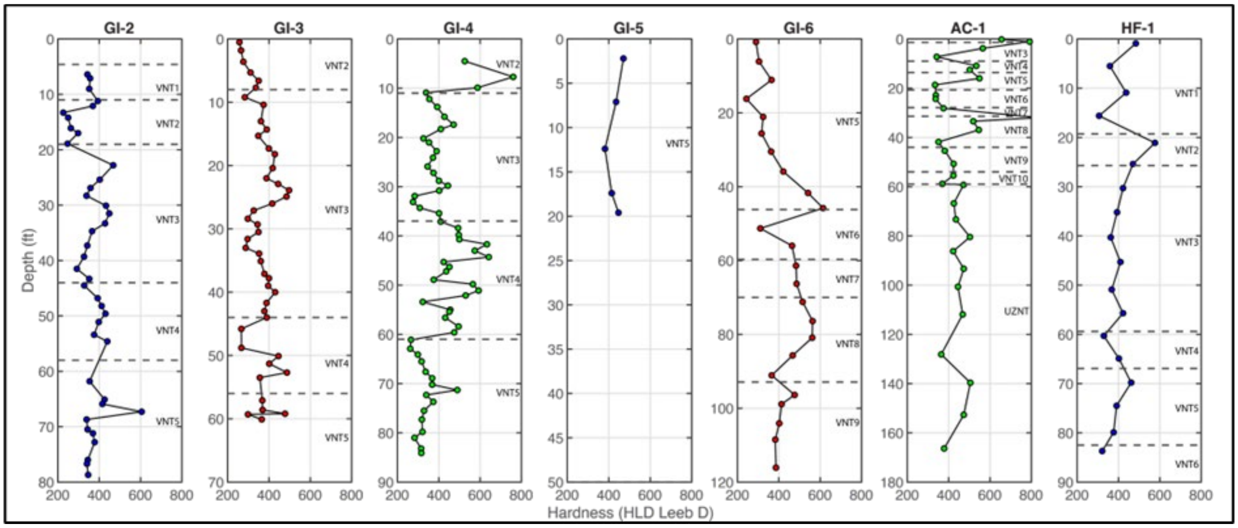

Figure 26. Hardness measurements made on the GI, HF-1, and AC-1 core made using the Piccolo system. VNT interfaces are indicated as horizontal dashed lines.

7.1.4. Fracture Analysis

Fracture occurrence was logged in core from GI-2, GI-3, GI-4, GI-5, GI-6, AC-1, and HF-1. All fractures were examined and classified as natural or induced during drilling (e.g., Lorenz and Cooper, 2018) [11]. Natural fractures were examined for surface roughness and shape, infill and surface features, sense of displacement, aperture, and orientation with respect to core features. A summary of relevant features for each fracture is given in Table 13. Orientations were recorded as α and β, where α represents the dip magnitude relative to the core axis (0 to 90°) and β represents the difference in strike orientation between the fracture and an oriented planar feature in nearby core. Obtaining a β orientation requires the fracture to be spatially tied to an oriented feature (bedding in these cores) by re-orienting core segments together and measuring the angles between an arbitrary reference line and both the fracture and the feature. This information, along with the orientation of either the core or the bedding feature, allows calculation of strike and dip of the fracture (e.g., Marjoribanks 2010) [13]. Breaks in continuity among core segments due to drilling were common, so β was not determined for most fractures.

Fractures are commonly <1 mm aperture, with a few thicker fractures associated with silica infill, preferential weathering in weaker vitric tuff, or layered zones containing varying amounts of ash, clay, and silica. Striations occur on over half of the observed natural fracture surfaces, indicating shear displacement is common. Slip on these fractures ranges from dip- to strike-parallel, suggesting that there is no preferential slip direction among the fractures. Ability to connect bedding features to a few fractures in AC-1 and GI-4 show that there is some alignment of fractures with bedding, but this alignment is not consistent and was not determined for fractures in GI-3, GI-6, and HF-1.

Table 13. Natural fractures observed during tabletop measurements of AC-1, GI-3, GI-4, GI-6, and HF-1. Induced fractures from these cores as well as those from GI-2 and GI-5 are not included in this summary. Drilling depth, infill and surface features, sense of displacement, aperture, and orientation with respect to core features (core axis, bedding) are given for each fracture. ND = not determined. DD = dip direction.

Core hole	Drilling Depth (ft)	Unit	Fracture Characteristics				
			Infill or Surface features	Shear or Extensional	Aperture	α (Dip in degrees wrt Core Axis)	β (Strike wrt Bedding Surface)
AC-1	12.1	VNT-4	None; weathered zone	ND	~3 cm	~90	206 (Bedding β=052)
	23.4	VNT-6	Thin, brown patchy material	Extensional	0.5 mm	43	ND
	52.6	VNT-9	None	Extensional	0.25 mm	40 (Bedding α=32)	200-210 (Bedding β=202)
	57.9	VNT-10	None	ND	<0.25 mm	60	ND
	59	VNT-10 /UZNT	None	Extensional	ND	50 (Bedding α=50)	070-075 (Bedding β=070-075)
GI-3	11.5–11.7	VNT-3	Striations, 90° to DD	Shear	0.5	30	ND
	20.1	VNT-3	Striations 24° to DD	Shear	ND	35	ND
	24.3–24.4	VNT-3	None	Extensional	ND	32	ND
	25.0–25.1	VNT-3	Striations 0° to DD	Shear	ND	29	ND
	39.6	VNT-3	Striations 90° to DD	Shear	ND	54	ND
GI-4	7.9	VNT-2	Silica infill	Extensional	2 mm → 0 mm along core surface	45	ND
	8.3–8.4	VNT-2	Tan to gray microcrystalline silica infill	ND	0.5 mm → 0mm along core surface	53	ND
	8.7	VNT-2	Striations 0° to DD	Shear	ND	ND	ND
	8.8–9.4	VNT-2	Described by NNSS	Shear	ND	10	ND
	9.4–9.7	VNT-2	White ash, orange to brown infill	Shear	1 mm	10	ND
	12.8–12.9	VNT-3	Striations 90° to DD	Shear	<1 mm	47	210 (Bedding β=350)
	15.9–16.2	VNT-3	Striations 15-30° to DD	Shear	ND	37	315 (Bedding β=350)

Core hole	Drilling Depth (ft)	Unit	Fracture Characteristics				
			Infill or Surface features	Shear or Extensional	Aperture	α (Dip in degrees wrt Core Axis)	β (Strike wrt Bedding Surface)
	17.1–17.3	VNT-3	Striations 0° to DD	Shear	ND	40	320 (Bedding β=350)
	17.8–18.1	VNT-3	ND	ND	1-2 mm	0 to 25	ND
	18.5–18.7	VNT-3	Partial tan to brown silica infill	ND	~0.25 mm	34	ND
	33.2–33.4	VNT-3	Striations 0° to DD	Shear (?)	<1 mm	45	230 (Bedding β=350)
	66.5–66.7	VNT-5	Striations 25° to DD	Shear	ND	35	ND
	83.8–83.9	VNT-5	Striations 30° to DD	Shear	ND	36	ND
GI-6	1.7–1.8	VNT-5	Striations 0° to DD	Shear	ND	40	ND
	2.2–2.3	VNT-5	Striations 0° to DD	Shear	1 mm	58	ND
	40.0–41.8	VNT-5	None	Extensional, parting	<0.5 mm	10	ND
	53.4	VNT-6	Striations 25° to DD	Shear	<0.5 mm	50	ND
	55.3–55.7	VNT-6	Striations ~20° to DD	Shear	<0.5 mm	23	ND
	73.0–73.3	VNT-8	Striations ~75-90° to DD	Shear	<0.5 mm	38	ND
	74.4	VNT-8	Striations ~40° to DD	Shear	ND	56	ND
	77.1–77.3	VNT-8	Striations ~40° to DD	Shear	~1 mm	44	ND
	79.2–79.3	VNT-8	Striations ~40° to DD	Shear	<0.25 mm	56	ND
	86.9–87.1	VNT-8	None	Extensional (?)	<0.25 mm	39	ND
	112.6	VNT-9	ND	ND	<1 mm	58	ND
HF-1	24.4	VNT-2	Brown to pink infill	ND	0.25 mm	11	ND
	49.5	VNT-3	None	ND	~1 mm	16	ND

7.2. Laboratory Geomechanics Tests

A subset of the PE1 core was designated for geomechanical measurements at SNL. These tests consisted of ultrasonic velocity measurements, permeability measurements, and triaxial deformation runs. Triaxial measurements are time- and labor-intensive, thus limiting the number of measurements possible.

Three critical variables were identified to characterize testbed behavior:

1. Geologic unit
2. Confining pressure
3. Saturation condition

To evaluate this parameter space, measurements were grouped into three phases based on saturation conditions (phase 1: fully saturated; phase 2: in-situ saturation; phase 3: dry). For the in-situ measurements, preserved core was used exclusively. Four pressure conditions of interest were identified: 0 MPa, 10 MPa, 50 MPa, and 200 MPa. Finally, four geologic groups of interest were identified based on their visually observed similarity, investigatory Brazilian tests, and availability of samples:

- Group 1: ash-fall tuff (VNT-1 and VNT-3)
- Group 2: pumice-fall tuff (VNT-4)
- Group 3: reworked ashfall tuff (VNT-5)
- Group 4: zeolitic nonwelded tuff (UZNT)

VNT-2 was omitted because it appears to be a unique layer and is very thin and discontinuous in the testbed. UZNT was included in phase 2 of geomechanical testing (in-situ saturation) because the contact with VNT is likely within the elastic radius of the first experiment, and geomechanical characterization is therefore a critical dataset despite only being sampled in a single borehole (AC-1). Details for the samples tested are in Table 14.

To prepare the samples, core was cut and ground into right-circular cylinders. Samples were either kept in their original saturation state (in-situ tests) or dried in an oven overnight to prepare for fully saturated and dried testing. For the in-situ tests, care was taken to expose the preserved samples to air as little as possible and to log times when the samples were exposed during prep. Sample dimensions and masses are shown in Table 14.

Further details can be found in Kibikas et al. [7].

Table 14. Measurement property table for laboratory geomechanics tests performed on geologic core samples. Locations, geologic units, and size of the core are listed along with the pressure and saturation condition under which the tests were performed.

Sample ID	Depth	Unit	Confining Pressure	Saturation	Length	Diam.	Mass	Dens.	Perm.
	ft	-	MPa	-	mm	mm	g	g/cm^3	Y/N
UZNT-AC-1-65.9-66.5	65.9–66.5	UZNT	0	In-situ	136.14	62.63	814.60	1.94	No
UZNT-AC-1-95.4-96.0	95.4–96.0	UZNT	10	In-situ	133.71	62.33	794.60	1.95	No

Sample ID	Depth	Unit	Confining Pressure	Saturation	Length	Diam.	Mass	Dens.	Perm.
UZNT-AC-1-146.5-147.1	146.5 – 147.1	UZNT	50	In-situ	138.81	62.76	842.00	1.96	No
GI-3-58.8-59.7	58.8–59.7	VNT-5	0	Fully	133.40	62.03	597.35	1.48	Yes
GI-2-71.9-73.6-A	71.9–73.6	VNT-5	10	Fully	134.54	62.05	603.30	1.48	Yes
GI-2-71.9-73.6-B	71.9–73.6	VNT-5	50	Fully	133.98	62.36	598.35	1.46	Yes
GI-2-66.1-66.6	66.1–66.6	VNT-5	0	In-situ	134.14	61.80	726.40	1.80	No
GI-4-69.5-70.0	69.5–70.0	VNT-5	10	In-situ	137.16	62.64	769.70	1.82	No
GI-4-62.0-62.7	62.0–62.7	VNT-5	50	In-situ	137.13	62.38	743.90	1.78	No
GI-4-72.4-73.4	72.4–73.4	VNT-5	0	Dry	136.80	62.71	708.4	1.67	Yes
GI-2-71.9-73.6	71.9–73.6	VNT-5	50	Dry	139.95	61.82	615.5	1.46	Yes
GI-4-68.1-69.2	68.1–69.2	VNT-5	200	Dry	135.53	63.09	607.2	1.43	Yes
GI-4-48.8-49.3	48.8–49.3	VNT-4	0	Fully	132.28	62.73	668.00	1.63	Yes
GI-4-47.6-48.8-B	47.6–48.8	VNT-4	10	Fully	132.74	62.71	628.40	1.53	Yes
GI-4-47.6-48.8-A	47.6–48.8	VNT-4	50	Fully	139.29	62.28	662.50	1.56	Yes
GI-4-50.3-50.9	50.3–50.9	VNT-4	0	In Situ	137.39	62.61	828.00	1.96	No
GI-4-37.5-38.1	37-5–38-1	VNT-4	10	In Situ	134.64	62.86	755.00	1.81	No
GI-3-44.6-45.3	44.6–45.3	VNT-4	50	In Situ	137.39	62.61	828.00	1.96	No
GI-4-50.9-51.6	50.9–51.6	VNT-4	0	Dry	137.26	62.76	731.50	1.72	Yes
GI-4-45.3-46.0	45.3–46.0	VNT-4	50	Dry	138.28	62.56	648.90	1.53	Yes
GI-4-42.0-43.2	42.0–43.2	VNT-4	200	Dry	136.22	63.09	755.8	1.77	Yes
GI-4-12.9-13.6	12.9–13.6	VNT-3	0	Fully	138.17	62.484	576.68	1.36	Yes

Sample ID	Depth	Unit	Confining Pressure	Saturation	Length	Diam.	Mass	Dens.	Perm.
GI-3-20.6-21.2	20.6–21.2	VNT-3	10	Fully	133.98	62.97	635.50	1.52	Yes
GI-3-21.8-22.6	21.8–22.6	VNT-3	50	Fully	128.96	62.86	602.00	1.50	Yes
GI-3-21.2-21.8	21.2–21.8	VNT-3	0	In Situ	129.84	62.78	765.10	1.90	No
GI-4-14.5-15.0	14.5–15.0	VNT-3	10	In Situ	141.86	62.64	721.10	1.65	No
GI-2-30.5-31.5	30.5–31.5	VNT-3	50	In Situ	155.07	62.25	856.70	1.82	No
GI-3-15.9-16.4	15.9–16.4	VNT-3	0	Dry	140.61	62.54	656.70	1.52	Yes
GI-2-40.3-41.3	40.3–41.3	VNT-3	50	Dry	132.91	61.67	625.90	1.58	Yes
GI-3-17.6-18.6-B	17.6–18.6	VNT-3	200	Dry	135.84	63.09	639.90	1.51	Yes

7.2.1. Velocity

Compressional (P-wave) and shear (S-wave) velocities were measured using a uniaxial press, with the sample placed between two steel caps, which were covered in a couplant to create good sample contact. An ultrasonic pulse was then generated by a signal producer (Olympus Model 5058PR) and transmitted through the sample. An external oscilloscope (B&K Precision 2559 Digital Storage Oscilloscope) was used to record the waveform transmitted through each sample. P- and S-wave velocities were then identified from the recorded waveform. Velocities were measured both axially (parallel to core axis) and laterally (perpendicular to core axis).

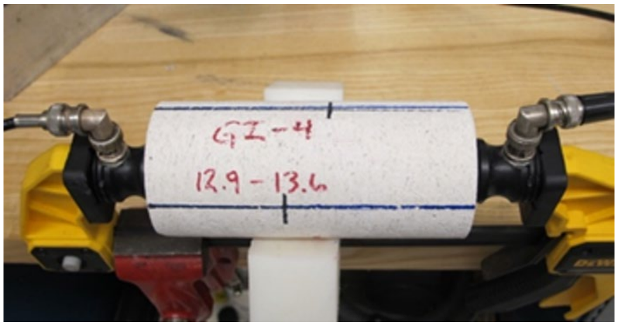

Figure 27. Photograph of a GI-4 core being set up to run velocity measurements.

In general, P- and S-wave velocities tend to increase with geologic unit depth and are on average greater measured in the lateral direction than axial direction. Dry samples exhibit a greater increase in velocity as a function of density than do the partially saturated and saturated samples. Additional details of velocity test data can be found in Kibikas et al [7].

7.2.2. Permeability

Sample permeability to CO_2 and to water was measured for the fully saturated tests, while nitrogen was used to measure permeability for the dry test samples. Each sample was jacketed to seal it from fluids, then placed in a pressure vessel. Gas permeability was first measured using CO_2 or N_2, flowing it through the sample until a stable flow rate and pore pressure were recorded. For the saturated tests, water permeability was measured by first saturating the sample with water for 12 to 36 hours, then flowing water through the sample at a constant rate. By maintaining a differential pressure of CO_2, N_2, or water at each end of the sample, permeability was measured using the flow rate, upstream and downstream pressures, sample dimensions, and fluid viscosities (e.g., Darcy's Law). CO_2 was chosen for the saturated samples to ensure full saturation of the core since CO_2 is easily dissolved in water. At the completion of each triaxial deformation test (described below), permeability was measured using water for saturated tests and N_2 for dry tests.

Pre-test CO_2 permeabilities are generally higher, around 10^{-14} m^2, than water permeabilities, which range from 10^{-14} to 10^{-16} m^2. N_2 permeabilities show a wider range of permeabilities at 10^{-13} to 10^{-16} m^2. Additional details of permeability test data and how they relate to velocity and triaxial deformation data can be found in Kibikas et al [7].

7.2.3. Triaxial Deformation

In preparation for permeability measurement and triaxial deformation, each sample was placed between two steel end caps and jacketed in UV-cure jacketing material to seal it from the confining fluid. Once jacketed, four linear variable displacement transducers (LVDTs) were attached to the sample; two oriented parallel to the sample axis ("Axial") and two perpendicular to the sample axis ("Radial" or "Lateral"). LVDTs mounted on the sample prior to permeability testing measured sample displacement and were used to determine strain during the deformation tests. The upstream and downstream pore pressure controls (Teledyne ISCO pumps shown in Figure 28) were used to monitor sample pore pressure during triaxial testing.

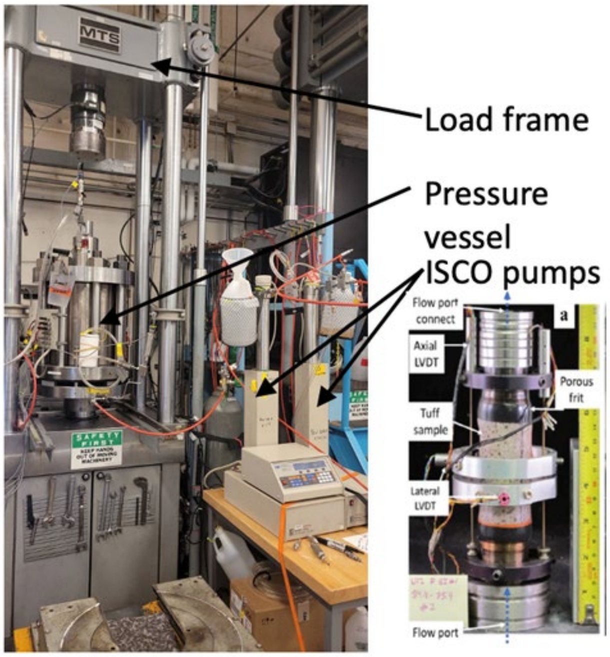

Figure 28. Photograph of the triaxial deformation setup.

After permeability tests were completed, confining pressure was increased to the desired condition except for tests at "0 MPa" where confining pressure was nominally ~0.5 MPa using shop air as a confining medium. Shop air was used to keep a small amount of pressure on the sample jacket during deformation. For the 10 to 200 MPa tests, silicon oil was used as the confining medium for pressurizing the samples. During testing, pore pressure was monitored but not controlled (i.e., undrained condition), allowing the effective pressure (i.e., confining pressure minus pore pressure) to change throughout testing. During hydrostatic loading, the pressure was unloaded and reloaded three to five times at different pressures (e.g., unload-reload loops). The "unloading" portion of these loops was used to determine the bulk modulus K.

Once the desired confining pressure was reached, the samples were axially deformed at a constant strain rate of 10^{-5} s^{-1}. Differential stress (i.e., the difference between axial stress and effective pressure) was unloaded and reloaded three to five times to measure the Young's Modulus E, Poisson's ratio ν, and shear modulus G in a similar manner as during the hydrostatic loops. Differential stress was increased until either 1) failure occurred and the rock failed or 2) steady-state behavior was observed (i.e., no change in behavior is indicated from additional loading). After this step, differential stress was reduced to 0 MPa, then confining pressure was decreased to end the tests. Post-test permeability was then measured using water for saturated conditions and N_2 for dry conditions.

Generally, the tests at 0 MPa experience a stress drop indicative of failure with increasing differential stress. At 10 MPa, differential stress reaches a plateau where stress increases or remains nearly flat even as strain continues to accumulate. At 50 MPa, samples do not experience a stress drop or flattening (except perhaps for 44.6 VNT-4-saturated), as no brittle failure or microcrack coalescence occurs. This behavior is consistent for both the fully and partially saturated tests. Additional details on triaxial deformation and effects on pore pressure and permeability can be found in Kibikas et al [7].

7.3. Geologic and Hydrologic Characterization

Laboratory geologic and hydrologic analyses characterize ten mapped VNT subunits and the UZNT lithology. Table 15 gives a master test matrix with the following: geologic and hydrologic testing types; sample locations along the given corehole to a tenth of a foot or via coordinates in Northing, Easting, and elevation values (SP NAD27) for grab samples; the naming nomenclature; and the lithologic unit from which the sample was taken. Sample selection was based on VNT subunit divisions and textural descriptions within a subunit to ensure selected samples capture heterogeneity within and among each subunit.

Table 15. Test matrix with geologic unit, sample ID, and testing types denoted by specific locations for samples, namely drilling depth to a tenth of a foot for core and SP NAD27 coordinates and elevation for grab samples.

<table>
<tr><th rowspan="2">Lith. Unit</th><th rowspan="2">Sample ID</th><th>Petrography</th><th>Spatial XRF</th><th>X-ray CT</th><th>XRD</th><th>TGA</th><th>MICP</th><th>Water Content</th><th>Porosity, permeability, grain- & bulk-density</th></tr>
<tr><th colspan="6">Specific location for sample by drilling depth (ft), which may apply to multiple testing types; blank and gray means no sampling for the specific test in the given column</th><th colspan="2">SP NAD 27 coordinates for sample location</th></tr>
<tr><td>VNT-1</td><td>GI-2-6</td><td>6.4</td><td></td><td></td><td colspan="2">6.4</td><td></td><td></td><td></td></tr>
<tr><td rowspan="2">VNT-2</td><td>GI-3-2</td><td>2.3</td><td></td><td></td><td colspan="2">2.3</td><td></td><td></td><td></td></tr>
<tr><td>GI-4-8</td><td>8.3</td><td></td><td></td><td colspan="2">8.3</td><td></td><td></td><td></td></tr>
<tr><td rowspan="6">VNT-3</td><td>GI-4-18</td><td>18.4</td><td></td><td></td><td colspan="2">18.4</td><td>18.5</td><td></td><td></td></tr>
<tr><td>GI-4-35</td><td colspan="2">35.1</td><td></td><td colspan="2">35.1</td><td>35.3</td><td></td><td></td></tr>
<tr><td>PE1-U12p06-1280-13</td><td></td><td></td><td></td><td></td><td></td><td></td><td colspan="2">N905939.5, E647958.0, 5521.8 ft elevation</td></tr>
<tr><td>PE1-U12p06-1190-4</td><td></td><td></td><td></td><td></td><td></td><td></td><td colspan="2">N905814.6, E647948.2, 5520.6 ft elevation</td></tr>
<tr><td>PE1-U12p06-1190-13</td><td></td><td></td><td></td><td></td><td></td><td></td><td colspan="2">N905814.8, E647926.6, 5522.6 elevation</td></tr>
<tr><td>GI-4-44</td><td>44.5</td><td></td><td></td><td></td><td></td><td>44.5</td><td></td><td></td></tr>
<tr><td rowspan="7">VNT-4</td><td>GI-4-54</td><td colspan="3">54.2</td><td colspan="2">54.1</td><td>54.5</td><td></td><td></td></tr>
<tr><td>GI-4-49</td><td colspan="2">49.5</td><td></td><td colspan="2">49.5</td><td></td><td></td><td></td></tr>
<tr><td>GI-3-51</td><td>51.2</td><td></td><td></td><td colspan="2">51.2</td><td></td><td></td><td></td></tr>
<tr><td>PE1-U12p06-1490-25</td><td></td><td></td><td></td><td></td><td></td><td></td><td colspan="2">N906133.6, E647972.0, 5520.0 ft elevation</td></tr>
<tr><td>PE1-U12p06-1280-22</td><td></td><td></td><td></td><td></td><td></td><td></td><td colspan="2">N905950.3, E647942.4, 5521.2 ft elevation</td></tr>
<tr><td>PE1-U12p06-1280-31</td><td></td><td></td><td></td><td></td><td></td><td></td><td colspan="2">N905962.2, E647929.2, 5522.4 ft elevation</td></tr>
<tr><td>GI-2-65</td><td>65.6</td><td></td><td></td><td colspan="2">65.6</td><td></td><td></td><td></td></tr>
<tr><td rowspan="5">VNT-5</td><td>GI-4-72</td><td colspan="4">73.2</td><td></td><td>73.3</td><td></td><td></td></tr>
<tr><td>PE1-U12p06-1280-34</td><td></td><td></td><td></td><td></td><td></td><td></td><td colspan="2">N905962.3, E647928.8, 5521.1 ft elevation</td></tr>
<tr><td>PE1-U12p06-1190-16</td><td></td><td></td><td></td><td></td><td></td><td></td><td colspan="2">N905814.6, E647905.4, 5519.4 elevation</td></tr>
<tr><td>PE1-U12p06-1190-25</td><td></td><td></td><td></td><td></td><td></td><td></td><td colspan="2">N905814.7, E647891.5, 5518.2 ft elevation</td></tr>
<tr><td>VNT-6</td><td>DA-1-17</td><td>17.2</td><td></td><td></td><td colspan="2">17.2</td><td>17.1</td><td></td><td></td></tr>
<tr><td>VNT-7</td><td>DA-1-19</td><td>19.3</td><td></td><td></td><td colspan="2">19.2</td><td></td><td></td><td></td></tr>
<tr><td>VNT-8</td><td>DA-1-25</td><td>25.6</td><td></td><td></td><td colspan="2">25.7</td><td></td><td></td><td></td></tr>
<tr><td>VNT-9</td><td>DA-1-35</td><td>35.7</td><td></td><td></td><td colspan="2">35.8</td><td></td><td></td><td></td></tr>
<tr><td>VNT-10</td><td>DA-1-36</td><td>36.7</td><td></td><td></td><td colspan="2">36.8</td><td>36.7</td><td></td><td></td></tr>
<tr><td rowspan="6">UZNT</td><td>AC-1-65</td><td>65.8</td><td></td><td></td><td colspan="2">65.9</td><td></td><td></td><td></td></tr>
<tr><td>AC-1-71</td><td>71.7</td><td></td><td></td><td colspan="2">71.8</td><td></td><td></td><td></td></tr>
<tr><td>AC-1-111</td><td>111.4</td><td></td><td></td><td colspan="2">111.5</td><td>111.4</td><td></td><td></td></tr>
<tr><td>PE1-U12p06-AC-1-92.5-92.9</td><td></td><td></td><td></td><td></td><td></td><td></td><td colspan="2">92.7</td></tr>
<tr><td>PE1-U12p06-AC-1-120.3-120.8</td><td></td><td></td><td></td><td></td><td></td><td></td><td colspan="2">120.4</td></tr>
<tr><td>PE1-U12p06-AC-1-151.5-152.0</td><td></td><td></td><td></td><td></td><td></td><td></td><td colspan="2">151.6</td></tr>
</table>

7.3.1. Geologic Characterization

Geologic characterization data supports the identification of lithologies, secondary mineral alteration, and their variability both within and among the various geologic units of the PE1 testbed. As the PE1 testbed is located near a geologic transition zone between mostly vitric and mostly zeolitic units, the rock composition and pore structure can vary greatly within and between lithologic units, which in turn may affect fluid flow, tracer transport, and geomechanics.

All testbed lithologic units (VNT-1 through VNT-10 and UZNT) were subsampled at least once and up to three times each, and these subsamples were used for thin section petrography, spatial X-ray florescence (XRF), X-ray diffraction (XRD), and X-ray computed tomography (CT). Textural descriptions within a subunit ensure selected subsamples capture heterogeneity within and among each subunit. These data support the understanding of geologic controls on heterogeneity and support calibration of petrophysical logging as needed.

7.3.1.1. Petrography

Rock samples were prepared into billets with a Buehler IsoMet 1000 Precision Saw using deionized water (DI) as lubricant. The trimmed rock samples were shipped to Wagner Petrographics for standard petrographic thin sections at 27 mm × 46 mm area and 30 μm thickness, with corresponding polished billets for each thin section. The rock samples were impregnated with low viscosity fluorescent red-dye epoxy resin under high vacuum to accentuate pores. The polished epoxied billets have approximately the same area of the standard thin sections, but are thicker (e.g., approximately 10 mm, but it can vary) to allow for study of three-dimensional pore structure (e.g., via X-ray CT or laser scanning confocal microscopy on the fluorescent epoxy) that is closely linked with 2D analysis on the top surface of the polished billet (e.g., via SEM-EDS or spatial XRF). Optical petrography was performed on all thin sections with a Zeiss LSM 900 using plane polarized and cross-polarized transmitted light, as well as reflected light. A series of at least two reflected light and two transmitted light images (both plane and plane-polarized) at low (50×) and high (200×) total magnification were taken for each thin section. A photomosaic of each thin section was also obtained at 50× total magnification using the Zen Imaging System for the Zeiss LSM 900 (Figure 29).

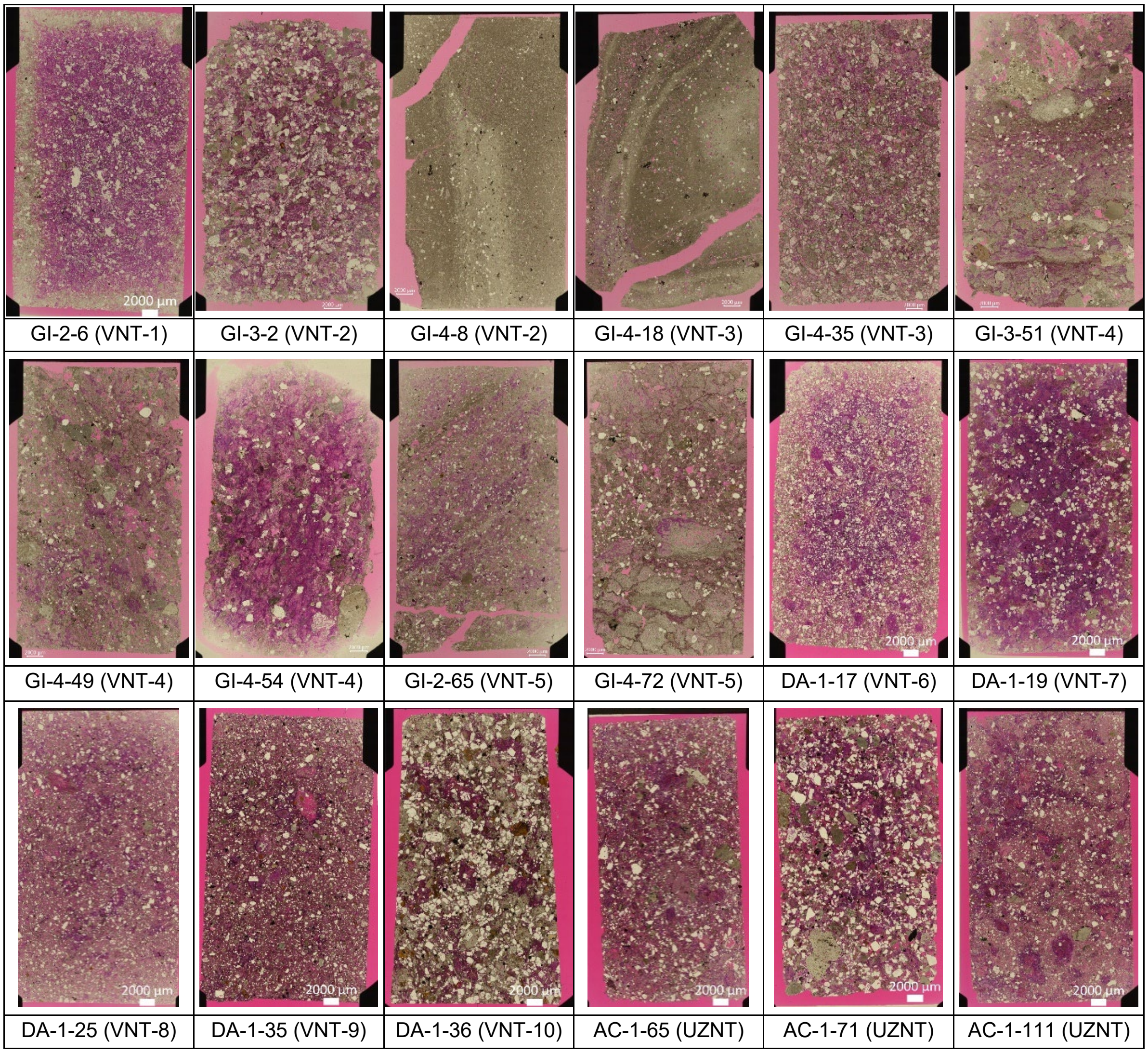
GI-2-6 (VNT-1) GI-3-2 (VNT-2) GI-4-8 (VNT-2) GI-4-18 (VNT-3) GI-4-35 (VNT-3) GI-3-51 (VNT-4)

GI-4-49 (VNT-4) GI-4-54 (VNT-4) GI-2-65 (VNT-5) GI-4-72 (VNT-5) DA-1-17 (VNT-6) DA-1-19 (VNT-7)

DA-1-25 (VNT-8) DA-1-35 (VNT-9) DA-1-36 (VNT-10) AC-1-65 (UZNT) AC-1-71 (UZNT) AC-1-111 (UZNT)

Figure 29. Inventory of thin sections via photomosaic imaging in transmitted plane light on Zeiss LSM 900. Corresponding epoxied billets were made for each of these thin sections (billets not shown). Each image is a mosaic of 5× plane polarized transmitted light sub-images taken over the entire given thin section. The standard thin sections are 24 mm × 46 mm × 30 µm.

Petrographic observation and quantitative analysis include the following: description of texture; a 300-point count for abundances of framework grains, non-framework components, and total porosity; types and abundances of framework and non-framework components; porosity types, including a 100-point count specifically on pore types (e.g., intergranular or intragranular); diagenesis, including type and nature of secondary mineralization (e.g., pore-filling or replacement), degree of compaction, and deformation features (fractures or grain crushing).

Relative abundance of framework grains (i.e., pumice, phenocrysts), matrix (i.e., ash), and porosity types varies greatly among VNT units 1 through 10 and the UZNT. The distribution or arrangement of these phases, including what solid phases line pores and will be exposed to directly to fluids, also varies. As expected, ash-fall tuffs (VNT-1, VNT-3, VNT-6, VNT-8, and VNT-9) tend to have more matrix material than pumice, and pumice-fall tuffs (VNT-2, VNT-4, VNT-7, and VNT-10) are dominated by pumice. Exceptions include a silicified VNT-2 sample, a pumice-rich VNT-3 sample, and phenocryst-rich VNT-10 sample with abundant clay, zeolite, and opal. Porosities range from 9.4% for silicified and zeolitic samples to 36.3% for more vitric samples. Thin section images and detailed petrographic data can be found in Wilson et al. (2024) [22].

7.3.1.2. SEM-EDS

Thin sections were prepared for SEM by coating them with a gold-palladium alloy using a Denton Vacuum Desk IV sputter-coater. The microtexture of each thin section was observed and imaged using backscattered electrons (BSE) and secondary electrons (SE) in high-vacuum mode at an accelerating voltage of 20.0 kV on a TESCAN Vega3 Scanning Electron Microscope. To confirm the presence of key primary and alteration minerals (zeolite, silica, clay minerals, etc.), elemental compositions from select portions of each thin section were obtained using an energy dispersive X-ray (EDAX) system. Energy dispersive spectra (EDS) were collected and analyzed using an Oxford Instruments Xplore 3D EDS detector and Aztec EDS software, version 6.0.

BSE images of volcanic tuff provide a clear view of pore and crystal morphologies due to the readily apparent difference between pores (black) and pore-lining phases (grayscale value dependent on atomic weight). BSE and EDS elemental overlay maps show a progression of volcanic tuff that is mostly vitric with incipient alteration to zeolite and smectite, to tuff with no glass content and correspondingly higher zeolitic content with varying amounts of smectite alteration and silica cementation. These alteration minerals both replace glass and partially to completely (depending on degree of alteration) fill inter- and intragranular pores. BSE and EDS map images can be found in Wilson et al. (2024) [22].

Zeolite morphologies vary, including wispy (e.g., VNT-4, U12p.06 GI-4-54), skeletal (e.g., VNT-1, U12p.06 GI-2-6; VNT-3, U12p.06 GI-4-35; VNT-6, U12p.06 DA-1-17), needle-like, and blocky crystals (e.g., UZNT, U12p.06 AC-1-111) growing into pore spaces. Complete closure of pore space can be found in some regions in zeolitized samples (e.g., UZNT, U12p.06 AC-1-111). Generally, zeolite is enriched in Ca and Mg, and depleted in K and Na compared to the volcanic glass that it replaces. Variations in Si, Al, Na, and K abundances within zeolite are observed and likely reflect different zeolite varieties (clinoptilolite, heulandite, and mordenite) that may form under dynamic diagenetic conditions (e.g., Chipera et al., 2006) [2]. Fe- and Mg-enriched smectite occurs as clumps intermixed with zeolite within pumice vesicles and between grains and commonly exhibits desiccation microcracks. Silica cementation is often nodular and appears to form in pores after alteration of volcanic glass to varying amounts of zeolite and smectite (e.g., VNT-4, U12p.06 GI-4-49).

7.3.1.3. X-Ray Diffraction

Samples for XRD were prepared from rock material trimmed away from each thin section billet so that the XRD results correlate to optical petrography and SEM observations. Trimming was performed with a Buehler IsoMet1000 precision saw using DI water as lubricant. The material removal for XRD was such that it would provide at least 10 grams of ground-up material. The rock material was sent to Premier Oilfield Group LLC, which performed bulk and clay-sized fraction analyses. The XRD analysis equipment includes Bruker D8 and D4 diffractometers with a 2θ goniometer and 250-cm radius, Cu $K\alpha$ radiation, a SSD160 Lynxeye detector, and a 0.6 mm divergence slit and 4.1° Soller slits for optimal intensity-resolution ratio. Sample preparation included homogenization, McCrone wet milling, spray drying, and front or side loading.

The clay-size fraction at <2 μm was obtained by sonication and centrifugation, and oriented clay preparation used a filter transfer method. Clay expandability was determined using the clay separation-glycolation-heat treatment method (Moore and Reynolds, 1997), aided by the NEWMOD clay modelling software. Mineral quantification used the Reference Intensity Ratio method, aided by Bruker EVA DIFFRAC SUITE software and the PDF4+ mineral database, and quantification was performed using customized Mineral Intensity Factor (MIF) values obtained from commercial and in-house standards. The mineral percentages are reported as weight percent.

The VNT units of the PE1 testbed can contain highly variable, and at times very high percentages, of secondary (i.e., diagenetic) phases including zeolites (e.g., clinoptilolite or heulandite), clay, and opal. Zeolite contents range from 2.4 to 63.4 wt%, with the highest levels in units VNT-4 and VNT-5. Amorphous volcanic glass contents range from 14.4 to 18.0 wt% in UZNT samples and 18.5 to 68.0 wt% in VNT samples. Clay contents range from 1.1 to 33.4 wt%, with VNT-2 through VNT-5 containing Na-smectite and VNT-1, vitric VNT-4, VNT-6 through VNT-10, and UZNT containing Al-smectite. Detailed bulk and clay-sized fraction XRD results can be found in Wilson et al. (2024) [22].

7.3.1.4. Spatial X-Ray Florescence

A Bruker M4 Tornado μ-XRF mapping system was used for spatial X-ray fluorescence mapping on polished thin sections or polished epoxied billets. The system includes a micro-focused Rh source (50 kV, 200 μA) with a poly-capillary optic and a silicon-drift detector for collection of fluorescence spectra at approximately 25 μm spatial resolution (see Rodriguez et al., 2012) [17]. The XRF scanning produces spectra (intensity versus energy) for each pixel where the mapping step size was 50 microns in both x and y dimensions, thus resulting in large data cubes that require post-processing to reduce the per pixel spectrum to spatially significant groups of phases (e.g., minerals or non-mineral mineraloid or amorphous phases such as opal or glass). SNL's in-house principal component analysis (PCA) and multivariate statistical analysis (MSA) software is used for post-processing the spatial spectral data (Kotula et al., 2006 [9]; Rodriguez et al., 2012 [17]; see Heath et al., 2012 [4], for a geologic application of the MSA software).

Post-processing of the spatial XRF data produces two-dimensional (2D) maps of the solid phases (minerals, mineraloids, and amorphous phases) in terms of a score from the PCA with an associated representative spectrum for the scored phases, which can be used in further post-processing (e.g., via segmentation for quantification of phases). The PCA analysis used 2×2 binning on the spatial XRF data, and thus the PCA resulting resolution is 100 μm.

Notable findings include that the spatial XRF with PCA can distinguish diagenetic zeolite from different types of silica, including crystalline quartz and amorphous phases such as volcanic glass and opal. Zones of different types of diagenesis are visible (e.g., opal deposition versus zeolite crystallization). 2D maps of analyzed samples, images of the PCA-scored maps, and spectra of dominant phases can be found in Wilson et al. (2024) [22].

7.3.1.5. X-Ray Computed Tomography

Two billets were scanned by X-ray CT with a Zeiss Xradia 620 Versa. These two billets were chosen for comparison between vitric (VNT-4, GI-4-54) and zeolitized (VNT-5, GI-4-72) samples. Data were collected on a flat panel detector with 21- or 23-μm voxel size over the entire billets, and data were also collected with a reduced field of view and higher resolution at 5.8 or 5.9 μm voxel size. Re-alignment and export of image stacks of the datasets were performed with Fiji ImageJ software

(Schindelin et al., 2012) [18]. Air regions and artifact sections of the dataset were cropped out during that process.

3D rendering was performed using Avizo™ 3D 2021.2 software by Thermo Fisher Scientific of the full billets and the sub-volume scans, including 2D images at various orientations to give the reader a feel for the differences in the high- and low-resolution datasets in terms of resolvable features (e.g., the 21 and 23 μm datasets do not resolve many fine features visible in the 5.8- or 5.9-μm datasets). 3D renderings and representative 2D image slices from the vitric and zeolitic samples at both resolutions can be found in Wilson et al. (2024) [22].

7.3.2. Hydrologic Characterization

Hydrologic characterization data are used to investigate in situ water content from samples preserved in the field against dry-out and fluid flow properties (porosity, permeability) to support numerical modeling of multiphase fluid flow and gas transport of the PE1 testbed.

Hydrologic laboratory testing focused on the following: multiphase fluid flow properties and further understanding of pore size distribution via mercury intrusion capillary pressure (MICP) measurements; water content as based on "hand" samples preserved in the field during mining operations, with supplemental thermogravimetric analysis (TGA); and porosity, permeability, bulk density, and grain density. The MICP data enable the assessment of capillary heterogeneity for the various sampled geologic units, and the MICP data are used to predict absolute and relative permeabilities (Swanson, 1981) [20]. In situ water content was measured on preserved samples because companion geomechanical testing is being performed on as-received and preserved core samples that correspond to the hand samples. Gravimetric and volumetric water content measurements include heating to 60°C, which may measure water that is available for flow, whereas TGA was used to inform on sorbed and structural water of solid phases.

Though samples used for hydrologic characterization were preserved, they may have been influenced by drilling fluid (cores) or mining (grab samples). These perturbations are largely unavoidable as they are required to collect the samples. Care was taken to collect and preserve the samples as quickly as possible to minimize the second altering factor, dry out, due to open air exposure. Even so, these variabilities in post-drilling saturation should be considered when interpreting the hydrologic characterization of the samples and when comparing core samples to grab samples. Further details can be found in Wilson et al. (2024) [22].

7.3.2.1. Mercury Intrusion Capillary Pressure

MICP measurements, including an extrusion phase, were collected on a Micrometrics AutoPore IV 9500 Series porosimeter by CoreSpec Alliance, LLC. Samples were typically ~ 0.9-inch diameter × 0.9 inch long to fit into the penetrometer cup of the porosimeter, but some samples were irregular. All samples were dried in a vacuum oven at 100°C for ~24 hours, and photos were taken. Samples were weighed and analyzed on the AutoPore IV and set to reach equilibrium by time (e.g., 30 seconds at both low and high pressure). Low-pressure intrusion proceeded to approximately 27 psia, after which the high-pressure intrusion commences, taking the pressure up to ~ 60,000 psia. The extrusion stage included monitoring volumes of mercury leaving the sample as pressure was returned to approximately atmospheric conditions. Data post-processing performed by Corespec Alliance, LLC, included corrections for "conformance," which is the volume of mercury that entered the penetrometer cup but did not actually intrude into the pore space of the samples.

MICP-derived porosities range from 16.08 to 50.41%, with the lowest values found in phenocryst-rich zeolitized samples and higher values in vitric pumice-fall samples. These results generally agree with petrographically determined porosities, with notable differences for a zeolitized VNT-4 sample that is 10% higher, a vitric VNT-4 sample that is 15% lower, and a zeolitized VNT-5 sample that is 11% higher than lab-derived porosities. These differences are likely related to differential intrusion of mercury, which can forcefully open pores defined by delicate glassy particles in vitric samples or can be blocked by pore-closing zeolites and clay in reworked and altered samples.

Bulk densities range from 1.13 to 1.99 g/cm^3, with the lower densities found in vitric samples and the highest densities for pumice-fall deposits that are rich in lithic clasts and phenocrysts.

Median pore throat radii range from 0.013 to 4.292 microns, with the largest values commonly in vitric samples. Swanson permeabilities range from 0.3 to 226.9 mD, with larger values associated with vitric pumice-fall samples.

Details of these MICP-analysis-derived rock properties, as well as plots of the ranges in pore sizes, individual pore size distributions, and mercury saturation versus pore size for each sample can be found in Wilson et al. (2024) [22].

For potential use in numerical modeling, MICP data can be converted to the air-water system (or other fluid pair systems) and fit with capillary pressure models. Such fits can also be used to estimate or predict relative permeability as a function of saturation (Heath et al., 2021) [5]. Furthermore, MICP data measured on samples from different locations or lithologies, as parameterized for ready comparison to each other, can help characterize heterogeneity in multiphase fluid flow properties. Thus, following methods of Heath et al. (2021) [5], the MICP curves were converted to the air-water system using air-water-rock contact angles of 16.75° for the vitric samples and 17.52° for the zeolitized samples—these contact angle values are based on measurements on samples that were Argon ion milled. Uni-modal and bi-modal VG model Markov chain Monte Carlo fits, including relative permeability predictions based on the VG fitting parameters for water and gas (Kuhlman et al., 2022) [10], as well as additional figures and values of these parameters can be found in Wilson et al. (2024) [22].

7.3.2.2. Thermogravimetric Analysis

Thermogravimetric analyses were conducted under a nitrogen environment using the SDT650 thermal analyzer by TA Instruments. Powdered samples from the same material used in XRD analysis were analyzed. In addition, one non-powdered chip for sample DA-1-19 at ~5 mm in diameter was analyzed to compare with the powder TGA. About 20 to 50 mg of the powdered samples were loaded in alumina pans of 6.55 mm outer diameter × 4 mm height.

Heating-ramp and holding sequences were as follows:

- ramp 1 °C/min to 27°C and hold for 240.0 mins;
- ramp 5 °C/min to 100°C and keep isothermal for 240 mins;
- ramp 5 °C/min to 200°C and keep isothermal for 240.0 mins; and
- ramp either 5 or 10 °C/min from 200°C to 900°C.

For natural clinoptilolite-bearing tuff samples from the NNSS, Knowlton et al. (1981) [8] used TGA to distinguish three types of water that can be associated with zeolite clinoptilolite: external water, loosely bound, and tightly bound water, with transitions at temperatures of 75 ± 10°C, 171 ± 2°C and 271 ± 4°C, respectively. These temperatures were determined by TGA under vacuum conditions, and those authors noted that the temperature transitions are ~50°C higher under heating in a nitrogen atmosphere. However, Bish (1993) [1] in reviewing thermal behavior of zeolites states "distinct 'types' of water (e.g., loosely bound or tightly bound zeolitic water) do not exist" and instead speaks of water bound to extra-framework cations with a continuum of energies, and that the amount of water in structural cavities of zeolite affects the zeolites' molar volume.

We generally consider that the weight loss at 100°C or less is corresponding to external water, weight loss at 100–200°C is mostly loosely bound water, and the weight loss at > 200°C is tightly bound water. While most of the water loss is related to heating and thus is relatively stable, the weight loss at 27°C, ~1/3 of the total water, is the least stable, or rather, most mobile water and can be variable based on the sample handling and exposure to moisture. The TGA samples have variable amount of water loss, ranging from 6% to 12.3%. From 200 to 900°C the water loss is 1.6 to 3%, which may be consistent with clinoptilolite tuff for "tight bounded water" reported by Knowlton et al. (1981) [8]. Further careful interpretation is needed for these complex multi-mineral and mineraloid samples as they can contain other water-sensitive phases such as swelling clay (e.g., smectite) and opal (SiO2·nH2O). Additional details can be found in Wilson et al. (2024) [22].

7.3.2.3. In-situ Water Content

Water content estimates were made using grab samples (approximately fist-sized or "hand") preserved in the field during mining for units VNT-3, VNT-4, VNT-5, and UZNT. Grab samples were not available from UZNT, so preserved core was used.

Gravimetric or mass-based water content determinations are based on the ratio of the mass of the water in the preserved sample over the mass of the dry solids in the sample, which is also called mass wetness w, where w = M_w/M_s (subscript w = water; s = solids; and M = mass). Methods from ASTM D2216–19 could be applied, but they may need to be modified to account for the water-sensitive solid phases (e.g., clinoptilolite, smectite, and opal). Methods used for this study included drying at 60°C in a convection oven with a drying time of over 72 hours (Figure 30). Note that future review of the TGA data may allow for a refined or more justified choice of drying temperature for these samples. Hand samples used in measurement of mass wetness were sub-cored and used to obtain dry bulk density, and mean particle or grain density via helium pycnometry.

Volume measurements of the irregularly shaped hand samples were attempted with a water-displacement method that was evaluated and shown to be inaccurate. A Creality 3D Scanner Kit with 0.05 mm accuracy was used to obtain the volume of the irregular hand samples to allow conversion of mass wetness to volumetric water content. For validation of the 3D scanner data, one sample was X-ray CT-ed with the Zeiss Xradia 620 Versa instrument, and the image data masked to the outer margin of the sample by marker-based watershed methods using Avizo™ 3D 2021.2 software by Thermo Fisher Scientific (Figure 30), and the label analysis module of Avizo™ was used on the binarized sample to determine the sample's volume, which for sample 12p06-1280-U-DLS-H-025-Practice-1 is 163.7 cm^3; thus, the volumetric water content of this originally preserved sample is 0.18. As a check, we use the formula $\theta = w(\varrho_b/\varrho_w)$, and assuming a water density of 1 g/cm^3, we estimate a dry bulk density of 1.7 g/cm^3, which is similar to typical values calculated by MICP. Confidence intervals for saturation are based on best estimates of measured values. Volumetric water contents range from 0.14 to 0.16 for VNT-3, 0.18 to 0.23 for VNT-4, 0.26 to 0.31 for VNT-5, and 0.33 to 0.37 for UZNT samples. Data for individual samples and associated calculations can be found in Wilson et al. (2024) [22].

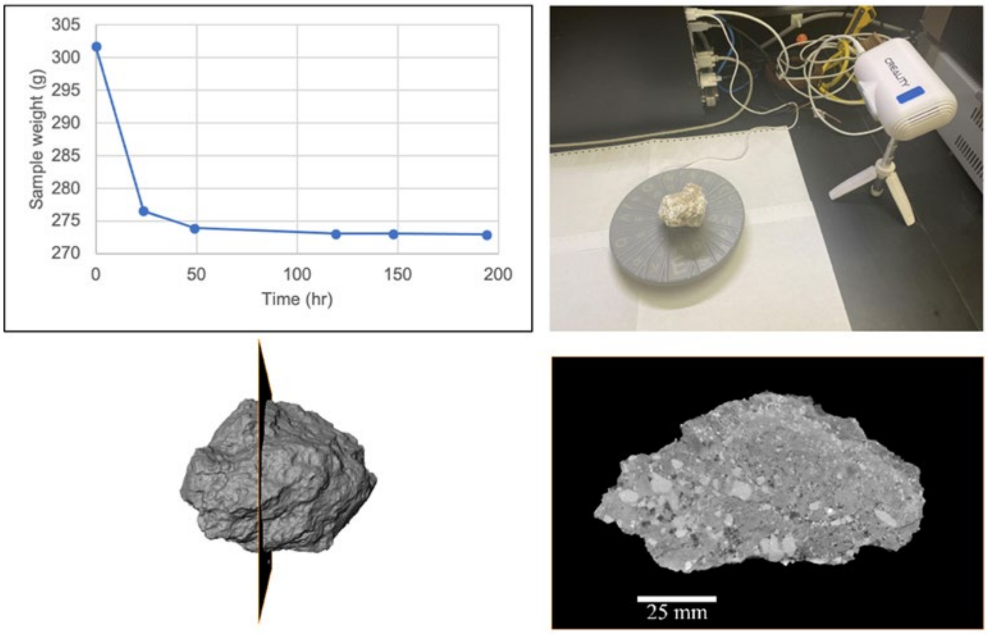

Figure 30. (Upper Left) Sample weight versus time for drying of sample 12p06-1280-U-DLS-H-025-Practice-1 in a convection oven at 60°C. (Upper Right) Photo of the 3D scanning set up used to image the irregular samples. (Lower Left) 3D rendering and (Lower Right) 2D images of the "hand" sample 12p06-1280-U-DLS-H-025-Practice-1 based on X-ray CT scanning, which was used to calculate the sample's total volume of 163.7 cm^3.

7.3.2.4. Porosity, Permeability, Density

Porosity measurements using a helium porosimeter and methods following Jones and Associates (1985) [6] were made on right cylindrical rock samples that were subsequently used in the permeability measurements. Porosities range from 33.47% to 35.19% for VNT-3 samples, 20.08% to 33.23% for VNT-4 samples, 29.79% to 42.18% for VNT-5 samples, and 28.52% to 35.00% for UZNT samples.

Nitrogen gas permeability measurements were made on the same samples as for porosity with a UV cured urethane jacket. The jacket prevented the permeant from flowing along the sample perimeter. The samples were confined under 80 psi (shop air) pressure to keep the jacket from delaminating from the sample surface. Metal porous frits were placed on each end of the sample and combined with endcaps that had a center port for air flow, which provided a way for gas to flow evenly across the ends of the sample. A fixed upstream gas pressure was applied, and the downstream pressure was atmospheric. The flowrate was measured along the sample downstream line and regulator with a standard flow meter calibrated for Nitrogen gas. Darcy's law was used to estimate permeability. Permeabilities range from 7.98E-14 to 2.71E-12m^2 for VNT-3, 1.15E-13 to 7.42E-13m^2 for VNT-4, 1.99E-13 to 1.27E-10m^2 for VNT-5, and 1.99E-13 to 5.46E-08m^2 for UZNT. Porosity, grain density, and permeability data for individual samples can be found in Wilson et al. (2024) [22].

This page left blank

8. BACKGROUNDS

Analysis of the existing background levels of planned tracers, geogenic gases, High Explosive (HE) byproducts, and other radioactive sources is important to PE1 to better understand the signals collected by both real time sensors and physical samples during the experiments. These backgrounds are also important for planned activities such as confinement leak testing. Because P-Tunnel has been used historically as a testbed for underground nuclear explosive tests, background levels of certain experimental byproducts may be elevated and thus important to characterize before PE1 HE experiments are conducted.

Several background gas collection campaigns were conducted inside the tunnel, separated into two categories. Small-volume gas samples were collected underground and on the apron for analysis of various analytes relevant to the experiment and for backgrounds relevant to grout plug leak tests. Large-volume gas samples were collected from the GS boreholes and from the Experiment A emplacement location and were primarily for xenon analysis.

Additionally, absorbent silica beads were emplaced throughout the tunnel to collect backgrounds from moisture in the tunnel air. Several radiological swipe analyses from materials leaving the tunnel were also logged.

Directly preceding Experiment A, gas and liquid samples were collected using the gas collection instrumentation sourced from the GS boreholes and Tunnel Environment (TE) locations, and water traps, respectively.

Analysis of these background samples is performed by multiple labs, each with their own scientific interest and technical expertise. The analytes and goals of the individual labs are detailed in Table 16.

Table 16. Distribution of Background samples to the various labs. PNNL: Pacific Northwest National Laboratory; SNL: Sandia National Laboratories; LANL: Los Alamos National Laboratories; NNSS: Nevada National Security Sites.

Analyte	Goals	Lab	Type
D_2O/HT	Check fractionation species specific transport and transport to the boreholes	PNNL	Small Volume Gas Samples
Geogenic Gas	Quantify gases released from emplacement geology when crushed/damaged	SNL	Small Volume Gas Samples
HE Gas	Test for HE gases that leak through confinement or to the boreholes	LANL	Small Volume Gas Samples
Xe-126/Xe-127	Check the transport of Xe to the boreholes	PNNL	Large Volume Gas Samples
HTO	Evaluate tritium backgrounds	PNNL	Liquid Absorbent Samples
Freon/SF6	Support Confinement grout plug planning and verification	Intertek	Confinement Leak Test Samples
Radioactivity (Alpha/Beta)	Document release of materials from tunnel and characterize RAD hazard	NNSS	Radiologic Swipes

8.1. Small-Volume Sampling

Small volume gas samples (SVGS) were collected using the same 2.7 L stainless steel (Entech) bottles that will be used in the gas sampling system operating during the experiment (Figure 31).

These bottles were fitted with an automated timer (Entech TM1200) and a particulate filter. Bottles were cleaned and vacuum pulled at SNL. The timer was programmed to open at a designated time, drawing a whole air sample into the container, and close six hours later. Gas samples were under ambient pressure upon their sealing. The collection was performed over a weekend when the tunnel was inactive, and the ventilation system was turned off. This strategy was followed to best mimic the conditions under which Experiment A was conducted.

Figure 31. Photograph showing (left) the emplacement of a small volume gas sampler and liquid absorbents in the tunnel drift, (upper right) the small volume gas sampler system configuration, and (lower right) an example liquid absorbent sample.

Samples were collected at 15 locations in total over the span of three weekend-long campaigns (Figure 32). Several locations were duplicated so that the variance in the samples could be investigated. Note: SVGS-4 experienced a malfunction during emplacement, which may have resulted in a sample being collected with the tunnel ventilation on rather than over the weekend with it off.

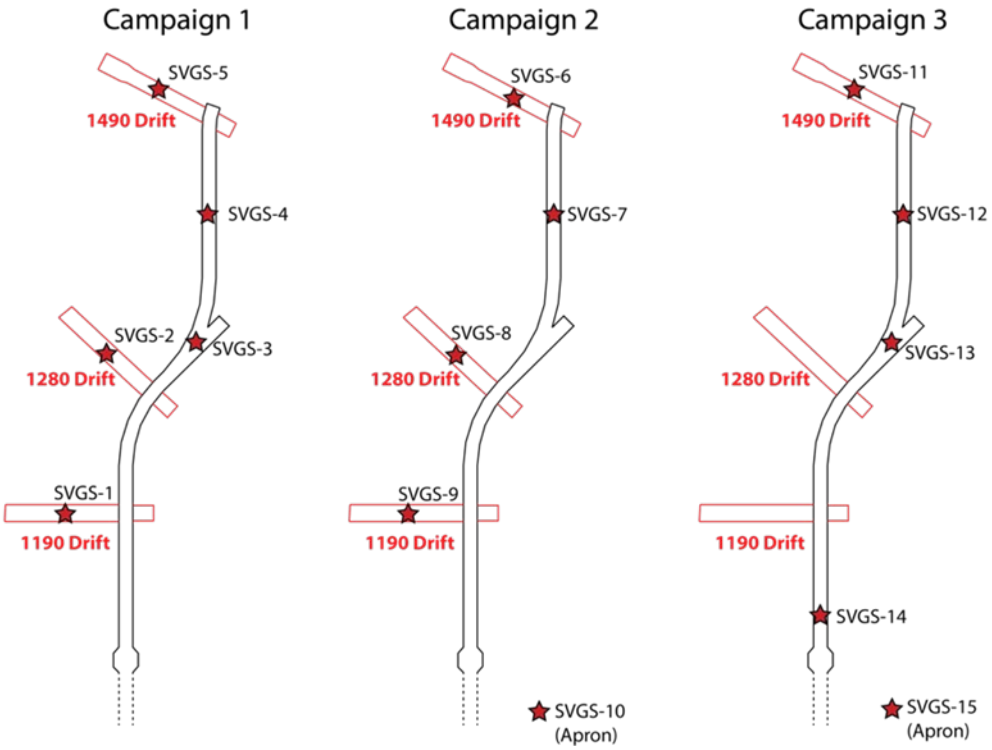

Figure 32. Locations of the small volume gas samplers and liquid absorbents over the three emplacement campaigns.

Multiple labs have an interest in the small volume samples, so the initial 2.7-L sample was split, to create three subsamples. Splitting was done by equilibrating pressure between the subsamples under vacuum and the primary sample under ambient pressure. The splitting was done at the NNSS for Campaign 1 and at SNL for Campaigns 2 and 3.

This splitting process was found to be inefficient when considering the scale needed for post Experiment-A sample management and the glass bottles were found to be less desirable. It was decided that the labs would process samples in serial with the original gas containers being shipped to the first lab, aliquoted, then passed to the next lab in the chain.

8.2. Liquid Absorbent Sampling

Liquid absorbent samples were collected concurrently with the small volume gas samples, sharing sampling locations and general timing (Figure 33). High-purity grade silica gel (Sigma Aldrich Cat. No. 227196) was used as the absorbent and was contained in a Nalgene Polypropylene copolymer vial. Liquid absorbents were emplaced and opened on the Thursday afternoon of the collection and were closed the following Monday morning, allowing collection throughout the weekend when the tunnel ventilation was off (the facility is typically closed on Fridays). Liquid absorbents were analyzed at the Pacific Northwest National Laboratory (PNNL) for tritiated water (Table 17).

Table 17. Average mass normalized activity in mBq and TU (Tritium Unit). The errors are derived from 2% error on the efficiency and statistical error from detection. From Lyons et al., 2022

Sample	Activity per g (mBq/g_{H2O})	±	Standard Deviation	Activity per g (TU)	±
SVGS-6	188.20	12.09	6.91	1568.3	100.8
SVGS-7	257.31	15.39	15.01	2144.2	128.3
SVGS-8	205.29	13.25	8.53	1710.8	110.4
SVGS-9	230.01	14.56	15.74	1916.8	121.3
SVGS-10	1450.79	113.71	690.66	12089.9	947.6
SVGS-11	192.31	13.09	9.68	1602.6	109.1
SVGS-12	270.58	17.42	12.58	2254.8	145.2
SVGS-13	258.37	16.13	11.65	2153.1	134.4
SVGS-14	321.17	18.88	13.45	2676.5	157.4
SVGS-15	441.95	31.77	177.62	3682.9	264.7

The first group (SVGS-6 through 10) collected, on average, 0.60 g of water, except for SVGS-10, located near the apron, which averaged an order of magnitude less. The second group (SVGS-11 through 15) collected, on average, 0.58 g of water, except for the SVGS-15, again near the apron, which collected roughly half the average. SVGS-1 through 5 were collected but encountered shipping issues and were not measured at the lab.

The silica gel was directly measured for tritium activity using liquid scintillation counting. Since each site was sampled in triplicate, the results in 5 are an average of the results from the three individual measurements, except for SVGS-6 and -7, which are duplicate averages. One of the triplicate samples from these sites was found to be leaking prior to counting and was discarded. SVGS-10 and -15 demonstrate a very low total activity but high normalized activity due to the low mass collected. The samples at these sites also varied tremendously, as shown by the high standard deviation, making the error bars for this site ~50%. There seems to be good agreement between repeated sites, but further validation may be needed. In contrast to typical atmospheric or rainwater background levels of less than 10 TU, all locations yielded significantly elevated tritium concentrations. Additional details can be found in Lyons et al (2022) [12].

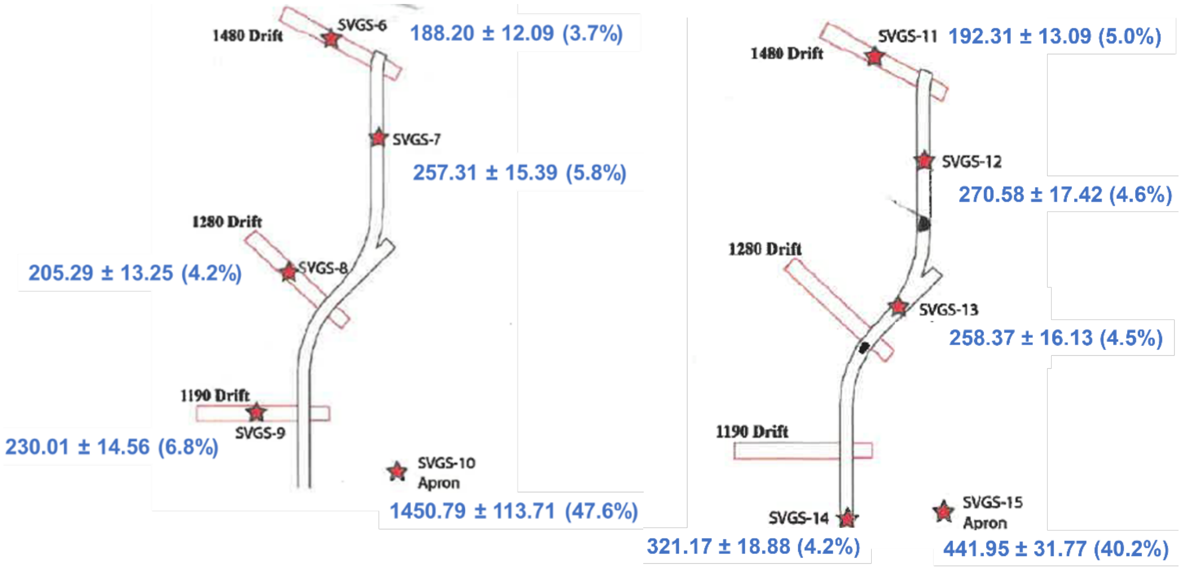

Values at each location:
Avg. Activity [mBq/g_{H2O}] ± Error, (% Std. Dev)

Values at each location:
Avg. Activity [mBq/g_{H2O}] ± Error, (% Std. Dev)

Figure 33. Collection location map and measurement values. The values presented at each location are the average activity in mBq/g of water collected with the associated statistical error and in parenthesis the standard deviation in percent. For additional details see Lyons et al. (2022) [12].

8.3. Confinement Leak Test Sampling

As part of Confinement, a grout plug was poured in the 1490 drift following HE emplacement to confine the explosion and byproducts. An important aspect of the plug is that it should contain no pathways for gas to vent from the chamber when under pressure. To test for potential venting, two leak tests were performed during the grouting process. A tracer (Freon or Sulfur Hexafluoride [SF6]) was pumped into the chamber, building pressure, and real time monitors were used to detect the presence of the tracer in the U12p.06 Bypass drift. Background measurements of the tracers are important to estimate the needed concentrations for a successful test.

We collected ten 2.7-L samples over three campaigns (Figure 34). Samples were collected using the same methodology as the small volume gas samples and using the same bottle types. Samples were collected under both ventilated and non-ventilated conditions and were repeated for several key locations.

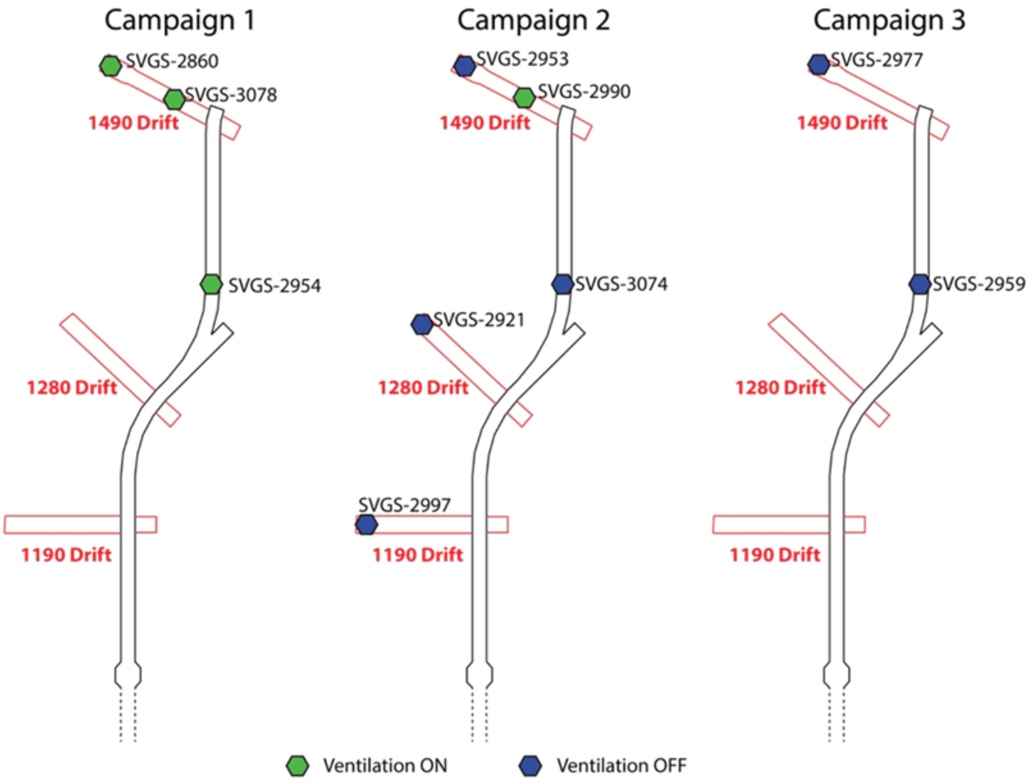

Figure 34. Emplacement locations for the Confinement Leak Test samplers. Colors denote if the sample was done with ventilation on (green) or ventilation off (blue).

The samples were analyzed for SF6 and a suite of Freons (R-132, R-132a, R-132b, R-122, R-122a, and R-124). The two leak tests used SF6 and Freon, respectively, as the detectable tracer. All samples measured SF6 to be below the detectable limit of 50 ppm (Table 18). Additionally, all samples measured R-124, R-122, and R-122a to be below the detectable limits of 2, 0.5, and 0.5 ppm respectively. Measurements of R-132 and R-132a were below the detectable limit of 0.5 ppm for all but SVGS-2297 (<1 ppm), the southernmost sample at the 1190 drift face. Measurements of R-132b were all below the detectable limit of 0.1 ppm except for SVGS-2959, SVGS-2953, and SVGS-2921 (<0.5 ppm). These samples came from various locations, but all were taken with the tunnel ventilation off.

Table 18. Summary table of results from the Freon and SF6 testing done by Intertek on the Confinement Leak Test samples.

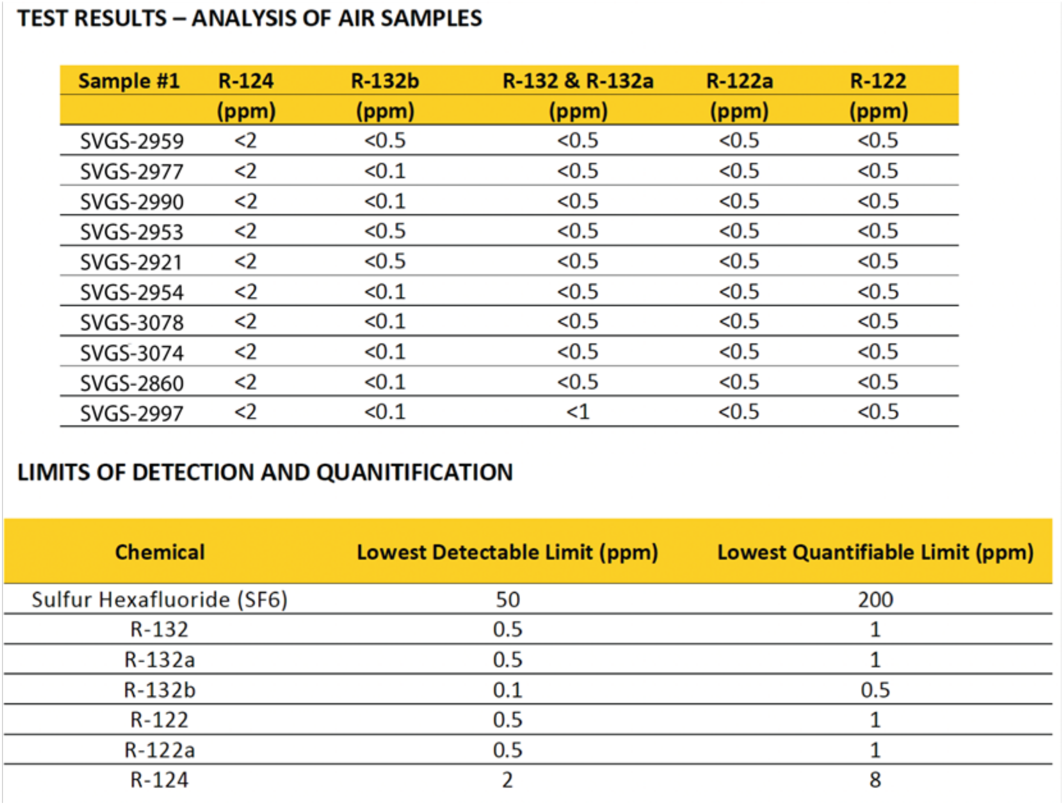

TEST RESULTS – ANALYSIS OF AIR SAMPLES

Sample #1	R-124 (ppm)	R-132b (ppm)	R-132 & R-132a (ppm)	R-122a (ppm)	R-122 (ppm)
SVGS-2959	<2	<0.5	<0.5	<0.5	<0.5
SVGS-2977	<2	<0.1	<0.5	<0.5	<0.5
SVGS-2990	<2	<0.1	<0.5	<0.5	<0.5
SVGS-2953	<2	<0.5	<0.5	<0.5	<0.5
SVGS-2921	<2	<0.5	<0.5	<0.5	<0.5
SVGS-2954	<2	<0.1	<0.5	<0.5	<0.5
SVGS-3078	<2	<0.1	<0.5	<0.5	<0.5
SVGS-3074	<2	<0.1	<0.5	<0.5	<0.5
SVGS-2860	<2	<0.1	<0.5	<0.5	<0.5
SVGS-2997	<2	<0.1	<1	<0.5	<0.5

LIMITS OF DETECTION AND QUANITIFICATION

Chemical	Lowest Detectable Limit (ppm)	Lowest Quantifiable Limit (ppm)
Sulfur Hexafluoride (SF6)	50	200
R-132	0.5	1
R-132a	0.5	1
R-132b	0.1	0.5
R-122	0.5	1
R-122a	0.5	1
R-124	2	8

8.4. Large-Volume Gas Sampling

In order to analyze background concentrations of xenon, a larger sample volume than was collected in the SVGS samples is required. Five large-volume gas samples were collected for analysis of Xe-126 and Xe-127. Four of these samples were collected from the GS boreholes while the remaining sample was collected at the face of the 1490 drift (Figure 35).

Samples were initially collected using a rough pump to fill a 500-gal bladder over the span of several hours. The bladders were then transported out of the tunnel and onto the apron, where they were transferred into SCUBA tanks (rated to hold 80 SCF at 3000 psi) using a dive air compressor.

Analysis of the large-volume gas samples is still underway.

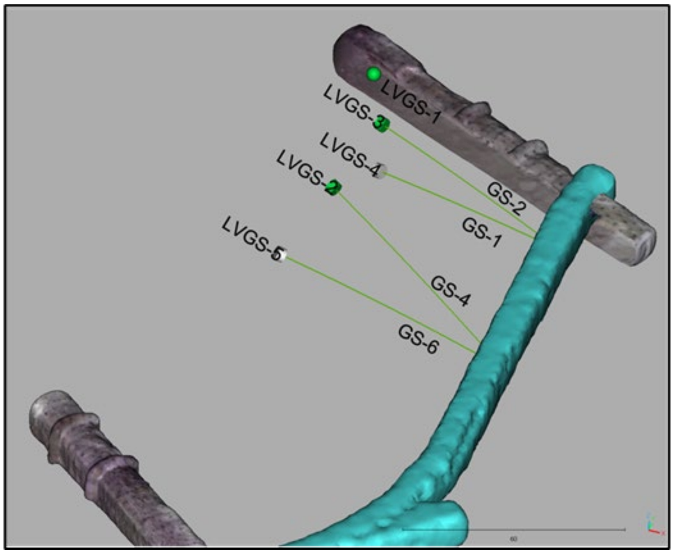

Figure 35. Locations of the five large-volume gas samples. The green sphere is the location in the A chamber. The four cylinders are the collection locations inside the gas boreholes using the Grab Sampling systems infrastructure. Green cylinders are from Campaign 1 and White cylinders are from Campaign 2. Cylinder length represents sampling borehole interval. Diameters were sized for display only and don't reflect radial sampling extent. 1490 drift left rib removed for clarity.

8.5. Pre-Experiment A Gas and Liquid Sample Collection

Prior to execution of PE1 Experiment A, gas and liquid samples were collected from the gas sampling boreholes and the tunnel environment (TE). These were collected to provide background information just before the explosion. The two separate collection events were performed on 9/27/2023 and 10/10/2023.

Gas grab samples were collected in 2.7-L stainless steel bottles connected to an automated manifold system, which allowed for multiple collections from each gas sampling borehole as a function of time. Both sample events collected a representative subset (2-3 per sampling location) of the 2.7-L bottles from the manifold system. Specifically, the bottles collected contained gas from GS-2, GS-3, GS-4, GS-6, TE-1, and TE-2. TE samples are of the ambient air conditions in the tunnel.

Each gas sampling system – GS and TE – has a water trap as part of its gas recirculation system. In addition, the GS boreholes have an additional water trap located at the borehole collar. As part of both sample collection events, each water trap was tapped to remove any collected liquid. For both events, all the borehole collar and TE water traps did not contain any appreciable volume of liquid. All the water traps for the GS borehole recirculation system did contain a sufficient liquid volume to allow for sample collection.

8.6. Radiologic Swipes

Radiologic swipes are routinely taken for material leaving P-Tunnel to ensure that there is no radiological hazard. Results of the swipe analyses were archived starting with core produced by the GI-2, -3, and -4 boreholes. These results are useful to understand the background contamination and to better understand the hazards present in the tunnel prior to Experiment A. After the initial round of core drilling, the NNSS radiological department determined that material leaving P-Tunnel could be released without undergoing testing. However, some radiological swipe analyses were requested to be done for the sake of broadening the archived data set.

The locations and findings from swipes can be found in Table 19. All results coming from the tests found alpha and beta counts to be below the minimum detectable activity (MDA).

Table 19. Radiologic swipe data that has been archived for materials being cleared for release from the tunnel.

Survey	Survey points	Date	Swipes
21-SMS-A12-002	U12 GI-2 core, drilling pipe sections, sample prep area	2/4/21	25
21-SMS-A12-003	Drill bit, U12 GI-2 core, sample prep area	2/9/21	15
21-SMS-A12-005	U12 GI-3 core, sample prep area	2/24/21	33
21-SMS-A12-008	U12 GI-4 core, sample prep area	3/31/21	61
21-SMS-A12-066	U12 PH-1 core, sample prep area	5/17/21	57
21-SMS-A12-073	U12 PH-1 core, sample prep area	6/7/21	19
21-SMS-A12-074	1190 grab samples, sample prep area	6/7/21	19
21-SMS-A12-076	U12 PH-2 core, sample prep area	6/28/21	56
21-SMS-A12-088	Tritium background, drill bits, rubber hose, U12 PH-3 core, sample prep area	8/17/21	17
21-SMS-A12-092	U12 PH-4 core, U12 PH-5 core, misc. core samples, sample prep area	8/31/21	36
21-SMS-A12-093	Mini excavator #3715 & components, Mini excavator #3991 & components, Bobcat #3722 & COMPO Mini excavator #3715 & components, sample prep area	8/31/21	46
22-SMS-A23-477	U12 1490 short cores, sample prep area	10/4/22	14

This page left blank

REFERENCES

[1] Bish, D.L. 1993. Thermal behavior of natural zeolites. LA-UR93-2881, Proceedings of Zeolite '93 Conference, Los Alamos National Laboratory, 24 p.

[2] Chipera, S.J., Goff, F., Goff, C.J., and Fittipaldo, M. 2006. Zeolitization of intracaldera sediments and rhyolitic rocks of Valles caldera, New Mexico, USA. In Zeolite '06—7th International Conference on the Occurrence, Properties, and Utilization of Natural Zeolites, Bowman, R.S. and Delap, S.E. (eds.), Socorro, New Mexico, USA, 16-21 July 2006.

[3] Gaylord, J., 2021, *LYNM PE1 Surface Station List*, LYNM-PE1-1.06-014PLN

[4] Heath, J.E., Dewers, T.A., McPherson, B.J.O.L., Nemer, M.B., Kotula, P.G. 2012. Pore-lining phases and capillary breakthrough pressure of mudstone caprocks: Sealing efficiency of geologic CO_2 storage sites. International Journal of Greenhouse Gas Control 11, 204–220.

[5] Heath, J.E., Kuhlman, K.L., Broome, S.T., Wilson, J.E., and Malama, B. 2021. Heterogeneous multiphase flow properties of volcanic rocks and implications for noble gas transport from underground nuclear explosions. Vadose Zone Journal 20(3), e20123, https://doi.org/10.1002/vzj2.20123.

[6] Jones, F and Associates, Inc. 1985 "Porosimeter Theory" Theory of operation of Coberly-Stevens porosimeter.

[7] Kibikas, W.M., Wilson, J.E., Jaramillo, J.L., Broome, S.T., Bodmer, M.A., Choens, R.C., and Feldman, J. Geomechanical Properties of Vitric and Zeolitic Nonwelded Tuffs, (submitted).

[8] Knowlton, G.D., White, T.R., and McKague, H.L. Thermal Study of Types of Water Associated with Clinoptilolite. Clays Clay Miner. 29, 403–411 (1981). https://doi.org/10.1346/CCMN.1981.0290510.

[9] Kotula, P.G., Keenan, M.R., 2006. Application of multivariate statistical analysis to STEM X-ray spectral images: interfacial analysis in microelectronics. Microscopy and Microanalysis 12, 538–544.

[10] Kuhlman, K.L., F.T. Good, T. LaForce & J.E. Heath, 2022. FY22 Progress on Imbibition Testing in Containment Science, SAND2022-13014, Albuquerque, NM: Sandia National Laboratories.

[11] Lorenz, J.C. and Cooper, S.P., 2017. *Atlas of natural and induced fractures in core*. John Wiley & Sons.

[12] Lyons, Stephanie M., Aalseth, Craig E., Lawler, Bethany M., Seifert, Allen. December 2022 Passive Moisture Collection for Site Characterization.

[13] Marjoribanks, R., 2010. *Geological Methods in Mineral Exploration and Mining*, 2nd ed., 179, doi:10.1007/978-3-540-74375-0, Springer-Verlag Berlin Heidelberg.

[14] Myers, et al., 2024. A Multi-Physics Experiment for Low-Yield Nuclear Explosion Monitoring, LLNL-TR-864107, 17p. DOI:https://doi.org/10.2172/2345984.

[15] Moore, D.M, Reynolds, R.C. Jr. 1997. X-ray Diffraction and the Identification and Analysis of Clay Minerals, Second Edition. Oxford University Press, New York, 400 p.

[16] Prothro, L. B. 2018. Geologic Framework Model for the Underground Nuclear Explosions Signatures Experiment, P-Tunnel Testbed, Aqueduct Mesa, Nevada National Security Site. Mission Support and Test Services, DOE/NV/03624--0312.

[17] Rodriguez, M.A., Kotula, P.G., Griego, J.M., Heath, J.E., Bauer, S.J., and Wesolowski, D.E. 2012. Multivariate statistical analysis of micro-X-ray fluorescence spectral images. Powder Diffraction 27(2), 108–113, doi: 10.1017/S0885715612000243.

[18] Schindelin, J., Arganda-Carreras, I., Frise, E., Kaynig, V., Longair, M., Pietzsch, T., Preibisch, S., Rueden, C., Saalfeld, S., Schmid, B., Tinevez, J., White, D.J., Hartenstein, V., Eliceiri, K., Tomancak, P., and Cardona, A. 2012. Fiji: an open-source platform for biological image analysis. Nature Methods 9(7), 676–682, doi:10.1038/nmeth.2019.

[19] Stauffer, P.H., Otto, S., Boukhalfa, H., and Bodmer, M. 2022. June 2022 Permeability Measurements in P-Tunnel, Nevada National Security Site. United States: LA-UR-22-27846, 18p., doi:10.2172/1883116.

[20] Swanson, B.F. 1981. A simple correlation between permeabilities and mercury capillary pressures. Journal of Petroleum Technology 33, 2498–2504.

[21] Vigil, S.R., 2016. Underground Nuclear Explosion Signatures Experiment. No. SAND2016-8565PE. Sandia National Lab. (SNL-NM), Albuquerque, NM (United States).

[22] Wilson, J.E., Heath, J.E., Kuhlman, K.L., Xu, G., Bodmer, M.A., Broome, S.T., Jaramillo, J., Barrow, P., Rodriguez, M.A., Griego, J.J.M., Valdez, N.R., Reppart, J., Smith, D., Larotonda, J., Townsend, M., 2024. PE1 Site Characterization: Data Documentation on Geologic and Hydrologic Lab Testing, SAND2024-07526.

DISTRIBUTION

Email—Internal

Name	Org.	Sandia Email Address
Technical Library	1911	sanddocs@sandia.gov

This page left blank

Sandia National Laboratories

Sandia National Laboratories is a multimission laboratory managed and operated by National Technology & Engineering Solutions of Sandia LLC, a wholly owned subsidiary of Honeywell International Inc. for the U.S. Department of Energy's National Nuclear Security Administration under contract DE-NA0003525.